Line shape analysis for precision spectroscopy in Ba+ ions

Valappol, Nivedya

DOI:
10.33612/diss.100383960

Line shape analysis for precision spectroscopy in Ba^+ ions

To my parents

Cover: Designed by: Ilse Modder

university of groningen / faculty of science and engineering / van swinderen institute for particle physics and gravity

Nederlandse Organisatie voor Wetenschappelijk Onderzoek

This work is part of a research program 'Broken Mirrors and Drifting Constants' funded in part by the Stichting voor Fundamenteel Onderzoek der Materie (FOM), which is financially supported by the Nederlandse Organisatie voor Wetenschappelijk Onderzoek (NWO).

ISBN: 978-94-034-2112-4 (printed version)
ISBN: 978-94-034-2111-7 (electronic version)

Cover design: Line shape fit to experimental data represented as heartbeat pulses. At the center is a symbol of Sudarshana Chakra, literally meaning "disk of auspicious vision" placed as a tribute to theoretical physicist E. C. George Sudarshan.
Printed by: Gildeprint

university of groningen

Line shape analysis for precision spectroscopy in Ba^+ ions

PhD thesis

to obtain the degree of PhD at the
University of Groningen
on the authority of the
Rector Magnificus Prof. C. Wijmenga
and in accordance with
the decision by the College of Deans.

This thesis will be defended in public on

12 November 2019 at 11:00 hours

by

Nivedya Valappol

born on 18 February 1990
in Kerala, India

Supervisor
Prof. K. H. K. J. Jungmann

Co-supervisor
Dr. L. Willmann

Assessment committee
Prof. R. A. Hoekstra
Prof. P. van der Straten
Prof. K. Wendt

Abstract

Most precise tests of the Standard Model (SM) in particle physics set stringent bounds on New Physics models and enable searches for new Physics beyond the SM. Conducting precision experiments on Atomic Parity Violation (APV) paves a way to determine the SM parameter Weinberg angle ($\sin^2\theta_W$) at low energies. Knowledge of atomic wave functions arbitrates the precision to which $\sin^2\theta_W$ can be determined. Calculations on atomic systems with a single valence electron such as Ba^+ and Ra^+ are possible with sufficient accuracy for this purpose. Such an experiment becomes feasible, if a single ion is localized to better than one optical wavelength in order to have the ion in the maximum of the electric and the magnetic fields of two standing waves which drive the two relevant transitions.

Measurements on a single trapped $^{138}Ba^+$ ion for the detailed understanding of atomic structure at percent level precision have been performed with laser spectroscopy referenced to an optical frequency comb. The one-photon and two-photon components of the line shape are extracted using an eight-level optical Bloch model. Measurement of transition frequencies in different Ba^+ isotopes, $^{136}Ba^+$ and $^{134}Ba^+$ enable the determination of isotope shifts. An analysis employing Fano line profiles provides for extracting the transition frequencies between the lowest lying S, P and D states in Ba^+ isotopes within 200 kHz. Furthermore, systematic effects are investigated by comparing multiple measurement schemes on trapped Ba^+ ions in a radio frequency Paul-trap setup.

Transitions in molecular $^{127}I_2$ serve as reliable secondary frequency standards. The line shape of signals from frequency modulated saturated absorption spectroscopy of hyperfine transitions in $^{127}I_2$ is analyzed. The derived line shape includes effects arising from experimental parameters. Consistent results for line center, density broadening and density shift of spectral lines to 10^{-11} relative accuracy have been obtained.

Precise spectroscopy is a major prerequisite for an experiment to determine atomic parity violation. This work is an important step towards a precise determination of $\sin^2\theta_W$ with some 5 fold improvement over the previous best measurement in one week of actual measurement time.

Contents

‡We summarize here the main contents of the paper where it distinguishes itself from the treatment in Chapter 5 of this thesis. The main contents of this chapter is also published under E. A. Dijck et al. [81], where also additional material is provided.

1. Introduction

1.1. Standard Model and Electroweak interaction

The Standard Model (SM) of particle physics [1, 2] provides a unique and elegant description of fundamental interactions between elementary particles. The SM has been enormously successful in describing and predicting a wide range of phenomena in physics and in particular in particle physics. Its remarkable success strongly suggests that the SM will remain an excellent approximation to nature from cosmic scales to distance scales as small as 10^{-18}m [3]. The discovery of the Higgs boson in 2012 [4, 5] represents an impressive confirmation of the concepts in the SM. The production rate as well as the decay pattern follow the predictions of the theory. The Higgs boson discovery completes the search for all particles foreseen in the SM (see Fig 1.1).

A number of experimental and theoretical reasons are known which strongly point to the fact that the SM is an incomplete description of the full set of observations in physics. Theoretically, the SM presents a number of unsatisfying features such as the hierarchy problem (instability of the electroweak scale), the unexplained origins of elementary particle mass and the violation of discrete symmetries (e.g parity), and it lacks a path to unification with gravity. Similarly, experimental observations of neutrino oscillations, along with cosmological phenomena of dark matter and energy and the matter-antimatter asymmetry, have posed puzzles for particle physics that cannot be solved within the SM. The search for physics beyond the SM that addresses these experimental and theoretical questions entails effort at three frontiers: the high energy frontier, for example, at the CERN Large Hadron Collider; the Cosmological frontier, including probes of the cosmic microwave background and large scale structure, as well as indirect astrophysical detection of

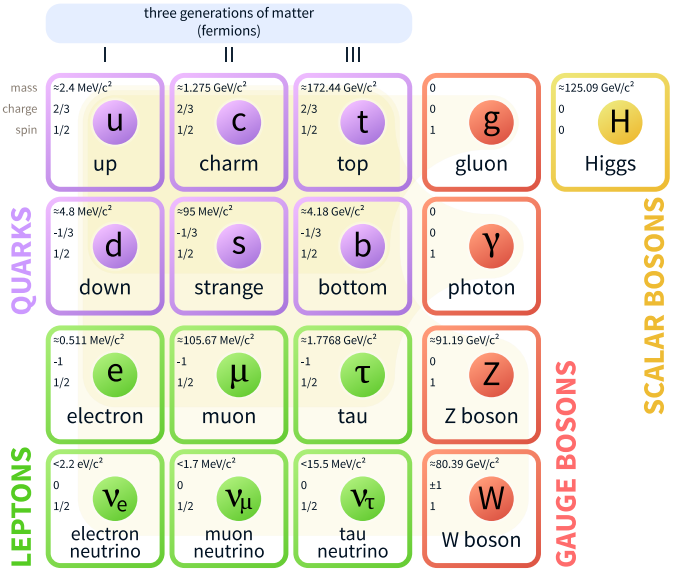

Figure 1.1.: Standard Model of elementary particle physics with the three generations of matter, gauge bosons in the fourth column, and the Higgs boson in the fifth. The values currently reflected in this graphic are as of 2017. (Adapted from [6]).

dark matter; and the Precision frontier, for example, Atomic Parity Violation measurements (APV) and searches for permanent Electric Dipole Moments (EDMs).

The SM combines the weak and electromagnetic forces in a single electroweak gauge theory [1, 2], in a similar way to Maxwell's unification of the seemingly distinct forces of electricity and magnetism. The theory suggests that all electromagnetic and weak phenomena are manifestations of one universal electroweak interaction mediated by four massless spin-1 bosons, two charged ($W^{\pm}$) and two neutral ones (Z^0 and the photon γ). After the spontaneous breaking of the electroweak symmetry by the vacuum, three of the four bosons acquire mass. The weak interactions are mediated by the three massive gauge bosons, $W^{\pm}$ and Z^0. Due

to these large masses, the range of the weak interactions with 10^{-17}m is rather short. Direct measurement of weak interactions is not possible since it is about 18 orders of magnitude weaker than the electromagnetic force, which to the contrary is rather strong and can be experimentally measured very accurately. However, it is possible to measure the effect of Z^0 boson exchange between an electron and a nucleus by looking at the quantum mechanical interference between these processes which is only about 6 orders of magnitude weaker than the electro magnetic interaction (Fig 1.2). Unlike the electromagnetic force, the weak force does not respect certain discrete symmetries such as parity (P), which describes the symmetry between right- and left-handed particles; charge conjugation (C), which is the exchange of particles by antiparticles, i.e., particles with the same mass but opposite charge; and the combination of these two symmetries (CP).

Electroweak theory permits the extraction of the SM parameter called the weak mixing angle or the Weinberg angle ($\sin^2\theta_W$) [7] which describes the mixing of the photon (γ) and the Z^0 boson. It connects the two independent coupling constants of the electroweak theory: the electric charge, e, and the weak coupling constant, g_W, through the relationship [8]

$$sin^2\theta_W = \frac{e^2}{g_W^2}. \tag{1.1}$$

It can be defined as [7, 9]

$$sin^2\theta_W = 1 - (m_W/m_Z)^2, \tag{1.2}$$

where m_W and m_Z represent the masses of the W and Z bosons receptively. A quantitative determination of the electroweak interaction in atoms is possible by the electric charge and the weak nuclear charge Q_{weak}. The magnitude of Q_{weak} is given by [10]

$$Q_{weak}(Z,N) = -N + (1 - 4sin^2\theta_W)Z, \tag{1.3}$$

where N and Z are the number of neutrons and protons in the nucleus. The finite nuclear size corrections are dominated by the spatial dependence of the neutron density. The uncertainties for the measurement

of the Weinberg angle associated with this correction have been estimated [11] to be about $\pm 0.15\%$ for cesium. The uncertainties associated with nucleon structure are comparably small [12, 13].

Fig 1.3 shows the Weinberg angle ($\sin^2\theta_W$) as a function of the momentum transfer in experiments. It is predicted by electroweak theory (black solid line). When propagating from low energies to about the $W^{\pm}$ boson mass scale the mixing angle slowly decreases by about 3% [14] due to vacuum polarization by the formation of quark-antiquark pairs. A screening effect is caused due to this which effectively reduces the weak charge of the interacting particles. At higher energies, an anti-screening of the interacting particles is caused if $W^{\pm}$ pairs start to dominate the vacuum polarization. This results in an increase of the weak charge and hence results in an increase of the mixing angle. At high Q as indicated in Fig 1.3 the weak mixing angle has been measured accurately by SLAC's SLD experiment and the LEP experiments at CERN [15] at the Z-pole. The SLAC E158 collaboration [16] measured the parity-violating asymmetry with a fixed target electron-electron (Møller) scattering, and the NuTeV [17] collaboration extracted the $\sin^2\theta_W$ by measuring the ratios of neutral current to charged current cross sections in neutrino-nucleon deep inelastic scattering experiments. In addition, such an experiment has sensitivity to new physics such as dark Z bosons and leptoquarks [18, 19] (see Fig 1.3).

Unlike the gauge couplings of QED and QCD, whose running below the weak scale has been stringently tested in a variety of ways, the low scale running of ($\sin^2\theta_W$) has been tested precisely in only a handful of experiments. A well known precise experiment that probes $\sin^2\theta_W$ is the APV experiment on Cs with an accuracy of 0.35% by the Boulder group [20, 21, 22, 23, 24, 25, 26]. The experiment was conducted by exploiting the Stark interference method, a method involving applying an external electric field to a vapor, thereby inducing Stark-mixing of the atomic levels and leading to parity forbidden atomic transitions and a beam of cesium atoms. Higher precision (0.1%) is required to search for new Physics (NP) beyond SM [27]. An independent measurement by measuring atomic parity violation in a single trapped barium or radium ion together with the experiments at higher momentum transfer

has potential to confirm the running of the mixing angle over more than 4 orders of magnitude in momentum transfer.

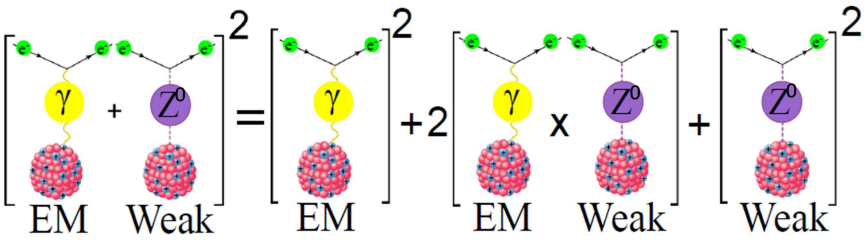

Figure 1.2.: Quantum mechanical interference between weak and electromagnetic interactions in atomic systems. The amplitudes of both these processes are coherently added to arrive at the probability of the combined process. Modified from [28].

Various nuclear and atomic parameters are relevant for the interpretation of measurements on atoms in terms of weak interaction effects. Understanding atomic structure and atomic behavior to percent accuracy needs the determination of parameters such as lifetime, transition frequencies, light shifts, hyperfine structure and isotope shifts (IS) to be determined experimentally. In this work we are devoted to this task.

1.2. Atomic Parity Violation in atomic systems

Scientists first observed parity violation in 1957 with a crucial pioneering experiment on the β-decay of polarized ^{60}Co nuclei [31]. There it was found that electrons are emitted preferentially opposite to the direction of the nuclear spin. Parity violation in atomic systems is caused by the interaction of electrons with the quarks in the nucleus through the exchange of Z^0 bosons. The APV measurements are interpreted in terms of the weak nuclear charge Q_{weak} , which quantifies the strength of the electroweak coupling between atomic electrons and quarks in the nucleus. The relation between Q_{weak} and the APV amplitude, $E1_{APV}$, can be represented as

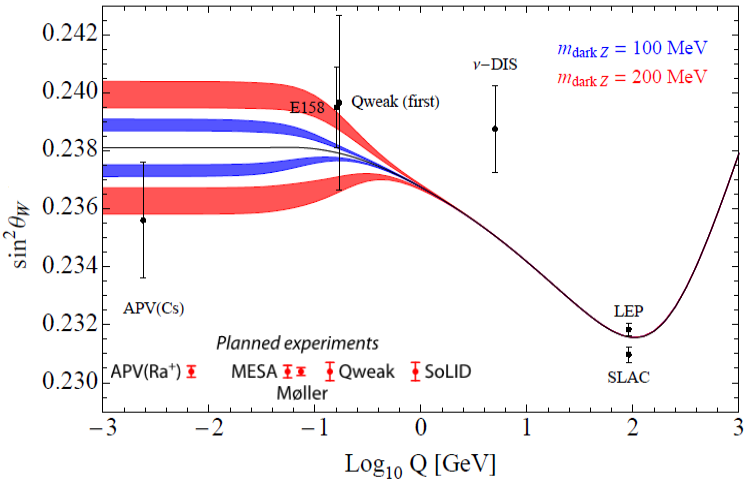

Figure 1.3.: Running of the Standard Model parameter Weinberg angle ($\sin^2\theta_W$) as a function of momentum transfer Q. The solid line represents the behavior of $\sin^2\theta_W$ as predicted by the SM where the curve has been fixed at the z-pole. The results from the SLAC, LEP, deep inelastic ν scattering, PV Møller scattering, and APV(Cs) are shown. The red and blue bands represents the sensitivity to a possible dark Z-boson of mass 200 MeV/c^2 and 100 MeV/c^2 respectively. APV is particularly sensitive to dark Z bosons [19, 29, 30] with masses below 100 MeV. This may be of significance in the determination of dark matter in the universe (adapted from [30]).

$$E1_{APV} = kQ_{weak}, \tag{1.4}$$

where k is an atomic-structure dependent factor. The interpretation requires atomic-structure calculations of k with an accuracy that matches the experimental uncertainty in APV. Atomic systems with one valence electron enable to reduce the complexity in atomic wavefunction calculations. In such ions and atoms the APV calculations can be carried

out to highest possible accuracy. Also the parity-violating weak effects in atoms increases faster than Z^3 [32](see Fig 1.4) which makes heavy alkaline earth metal ions like Ra^+ and Ba^+ much preferred systems for experimental studies. The atomic structure of these two atoms is simpler to calculate and the theoretically predicted enhancement factors of weak effects in atomic systems like Fr [33, 34] , Ba [35] and Ra [36, 37, 38] compared to Cs are 2.3, 16, and 52, respectively.

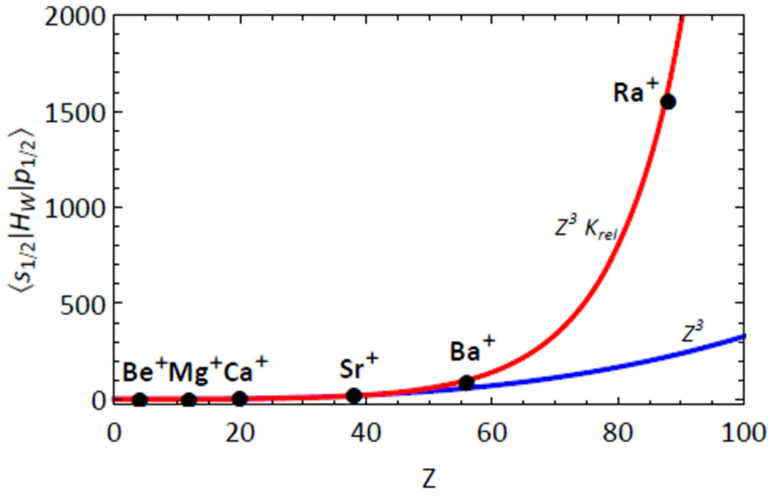

Figure 1.4.: The scaling of the weak interaction matrix element for transition between $n|S_{1/2}\rangle$ - $m|P_{1/2}\rangle$ states atoms with atomic number Z. The blue line corresponds to the scaling with Z^3 [32] and red line shows the scaling stronger than Z^3 due to the relativistic factor K_{rel} [39].

There are principally different techniques that can be used to measure APV such as optical rotation in atomic vapor [40, 41, 42], Stark interference in atomic vapor [43], in atomic beams [44, 21, 45], with small number of atoms and light-shift in a single trapped and laser cooled ion [46, 47]. We use the light-shift in single trapped and laser cooled ion technique since single trapped and laser cooled ion is free from unknown perturbations (e.g.: absence of Doppler broadening) and it has long co-

herence time. Systematic uncertainties are easily tractable and therefore, the system is more favored for such experiment.

Atomic parity violation leads to mixing of different parity states with the ground state $7|S_{1/2}\rangle$. Thus this ground state has also in particular a small contribution from $7|P_{1/2}\rangle$ state resulting in a non-zero probability of electric dipole-dipole transition between $7|S_{1/2}\rangle$ and $6|D_{3/2}\rangle$ states which is in an atomic system strictly following the lambda system coupling scheme a forbidden electric dipole transition. A transitional dipole interacts with the electric field while a quadrupole interacts with the field gradient. It is possible in the experiment to induce both a dipole transition($E1_{APV}$) as well as a quadrupole transition (E2) between $7|S_{1/2}\rangle$ and $6|D_{3/2}\rangle$ states. The interference term of these two leads to a measurable frequency change of the Larmor frequency between the ground state Zeeman sublevels while the laser fields are present and absent. Fig 1.5 shows the light shifts of the Zeeman magnetic sublevels of ground state of Ra^+ if light fields are applied which drives the $E1_{APV}$ and E2 transitions. For a single Ra^+ ion with zero nuclear spin, the splitting between the Zeeman sublevels m= +1/2 and m= -1/2 of the $7S_{1/2}$ ground state in a magnetic field is about $\Delta\omega_{zeeman} = 23\,\frac{MHz}{mT}$ [48].

A possible configuration of the laser light fields to obtain the required APV frequency shift is

$$E1_{APV} = \hat{x}E_0' cos kz \tag{1.5}$$

and

$$E2 = i\hat{z}E_0'' sin kz \tag{1.6}$$

where $E_0'$and E_0'' are the electric field amplitudes of the two lasers [46]. The coupling strength of $E1_{APV}$ and E2 transitions with the electric fields E_0' and E_0'' is given by the Rabi frequencies

$$\Omega_{APV}^{m,m'} = -\frac{1}{2\hbar}\sum\langle E1_{APV}^{m,m'}\rangle_i E_0'(0), \tag{1.7}$$

$$\Omega_{E2}^{m,m'} = -\frac{1}{2\hbar}\sum\langle E2^{m,m'}\rangle_{ij}\left[\frac{\partial E_0''(r)}{\partial x_j}\right], \tag{1.8}$$

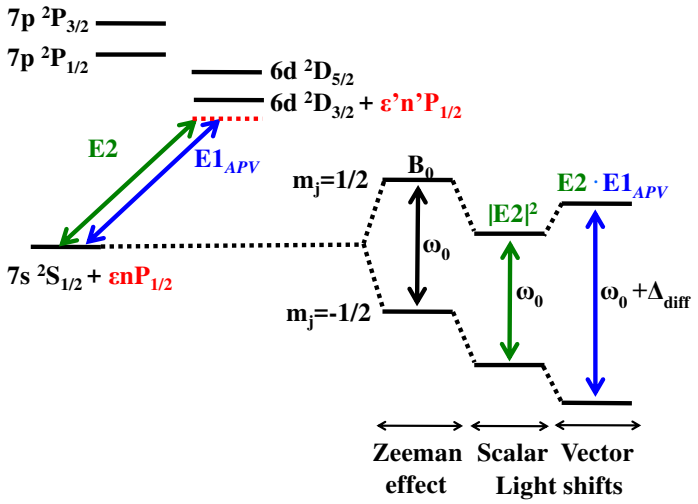

Figure 1.5.: Scalar and vector light shifts on the ground state magnetic sub-levels in the Ra^+ ion with n=7 ground state in the presence of light field driving the E2 and $E1_{APV}$ transitions. The configuration is similar for Ba^+ with n=6 ground state.

where m and m' represent the magnetic quantum numbers of the two states and $\langle E1^{m,m'}_{APV}\rangle$ and $\langle E2^{m,m'}\rangle$ are the matrix elements for the dipole and quadrupole transitions, respectively. An ion placed at the antinode of an electromagnetic wave field with electric field strength $E1_{APV}$ will have an APV induced electric dipole light-shift while the ion placed at the node of an electromagnetic wave of electric field strength E2 will show an electric quadrupole light-shift(see Fig 1.5). The quadrupole light-shifts of the Zeeman sublevels in the ground state due to the E2 field are of the same magnitude and direction and hence will not lead to any change of the ground state Larmor frequency defined by the energy difference between the Zeeman sublevels of the ground state. On the contrary, the shifts due to $E1_{APV}$ field will increase the Larmor frequency and produces

a differential light shift between the two sublevels (Δ_{diff} in Fig.1.5). This change in Larmor frequency is proportional to the magnitude of the $E1_{APV}$ field [46].

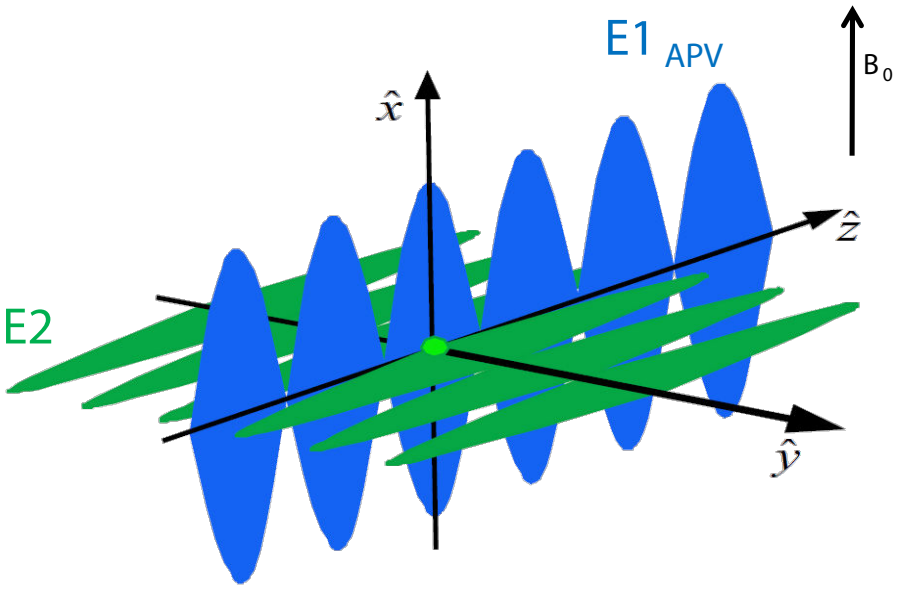

Figure 1.6.: The ion is localized in two standing wave light fields which are perpendicular in polarization to each other for an APV measurement. E2 represents the laser light wave driving the quadrapole transition and $E1_{APV}$ is the dipole transition [45].

The possible accuracy of an APV effect in a single Ra^+ ion is given by,

$$\frac{S}{N} = \frac{E1_{APV}}{\partial E1_{APV}} \cong \Delta_{diff} f \sqrt{Nt\tau}, \tag{1.9}$$

where N is the number of particles and $N = 1$, f is an efficiency factor determined by the experimental conditions, τ is the lifetime of the metastable $D_{3/2}$ state and t is the total measurement time. Table 1.1

gives the expected APV effects [46] for a single trapped Ba^+ and Ra^+ ions.

Table 1.1.: Expected light shifts in single trapped Ba^+ and Ra^+ ion on resonance for 100 mW beam focussed to a 10μm diameter spot size at the ion at wavelength 2050 nm for Ba^+ and 828 nm for Ra^+.

Expected APV light shifts	Ba^+	Ra^+[47]
Differential light shifts	0.4 Hz	4 Hz
Signal to Noise	200	180
Statistical accuracy	1.2 %	0.4 %

A single Ra^+ has the potential for a more than 5-fold improvement in the measurement of the Weinberg angle within one day of measuring time.

1.3. Sensitivity to atomic structure and wavefunctions calculations

Important atomic properties for measuring atomic parity violation are the line shapes of atomic transitions, isotope shifts, light shifts and transition matrix elements. The determination of such is in the center of this thesis.

1.3.1. Line shapes and absolute transition frequencies

In order to investigate the interaction between light and matter and for applications based on high precision spectroscopy such as to construct optical clocks, good understanding of the optical line shapes involved is indispensable. Line shape modeling and extracting the transition frequencies provides crucial input for high precision cross checks with atomic structure calculations and can also improve the understanding of data collected experimentally.

The line shape analysis and extraction of absolute frequencies of $^{127}I_2$ lines used as a secondary frequency standard in our experiment is explained in Chapter 3. The fitting of the resonant fluorescence with a calculation on the basis of Optical Bloch Equations(OBE) and the determination of all relevant transition frequencies is explained in Chapter 4.

1.3.2. Isotope shift

Isotope shift in APV measurement

Atomic structure computations for Ba^+ isotopes are expected to achieve the same level of precision as for cesium (see Ref [49]). A comparison of APV effects in different isotopes eliminates the large atomic structure theory uncertainties. In particular, if a ratio is formulated as [7]

$$\mathcal{R}1 = \frac{A_{APV}^{NSID}(N') - A_{APV}^{NSID}(N)}{A_{APV}^{NSID}(N') + A_{APV}^{NSID}(N)}, \tag{1.10}$$

where $A_{APV}^{NSID}(N)$ is a nuclear spin independent APV observable. If the atomic structure effects which are governed largely by the nuclear Coulomb field, do not vary appreciably along the isotope chain, then we have

$$\mathcal{R}1 = \frac{Q_W(N') - Q_W(N)}{Q_W(N') + Q_W(N)} \approx \frac{N' - N}{N' + N}, \tag{1.11}$$

where the dependence on atomic structure has largely canceled from the ratio. An analogous result occurs for the ratio $\mathcal{R}2 = A_{APV}^{NSID}(N')/A_{APV}^{NSID}(N)$. At present, in order to provide meaningful probes of NP, the theoretical uncertainties associated with this effect appear to be larger than needed for precise isotope measurements [11].

Isotope shift in transition frequency measurement

The difference in neutrons in different isotopes of Ba^+ has two small effects of comparable size on atomic wavefunctions and therefore on transition frequencies. The first is called the mass shift and the second is called the volume (field) shift. For heavy elements the optical isotope

shift $\delta\nu_i^{A,A'}$ between isotopes with mass number A and A', can be written as [50, 51]

$$\delta\nu_i^{A,A'} = F_i\delta\left\langle r^2\right\rangle^{A,A'} + M_i\frac{A'-A}{AA'}, \tag{1.12}$$

where F and M are the field- and mass-shift factors, respectively. $\delta\left\langle r^2\right\rangle^{A,A'}$ is the change in mean-square charge radii between isotopes. Here $\mathrm{M} = \mathrm{K}_{NMS} + \mathrm{K}_{SMS}$, the sum of the normal (K_{NMS}) and specific (K_{SMS}) mass shifts. The normal mass shift can be calculated as [52]

$$K_{NMS} = \nu_0 m_e, \tag{1.13}$$

where ν_0 is the transition frequency and m_e the mass of the electron. The K_{SMS} is due to the modifications to all other non-valence electrons which is hard to calculate accurately due to poor convergence of the perturbation theory for this quantity [53]. However, the contribution of the mass shift (both K_{NMS} and K_{SMS}) is small for heavy atoms and simplified estimations are sufficient.

For two transitions, 1 and 2, in a certain element, Eq. 1.12 gives

$$\mu^{A,A'}\delta\nu_1^{A,A'} = \frac{F_1}{F_2}\mu^{A,A'}\delta\nu_2^{A,A'} + M_1 - \frac{F_1}{F_2}M_2, \tag{1.14}$$

where $\mu^{A,A'} = AA'/(A'-A)$ is the mass-modification factor.

The King plot of $\mu^{A,A'}\delta\nu_2^{A,A'}$ against $\mu^{A,A'}\delta\nu_1^{A,A'}$ is used for experiment at the ISOLDE facility of CERN [52] for analysis such that from the gradient and intercept of the linear fit, F and M are calculated (see Fig 1.7). Using rather low-resolution laser spectroscopy of the very neutron-rich ^{233}Ra atom the isotope shift and relative charge radius was determined for the first time at ISOLDE.

Ref. [54] provides a formalism to interpret linear King plots as bounds on new physics with minimal theory input, a method which resembles the data-driven background estimation in collider searches for NP. As King linearity is equivalent to the coplanarity of the vectors the formulas are simplified by introducing a geometrical description of the leading order (LO) factorization of Eqn. 1.14. For each transition, a vector is

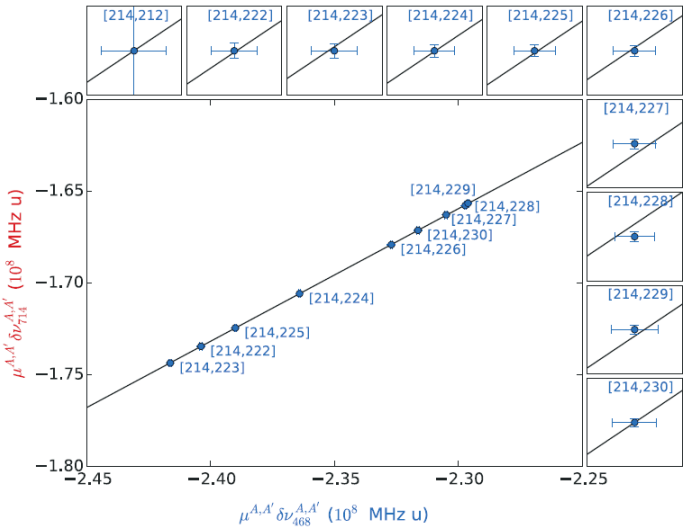

Figure 1.7.: King-plot analysis for the extraction of the atomic factors F and M. Insets are ×100 magnification to show the uncertainties on the data values. (Adapted from [52]).

formed. Also the nuclear parameters of the field and mass shifts $\mu^{A,A'}$ and $\delta\langle r^2\rangle^{A,A'}$ are written as vectors.

Experimental IS data can thus be used to test the precise theoretical predictions. Chapter 5 explains the experimental determination of isotope shifts in different isotopes of Ba^+.

1.3.3. Light shifts

The light shift or ac-Stark shift is a fundamental aspect of field-matter interaction. In the presence of on-resonant laser light the strong coupling of laser light with a single ion results in exchange of population between the ground state and the excited states. This is known as Rabi oscillations. The energy level shift in a two-level system for large detunings

compared to the power broadened linewidth is

$$\Delta E_{g,e} = \pm\hbar\frac{\Omega_{ge}^2}{4\delta}, \tag{1.15}$$

where Ω_{ge} is the Rabi frequency which is determined by the strength of the coupling between the ion and the light field. δ is the detuning of the laser frequency with respect to the resonance of the transition and is given by,

$$\delta = \omega_0 - \omega_L, \tag{1.16}$$

where ω_0 is the frequency of the atomic transition and ω_L is the frequency of the laser light.

For particular ground and excited states $|g\rangle$ and $|e\rangle$, the AC stark shift is

$$\Delta E_{g,e} = \hbar\frac{\Omega_{ge}^2}{4\delta} = \frac{e^2}{4\hbar}\frac{|\langle g|\vec{E}.\vec{r}|e\rangle|^2}{\omega_0 - \omega_L}. \tag{1.17}$$

If the light is far off-resonant red-detuned light, the ground state energy is reduced due to an oscillating polarization that is in phase with the light electric field. Likewise, laser fields tuned far above the resonance will induce a polarization out of phase with the electric field and the ground state energy will be increased (see Fig 1.8). In general, these light shifts are different for any two internal states of an atom and depend on the local intensity of the laser light beams and also on the polarization of the field [55, 56]. Hence changing the detuning and Rabi frequency will affect the fidelity of the experiment.

Additional splitting of the atomic levels into Zeeman components takes place when an external magnetic field is applied to the atomic system. For an isotope with zero nuclear spin there are three Zeeman-split components of the transition. A Stark induced transition amplitude is generally expressed in terms of real scalar, vector, and tensor transition polarizabilities [58, 59, 60]. Fig 1.9 shows a representation of the structure of the scalar, vector and tensor light shifts in Ba^+ and Ra^+. A detailed explanation of this is given in [61, 57]. The measurement of several different experimental parameters of the light shift contribution permits the determination of atomic matrix elements for the Ba^+ system [61, 47, 57, 35, 62].

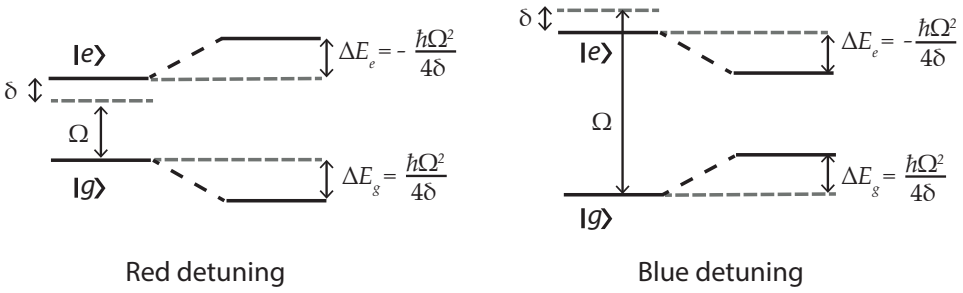

Figure 1.8.: Illustration of the ac-Stark shift or light shift on a two-level system due to far detuned laser light. When the laser frequency is far below the two state resonance, the ground state energy is decreased. Likewise, when laser fields are tuned far above the two state resonance the ground state energy will be increased. Adapted from [57].

1.3.4. Lifetime of the long-lived $D_{5/2}$ state

Lifetime measurements provide transition matrix elements of the quadrupole transition (E2) and therefore test the long-range parts of the nucleus [36, 63, 64]. In atoms or ions the lifetime of an excited state is related to the absolute transition probability

$$\tau = \frac{1}{\sum_i A_{ik}} = \frac{\lambda^3}{\langle i|r|k\rangle^2}, \tag{1.18}$$

where i is the lower state and k is the higher state, A_{ik} is the spontaneous transition probability for electric quadrupole transitions which is given by

$$A_{ik} = \sum_i \frac{8\pi\omega^5}{3c^5h} |\langle\phi_i|Q|\phi_k\rangle|^2, \tag{1.19}$$

where Q is the electric quadrupole operator.

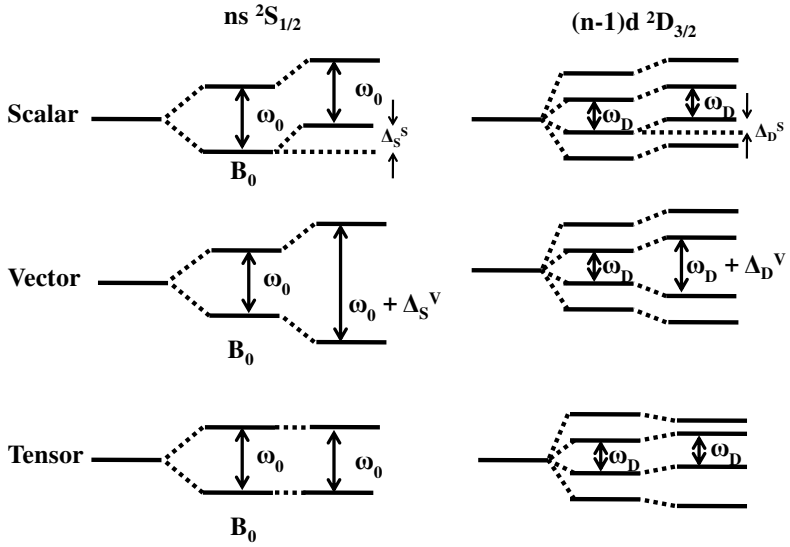

Figure 1.9.: The structure of the scalar, vector and tensor light shifts in the ns $^2S_{1/2}$ and (n-1)d $^2D_{3/2}$ levels where n = 6 for Ba^+ and n = 7 for Ra^+. Here ω_0 and ω_D represents the splitting in the Zeeman sublevels of the ns $^2S_{1/2}$ and (n-1)d $^2D_{3/2}$ levels respectively. Δ_S^S and Δ_D^S are the scalar shift in the S and D states and Δ_S^V and Δ_D^V are the vector shifts in the S and D states. Modified from [57].

1.4. Ra^+ Ion Spectroscopy

Spectroscopy on short-lived isotopes of Ra^+ ($^{209-214}Ra^+$) has been performed and calculated atomic wavefunctions of Ra^+ were tested [28, 65]. The lifetime of the $6d^2D_{5/2}$ state in $^{212}Ra^+$ ions [66, 47] (see Fig 1.10) has been determined. The hyperfine structure of the 6d $^2D_{3/2}$ state [65] and the isotope shift in the 6d $^2D_{3/2}$–7p $^2P_{1/2}$ transition in $^{209-214}Ra^+$ ions [65] (see Fig 1.11) could be measured at the TRiμP facility at the AGOR cyclotron. These are crucial for the evaluation of the uncertainties of atomic structure calculations. It appears that experiment and theory agree at typically to % level. Improved calculations are possible at sub-%

level when the experimental work will have reached the precision needed.

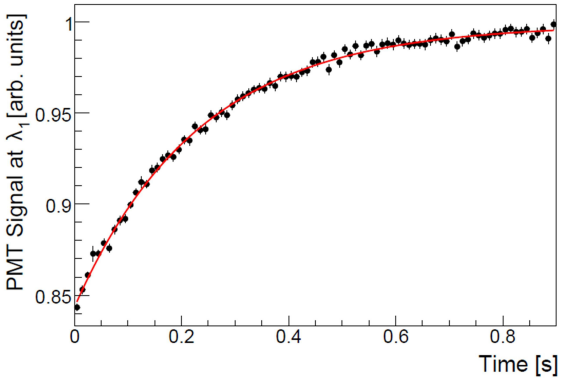

Figure 1.10.: Lifetime measurements of the $6d\,^2D_{5/2}$ state in $^{212}Ra^+$ ions in neon buffer gas at pressure $4{\times}10^{-5}$mbar. The solid line represents the recovery time needed for ions to re-enter the fluorescence cycle and an exponential function is fitted to the data. The measurements were performed with ions trapped in a Paul trap (from [28, 65]).

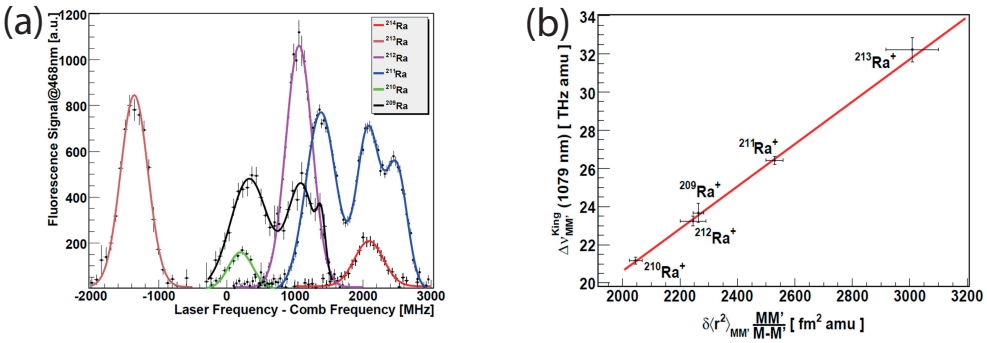

Figure 1.11.: (a) Fluorescence spectrum for the $6d\,^2D_{3/2}$ state of different isotopes of $^{209-214}Ra^+$ ions. The odd isotopes have hyperfine structures on it while there are no hyperfine structures for the even isotopes of Ra^+ ions. (b) Isotopic shifts on the $6d\,^2D_{3/2}$–$7p\,^2P_{1/2}$ transition for different isotopes of $^{209-214}Ra^+$ ions. The measurements were performed with ions trapped in a Paul trap.(From [28, 65]).

1.5. Experimental Realization

The scheme of measuring APV in a single trapped ion or atom was proposed by Fortson in 1993 [46]. Since Ra^+ and Ba^+ are isoelectronic, and due to the lack of stable isotopes for Ra^+ measurements towards APV are conducted using a Ba^+ ion confined in a radio frequency hyperbolic Paul trap. The energy level scheme for Ra^+ and Ba^+ for the relevant transitions are given in Fig 1.12.

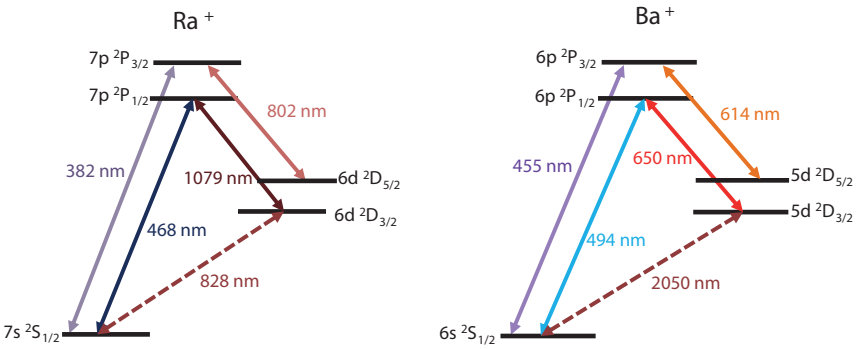

Figure 1.12.: Energy level scheme for Ra^+ and Ba^+ for the lowest lying S, P and D states. Ra^+ and Ba^+ have a Λ-level configuration.

In an ideal hyperbolic Paul trap [67, 68, 69], which is comprised of a center hyperbolic ring electrode and two hyperbolic end-caps, the electric potential is given by [70]

$$\Phi = \frac{2z^2 - x^2 - y^2}{2d^2}(U_0 + V_0 cos\Omega_{RF} t), \tag{1.20}$$

where

$$d = \sqrt{\frac{1}{2}r_0^2 + z_0^2}. \tag{1.21}$$

Here U_0 is an applied DC potential between the ring and both endcaps, V_0 is the amplitude of the AC potential difference between the electrodes,

Ω_{RF} is the rf frequency of the applied AC voltage, r_0 is the inner radius of the center hyperbolic ring and $2z_0$ is the minimum distance between the two endcaps (see Fig 1.13).

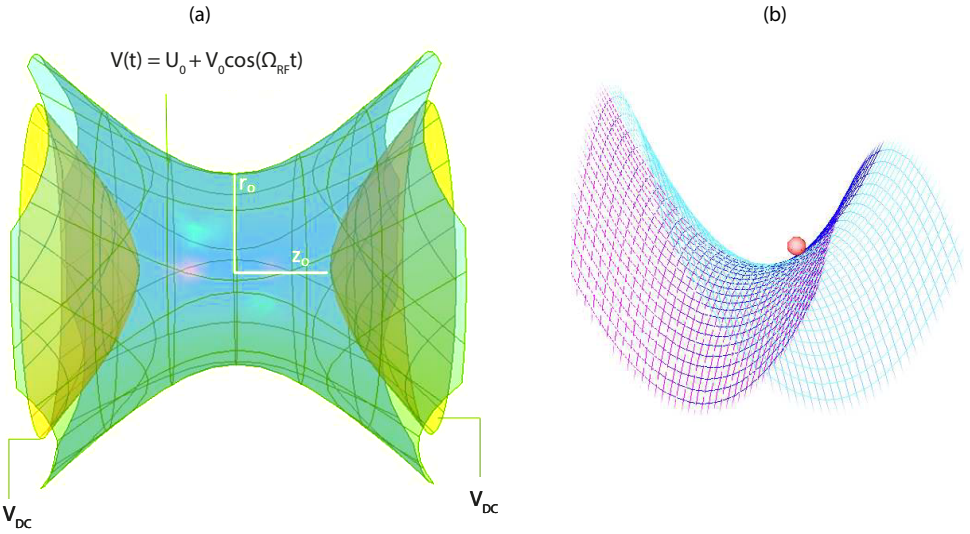

Figure 1.13.: (a). Representation of hyperbolic Paul trap. A time varying AC potential V(t) is applied to the ring electrode. U_0 is the DC offset, V_0 is the amplitude of the potential difference between the electrodes. A biased DC voltage V_{DC} is applied to the endcaps. r_0 is the inner radius of the center hyperbolic ring and $2z_0$ is the minimum distance between the two endcaps. Adapted from [71]. (b). The mechanical analog to the rf Paul trap. Rotating the hyperbolic saddle shaped potential at a proper rate, makes the ion stay on the surface [67, 72].

The equation of motion for a charged particle is described by the Mathieu equation as

$$\frac{d^2u_j}{dt^2} + (a_j - q_j cos2T)u_j = 0. \tag{1.22}$$

Here $u_1 = x, u_2 = y, u_3 = z$, $T = \frac{1}{2}\Omega_{RF}t$ and a_j and q_j are the dimensionless stability parameters that determine the stable and unstable

solutions of the Mathieu equations. We have

$$a_x = a_y = \frac{-4QU_0}{Md^2\Omega_{RF}^2} \qquad a_z = \frac{8QU_0}{Md^2\Omega_{RF}^2} \tag{1.23}$$

$$q_x = q_y = \frac{2QV_0}{Md^2\Omega_{RF}^2} \qquad q_z = \frac{-4QV_0}{Md^2\Omega_{RF}^2} \tag{1.24}$$

where M and Q are the mass and charge of the ion, respectively. In adiabatic approximation, Eq 1.22 has stable solutions if $a_j, q_j \ll 1$ where j= 1,2,3. In this case, the first order solution for the Mathieu equation is

$$u_j \approx u_0 cos(2\pi\omega_j t + \phi)[1 + \frac{q_j}{2} cos\Omega_{RF} t], \tag{1.25}$$

The secular motion of ions corresponds to a harmonic oscillation at frequency ω (macromotion) in the x, y-plane with an amplitude that is modulated at the trap frequency Ω_{RF} (micromotion). The frequency of the this secular motion is,

$$\omega_{j,RF} = \frac{1}{2}\beta_j \Omega_{RF}, \tag{1.26}$$

where $\beta_j \approx a_j + \frac{q_j^2}{2}$. The potential energy of the ions corresponds to the kinetic energy of the oscillation and potential depth generating the harmonic motion is then given by

$$D_r = \frac{QV_0}{Mr_0^2\Omega_{RF}^2} = \frac{D_z}{2}, \tag{1.27}$$

for a hyperbolic Paul trap with $r_0^2 = 2z_0^2$. If a DC voltage (U_0) is applied to the end caps in a symmetric configuration, the potential depth of the trap changes and we have

$$D_z^{'} = D_z + \frac{U_0}{2}, \tag{1.28}$$

and

$$D_r^{'} = D_r - \frac{U_0}{2}. \tag{1.29}$$

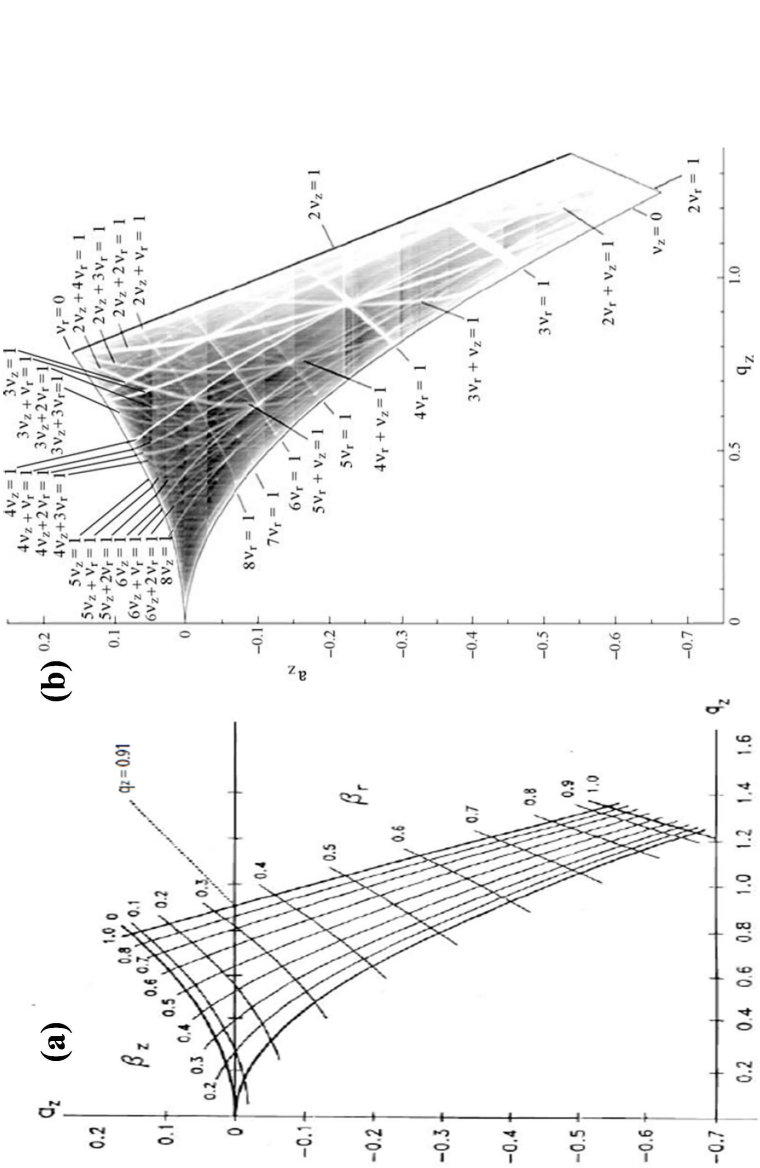

Figure 1.14.: (a) Mathieu stability diagram in (a_z, q_z) space for a hyperbolic Paul trap [73, 67]. (b) An example of the same Mathieu stability diagram for a realized trap where the extra lines represent the different parametric resonances for different values of a and q where the stable trapping of ions is not possible [70].

The stability domain in (a, q) space is shown in Fig 1.14 [74]. The maximum value q = 0.91 (for $U_0 = 0$) sets a boundary for the minimum mass/charge ratio of the particles that can be stored in a Paul trap. For high values of q, the orbits diverge and the ions are discarded from the trap (see Fig 1.14). This stability limit can be changed by an additional DC potential ($a \neq 0$). This provides for a means to expel particles with e.g. heavier mass/charge ratios. The manipulation of the trap potentials across the stability region is a substantial method to avoid trapping of undesired ions.

In this work chapter 2 gives important experimental and technical details about the setup of our particle trap. Chapter 3 discusses the line shape of molecular iodine signals which are calibrated and used further in this work for frequency locking of lasers. In chapter 4 we describe the line shape of trapped ion signals with optical Bloch equations as they were used for singly charged ions of the isotope $^{138}Ba^+$. In chapter 5 we measure and analyze spectroscopy signals of ions of the isotopes $^{134}Ba^+$ and $^{136}Ba^+$ for which an analysis method based on Fano profile treatment has been developed. This approach results in a measurement of the isotope shifts for these isotopes with respect to $^{138}Ba^+$. Chapter 6 summarizes this work in the context of associated measurements and a future parity violation experiment.

2. Apparatus and Laser System for Ba^+ Spectroscopy

For the experiments described in this thesis two hyperbolic Paul traps are set up inside two separate Ultra High Vacuum (UHV) chambers for efficient trapping and spectroscopy of heavy alkaline Ba^+ ions. One Paul trap (named as "trap 1') contains the isotope $^{138}Ba^+$ [61]. A modified version of this trap (named as "trap 2") contains two different isotopes $^{134}Ba^+$ and $^{136}Ba^+$. The "trap 2" setup is explained in detail in this chapter. Both traps use the same laser light sources and similar optical detection schemes which are also described here. Parameters which are pivotal for a precision spectroscopy such as laser frequency stability, polarization control, manipulation of detuning, beam profiles are explained in detail. The laser system is localized in laser laboratory which is separated by some 30 m from the laboratory where the traps for Ba^+ is reside. Optical fibers transport the necessary laser light from the laser lab to the Ba ion trapping lab.

2.1. Hyperbolic Paul trap

A hyperbolic Paul trap is designed to create optimal trapping conditions (see Fig. 2.2). It is made of two end cap electrodes and a center ring electrode. The chosen geometry results in a harmonic pseudo-potential at the center of the trap for an AC voltage applied between the electrodes. The end cap electrodes are grounded. The dimensions of the Paul trap are based on a prototype for storing different mass ions which had been developed at the IBM Almaden Research Center, San Jose [75].

2.1.1. Trap for Ba^+ ions

The center ring electrode and end cap electrodes are made of OFHC (Oxygen Free High Conductivity) copper which are mounted on a MACOR holder which is fixed to a copper base plate (see Fig. 2.1). The center ring electrode has a diameter $d_0 = 2.8\,\text{mm}$ and thickness $t_0 = 1\,\text{mm}$. The distance between the tips of the end caps is $z_0 = 2\,\text{mm}$ (see Fig. 2.2).

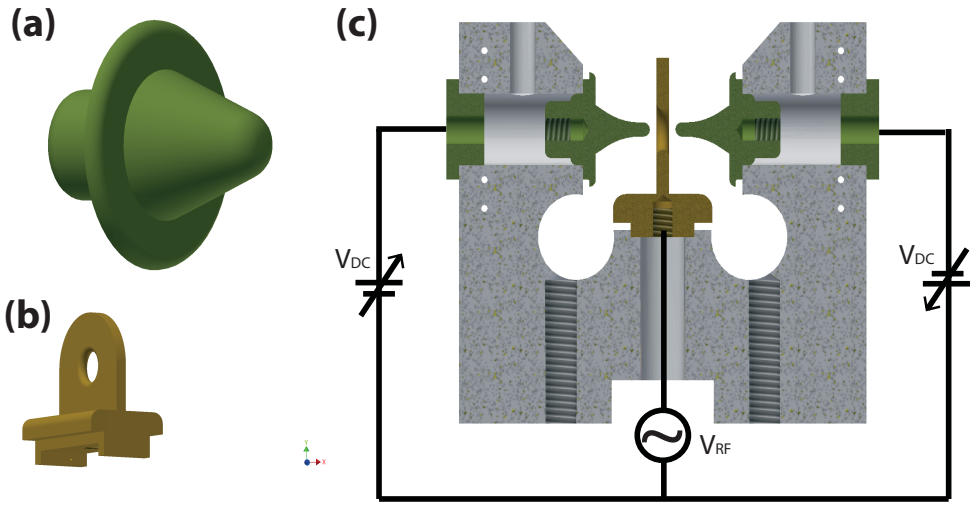

Figure 2.1.: The ring electrode and end cap electrodes of the Paul trap. (a) end cap electrode (b) center electrode (c) mounted trap with two end cap electrodes and a center ring electrode. The ions are confined in a Paul trap created by applying a rf field to the center electrode and dc voltage to the end cap electrodes. In the center of the assembly the electrodes approximate well the field geometry of a hyperbolic trap.

A holder for two Ba ovens containing $^{134}Ba^+$ and $^{136}Ba^+$ is also fixed on the copper base plate. For $^{134}Ba^+$ a mixture of 88.1($\pm$0.4)% enriched Barium Carbonate($BaCO_3$) and Zirconium (Zr) and for $^{136}Ba^+$ a mixture of 95.4($\pm$0.2)% enriched $BaCO_3$ and Zr are filled in a 0.9 mm inner diameter $\times$ 40 mm length resistively heated stainless steel hollow medical needle each (the production of atoms is explained in detail elsewhere and

can be found in, e.g. [61]). Atomic beam with a flux of the order of 10^6 atoms/s are produced when a current of typically 6.5 A, supplied by ES 015-10 power supply (Delta Elektronika) is applied to the needle.

Stray electric fields develop in the trap from residuals deposited on the electrodes when a beam of Ba atoms passes through the trap. Stray fields can also come from charges produced photo-electrically. To compensate for this, four auxiliary electrodes are mounted symmetrically around each end cap electrode. These auxiliary electrodes are made of tantalum with thickness $t_{aux} = 1$ mm and are mounted on a Macor holder which is then fixed to the Cu base plate. The base plate also has a best form lens of focal length $f_l = 40$ mm which is mounted on the lens holder for the collection of fluorescence from trapped ions in addition to an aperture to reduce the background scattering from laser beams passing through the trap. A 1 mm slit aperture is also mounted on the base plate in the direction of the entrance of the laser beams which aids in the alignment of the beams and blocks the scattering. These apertures are painted with UHV compatible black paint (MLS-85-SB) [48] to prevent reflections.

2.1.2. Electronics for generating the trapping field

The trapping potential for the Paul trap is provided by an RF electronic circuit (see Fig. 2.4). A function generator (HP3325A) provides a sinusoidal RF signal. This is then amplified with a RM-KL-500 high power linear amplifier(AMP). Higher harmonics in the signal are suppressed by a 50 Ω impedance low pass filter at 15 MHz. The amplitude of the signal is varied using a variable attenuator. The synthesizer frequency is tuned to be in resonance with an LC circuit. The transformer coil of the LC oscillator is made by winding a 0.90 mm thick silk covered 99.99% silver wire 25 times on a Teflon core. For monitoring frequency matching the RF feedback (read out) is connected to an oscilloscope. The whole circuit is enclosed in a brass cylinder to reduce sending of the RF to other sensitive electronics. The RF voltage is then applied to the center ring electrode. A balanced DC voltage of $-9\,\mathrm{V} < U_0 < 9\,\mathrm{V}$ each can be applied between the end cap electrodes.

To test the LC circuit an RF signal from a synthesizer (RIGOL DG

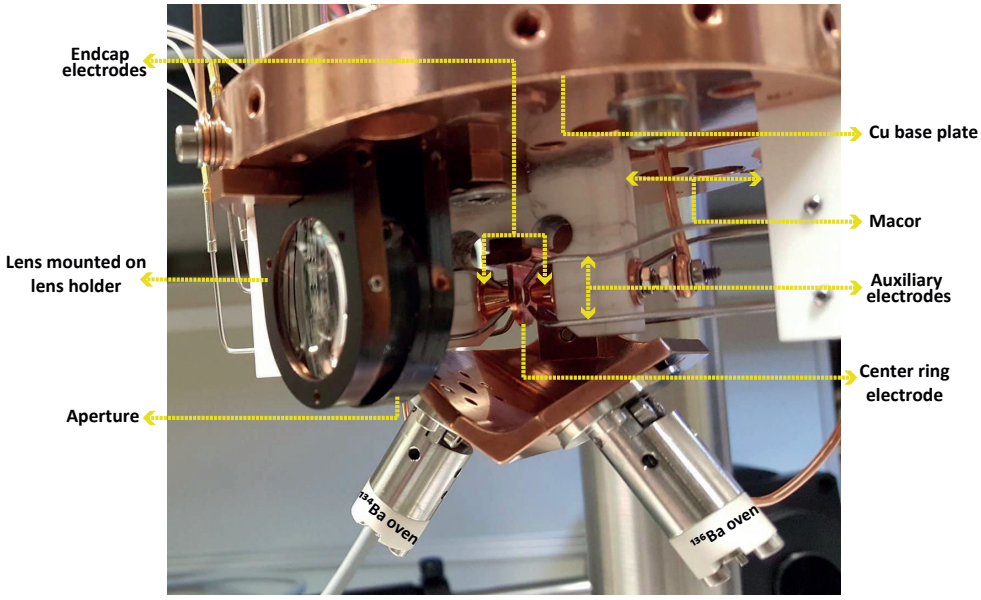

Figure 2.2.: Mounted trap assembly.The region between the end cap electrodes and the center ring electrode is the trap volume. Diameter of the center ring electrode $d_0 = 2.8\,\text{mm}$ and the distance between the end caps $z_0 = 2\,\text{mm}$. Two Ba isotopes are available, each from a different oven. The fluorescence light from the ion(s) is collected by a best form lens of focal length $f_l = 40\,\text{mm}$. The laser light passes through the middle of the center ring electrode.

4162) is fed to 'RF in' connected to the LC circuit after amplifying the signal (see Fig. 2.3(a)). A voltage probe (Tek P6139A 500 MHz, 8 pF, 10 MΩ) connected to an oscilloscope (TDS 202413) measures the voltage applied to the center ring electrode in the trap. The RF read out is also monitored on the same oscilloscope. Such a measurement confirms the reliably of tuning the synthesizer frequency to match the resonance of LC circuit. A similar measurement is done to determine the resonance frequency Ω_{RF} of the LC circuit and to calibrate the voltage at the trap by generating the RF signal from HP3325A function generator.

In order to calibrate the voltage at the trap a set of measurements is

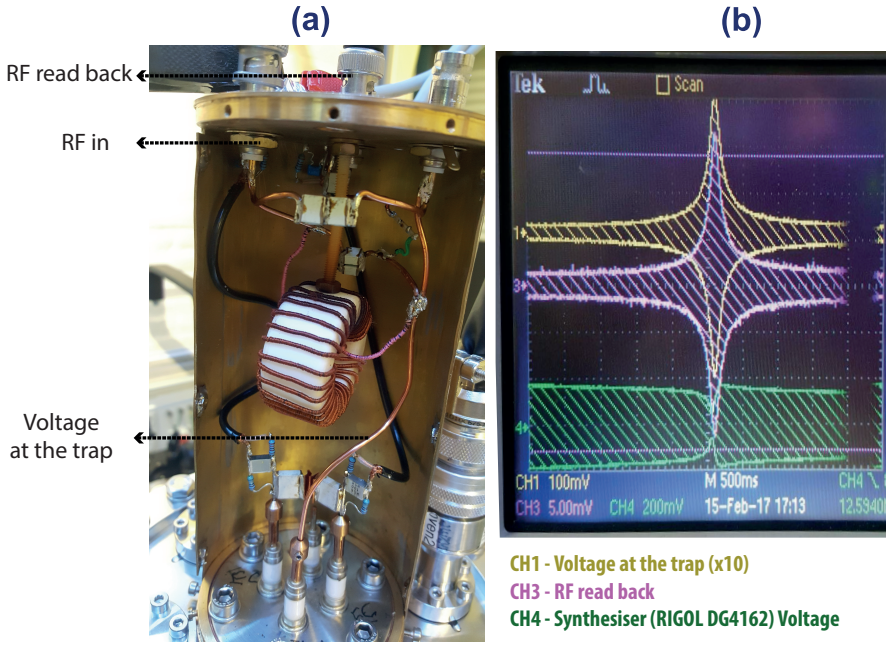

Figure 2.3.: (a) LC circuit which delivers the RF voltage to the trap after amplification. A DC voltage synthesizer (RIGOL DG 4162) provided the input voltage to 'RF in'. A voltage probe (Tek P6139A 8 MHz, 8 pF, 10 MΩ) is used to measure the voltage applied to the ring electrode in the trap. (b) Measurement to test the LC circuit and to calibrate the RF voltage at the trap. The frequency of the synthesizer(in green) is tuned to match with the resonance frequency of the LC circuit frequency (in yellow is the voltage measured at the trap and in magenta is the RF read back voltage). RF read back $\approx 31\,\mathrm{mV}_{pp}$ and RF measured at the trap $\approx 6\,\mathrm{V}_{pp}$.

done by changing the RF signal amplitude from the synthesizer and measuring the voltage at the trap and the RF read back voltage at resonance (see Fig 2.3(b)). The measured voltages for calibration of the RF voltage at the trap are tabulated in Tab. 2.1.

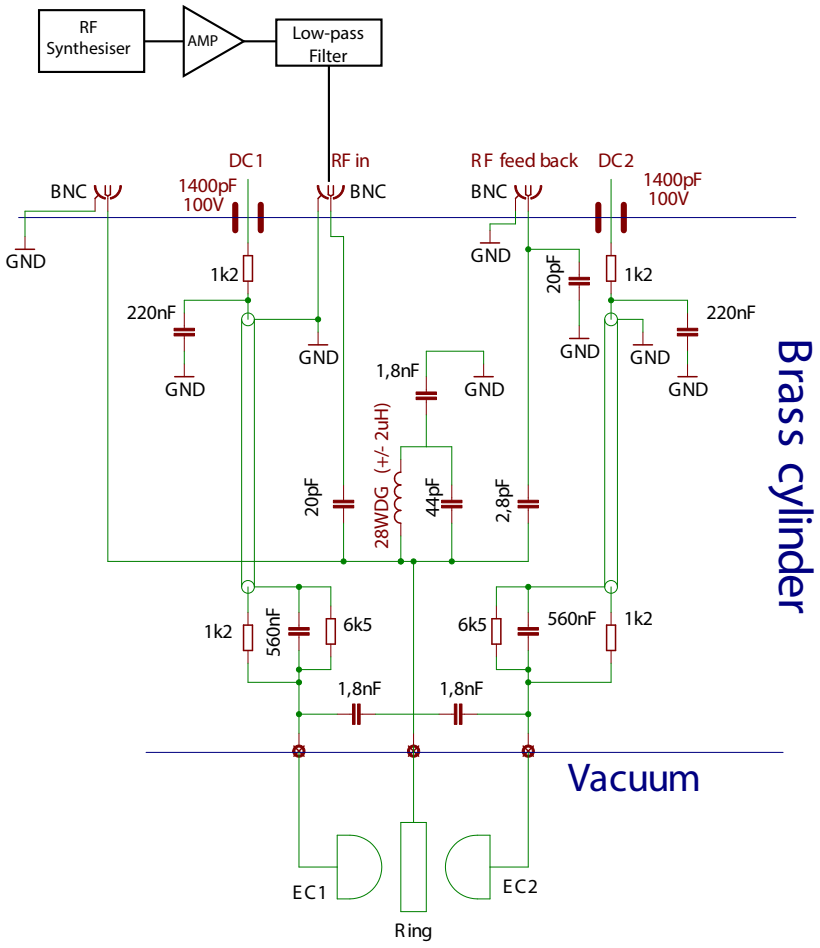

Figure 2.4.: Circuit diagram of the electronics for generating the high RF voltage from amplified and filtered sinusoidal signal.The trap is operated at RF frequency $\Omega_{RF} = 11.383(1)$MHz with a voltage amplitude V_{rf} between 100 V - 2500 V applied to the ring electrode. The LC circuit is enclosed in a brass cylinder.

In order to determine the resonance frequency of the LC circuit, the frequency of the synthesizer for different RF read out voltages are plotted. The frequency response curve of an LC circuit is fitted which is in excellent agreement with the measured points (see Fig 2.5). The resonance frequency of the circuit is determined to be $\Omega_{RF} = 11.383(1)$MHz with a Quality factor of 76.

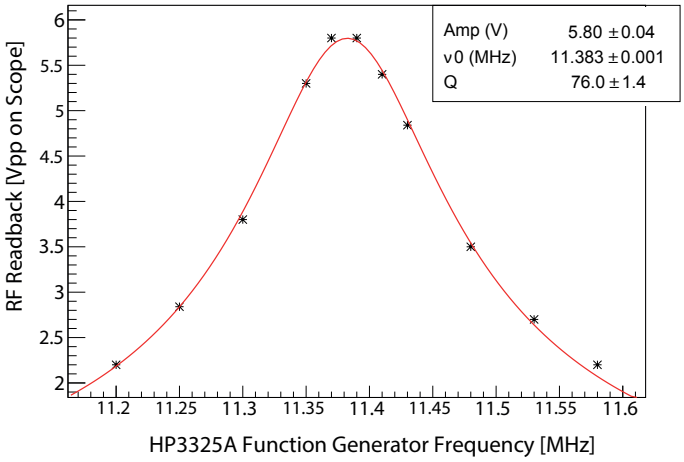

Figure 2.5.: Measurement of RF resonance in the Paul trap assembly. The RF signal is generated by HP3325A function generator. The uncertainties of the measurements are below symbol size. The curve for the frequency response of an LC oscillator is fitted which agrees very well with the measured points.The resonance frequency of the circuit, $\Omega_{RF} = 11.383(1)$MHz. The quality factor of the circuit is Q= 76.

2.1.3. Stray electric field compensation

A precision experiment involves placing the ion at the center of the RF quadrapole field with µm precision where it is less perturbed by stray electric charges and hence enhancing the life time of the ions in the trap. The micro-motion of ions are reduced when placed at a position with

Table 2.1.: Voltage calibration at the trap

Function Generator (V_{pp})	RF read back (V_{pp})	Voltage at the trap (V_{pp})	q_z
1.4	8.4	1500	0.14
0.9	56	1000	0.10
0.2	1.4	250	0.03

a minimum amplitude of the RF filed. Due to the deposition of extra charges on the electrodes, while changing the amplitude of the RF trapping field the position of the ions are displaced. To compensate for this, a DC voltage is applied to the end cap electrodes which compensates for the horizontal movement of the ions. The voltage controller is designed in such a way which makes it possible to apply a DC voltage to each end caps separately and also to both simultaneously using a common potential. The circuit connection could be found in Appendix A.

Four auxiliary electrodes are fixed symmetrically around each end cap electrode to compensate for the displacement of ion from the center of the trap due to stray electric charges. A high voltage power supply (NHQ 236L, 2×6 kV/1 mA) provides the DC voltage to each of these electrodes. The polarities for the electrodes are chosen such that the ion is placed at the center of the trapping field. The image of the trapped ions on an EMCCD camera (see Section 2.4.2) is used to monitor the movement of the ions. Fig 2.6 shows the direction in which the ions move when a voltage up to 100 V is applied to each of the electrodes. In order to calibrate the voltages applied to each of the auxiliary electrodes the relative movement of the ions are plotted against change in the DC potential applied to them (see Fig 2.7).

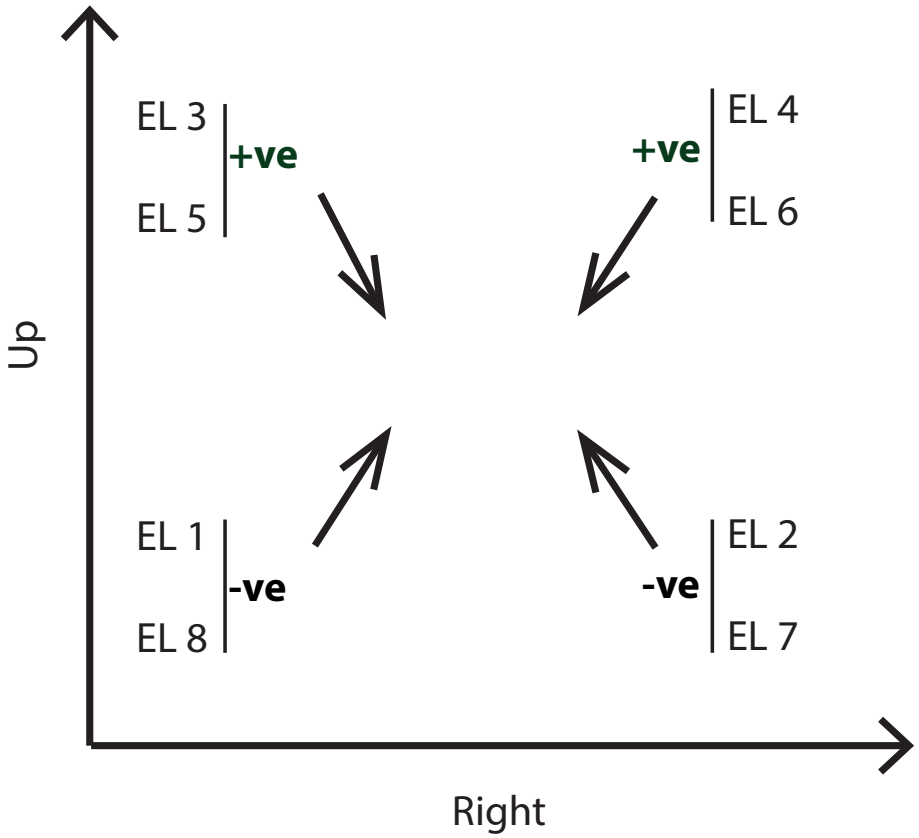

Figure 2.6.: The movement of the ion cloud as observed with the EMCCD camera by changing the voltage on the auxiliary electrodes by 100 V. EL: auxiliary electrode. The arrows show the direction in which the ions move on the camera when the high voltage is applied to each of the electrodes. The polarity of voltage applied to each of the electrodes are also indicated.

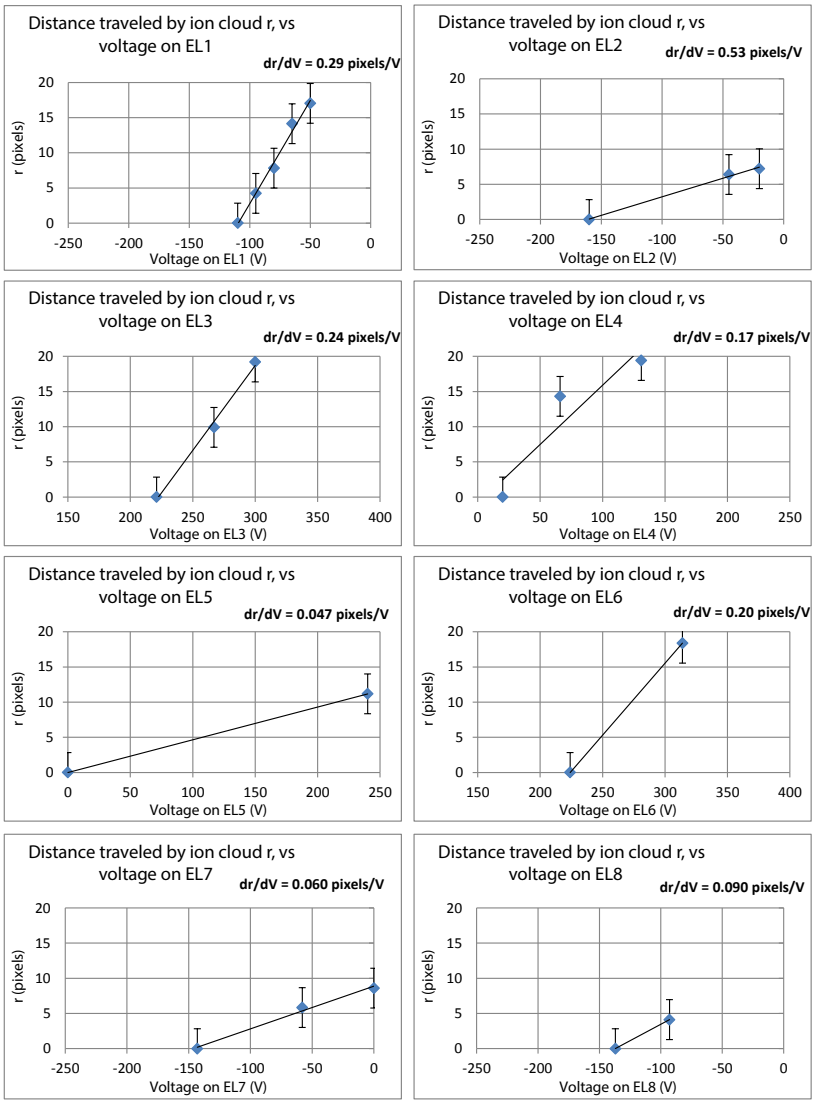

Figure 2.7.: Calibration of voltages applied to the auxiliary electrodes. The distance moved by the ions with respect to each other per volt is shown. EL: auxiliary electrode. The relative distance moved by the ions per pixel is, d_{EL1}=0.29 px/V, d_{EL2}=0.053 px/V, d_{EL3}=0.24 px/V, d_{EL4}=0.17 px/V, d_{EL5}=0.047 px/V, d_{EL6}=0.20 px/V, d_{EL7}=0.060 px/V, d_{EL8}=0.090 px/V.

2.1.4. Vacuum System

In a high precision experiment an as far as possible undisturbed system is cardinal. Collisions of the trapped ions with residual gas, for example, can shorten the lifetime of the excited atomic states as well as the lifetime of the ion stored inside the trap. In order to reduce the influence of collisions, the residual gas pressure inside the chamber is maintained below a few times 10^{-10} mbar. The hyperbolic trap is mounted on a special rotatable CF 160-flange which is fixed to an ultra-high vacuum chamber made of stainless steel (RVS 316LN), see Fig 2.8.

The operating pressure is attained as follows: (i) an oil-free roughing pump (Aneta Iwata Scroll meiser 5.3m^3/h) brings down the pressure to several 10^{-3} mbar, (ii) a turbo pump (Leybold TMP70) pumps it further down to 10^{-8} mbar and (iii) a titan ion pump (Gamma Vacuum 800) enables to reach at the operating pressure of 10^{-10} Pa. The flow of the residual gas is controlled by all metal valves in between the pumps (specifications in Appendix A). Pressure lower than 10^{-10} mbar is attained by baking the chamber to 130 °C for about three days. In order to boost the pumping speed and to maintain a constant pressure level inside the chamber, an additional 3 filament titanium sublimation pump (SUBLI-CON 360043)is operated for 3 min every week. The pressure is monitored by a Pirani gauge and by a Bayard Alpert gauge connected to an ion gauge and the current to the Titanium ion pump. In order to transmit the light at wavelengths λ_{494}, λ_{650} and λ_{413} custom AR coated glass windows are attached to stainless steel extension arms that seals the port. A set of 3 apertures coated with vacuum compatible black paint (MLS-85-SB) is placed on each side of the two extended arms to avoid stray light from the laser beams. These apertures are held inside the extended arms by means of 3 threaded rods (see Fig 2.9).

2.2. Laser system

Different light sources are employed for producing, laser cooling and spectroscopy of Ba^+ ions. Here we describe the generation of light at the required wavelengths and frequency stabilization of these lasers imple-

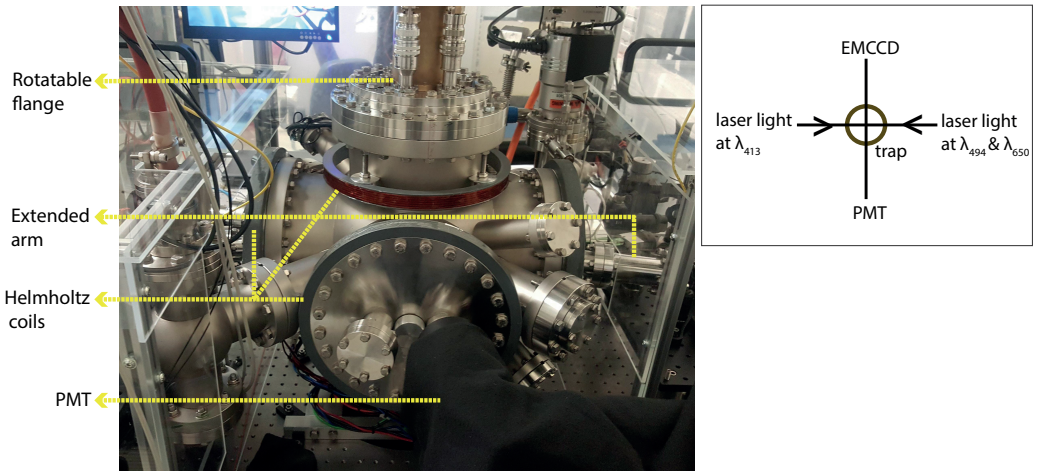

Figure 2.8.: Stainless steel ultra-high vacuum chamber containing the Paul trap. The trap is held on a rotatable CF 160-flange and is fixed to the chamber. The whole chamber is fixed on a floating optical table unperturbed by external vibrations. The axis and direction of the laser beams at wavelengths λ_{494}, λ_{650} and λ_{413} through the vacuum chamber and the axis for the detection systems, EMCCD and PMT placed outside the chamber are represented in the inset.

mented by means of absolute frequency references such as light from a frequency comb and saturated absorption spectroscopy of molecular iodine (I_2). The time base of the experiment is precisely given by a SRS Rubidium clock (FS725-10 MHz Rb, Stanford Research Systems) by providing a TTL signal at 10 MHz.

2.2.1. Photoionization laser

The creation of Ba^+ ions is done by two-step photoionization of Ba atomic beam passing through the center of the Paul trap. This process involves resonantly driving the $6s^2\ ^1S_0$ - $5d\ 6p\ ^3D_1$ transition at wavelength λ_{413} with light from an external cavity laser diode (ECDL) in Littrow configuration, Fig 2.10. The advantages of such a scheme are higher efficiency

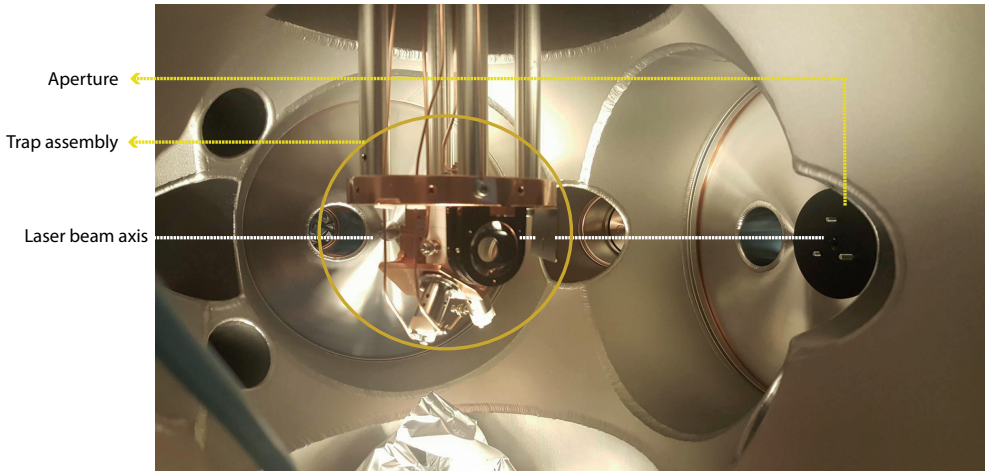

Figure 2.9.: Mounted trap inside the vacuum chamber. A set of 3 apertures coated with vacuum compatible paint are fixed on each arm to avoid stray light from the laser beams. The outer most aperture held inside an arm of the vacuum chamber by means of three long threaded rods is shown in the picture.

and the isotope selectivity [76] compared to electron bombardment technique. In addition to this, benefits like strongly reduced static charging of dielectrics [77], lower motional heating rates of the ions after loading due to the suppression of patch potentials [78] is of great advantage.

In order to achieve the wavelength λ_{413}= 413.3495(3) nm for photoionization we employ a diode laser at wavelength 405 nm (DL-5146-101S) operated at current of ≈90 mA and temperature of ≈110 °C, which is beyond the manufacturer specifications. A part of the beam, before entering the trap is split off using a beam splitter and is coupled into a wavelength meter (HighFinesse,WS/6-UV) to monitor the wavelength. The other part is tightly focused at the trap center by a lens of focal length, f_{413} = 500 mm. This beam is counter propagated with the light at wavelength λ_{494} and λ_{650} through the trap so that overlap of these beams at the trap center is ensured. The operating temperature of the diode laser is turned down to 40 °C when it is not operational for the

sake of lifetime of the diode laser.

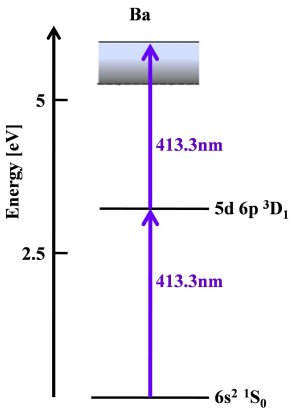

Figure 2.10.: Energy level scheme of two-step photoionization of Ba atoms. The first one couples the ground state with the 5d 6p $^3D_1$. The second photon excites the electron deeply into the continuum.

2.2.2. Optical frequency comb

An optical frequency comb consists of many continuous wave laser modes, equidistant in frequency space, which can be used like a ruler to determine large frequency differences between lasers. We employ a fiber-based femtosecond optical frequency comb (FC1500-250-WG) operated at a mode spacing of 245 MHz as a very precise frequency reference to the laser systems. The frequency of each mode is then

$$\nu_m = m \times \nu_{comb,reprate} + \nu_{comb,offset}, \tag{2.1}$$

where m is the mode number, $\nu_{comb,reprate} = \nu_{synth}/4 + 245\,\text{MHz}$ is the repetition rate of the laser pulses where ν_{synth} is the synthesizer frequency and $\nu_{comb,offset}$ is the carrier-envelop offset frequency.

The frequency comb is disciplined by an SRS Rubidium frequency standard which in turn is locked to an external frequency 1pps GPS signal. Hence the frequency comb obtains a frequency stability of better than

10^{-12} in 100 s. The long term stability of the offset beat and repetition rate of the frequency comb is show in Fig 2.11.

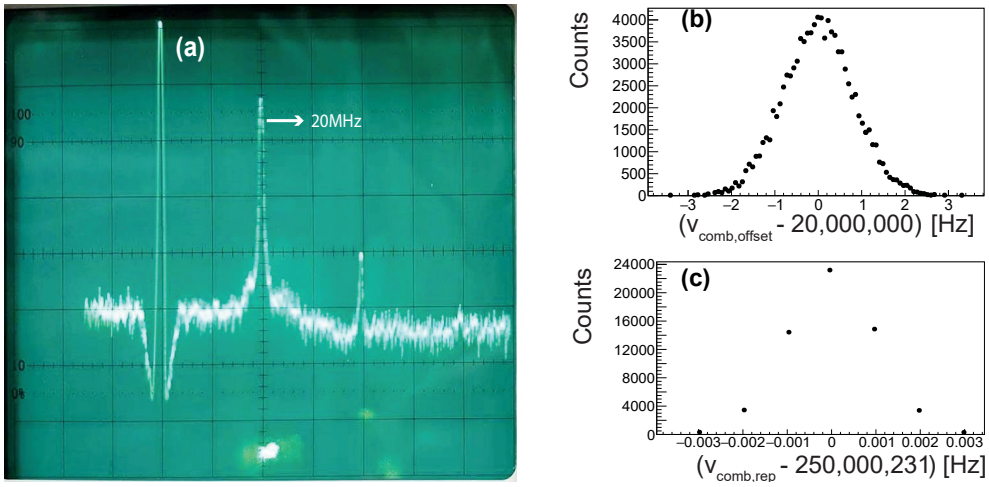

Figure 2.11.: (a) Offset beat note displayed on the oscilloscope is shown on the left side. The offset frequency is locked to 20 MHz. The long term stability of offset beat (b) and repetition rate (c) of the frequency comb.

2.2.3. Iodine-stabilized diode laser

An iodine-stabilized diode laser is used as a secondary frequency reference for the experiment. The light at wavelength 650 nm is generated from an ECDL (HL6366DG/67DG) in Littrow configuration operated at a current of 153 mA and temperature of 40.2 °C. This laser light has a typical linewidth of order 2 MHz and provides about 30 mW of light for the experiment. For short-term frequency stability the diode laser frequency is locked to a transition in molecular iodine (I_2). A narrow line from the hyperfine structure in the molecule is employed for this purpose by high resolution saturated absorption spectroscopy of molecular I_2. A detailed explanation of the experimental set up and frequency-modulated saturated absorption spectroscopy of I_2 is given in Chapter 3. The dye

laser light uses the light from the iodine-stabilized diode laser as the reference frequency (see Section 2.2.4). In order to achieve long-term frequency stability a small fraction of the light from the diode laser is split off and overlapped with light from the frequency comb on a photodiode which has a nonlinear response to the electric field of the light wave. The beat note is used for phase locking the diode laser to a particular line in the spectrum of the optical frequency comb. The absolute frequency of the diode laser is then

$$\nu_{diode} = m \times \nu_{comb,reprate} + 2 \times \nu_{comb,offset} + \nu_{B_2}, \tag{2.2}$$

ν_{B_2} is the beat note frequency between diode laser and frequency comb. The stability of this beat note is within ±(80 - 90)kHz (see Fig 2.12).

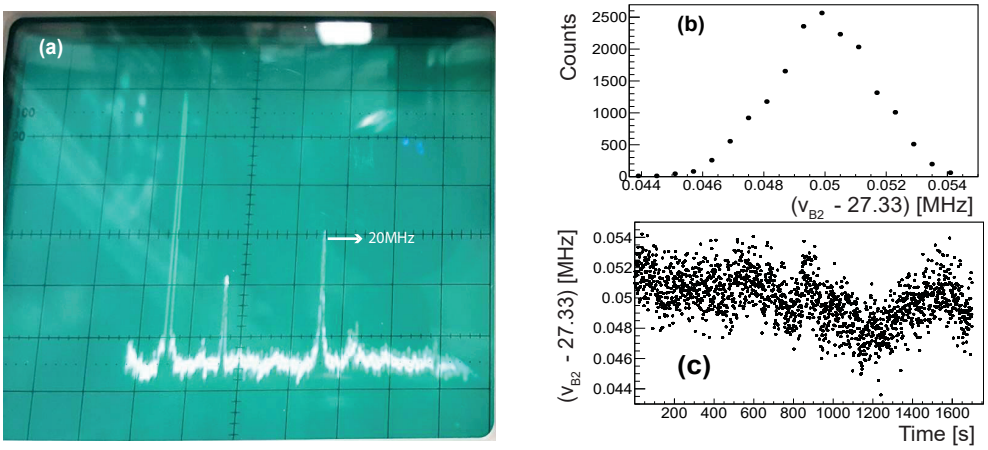

Figure 2.12.: (a) Beat note signal of iodine stabilized-diode laser with the frequency comb displayed on an oscilloscope. Example of (b) beat note signal and (c) the long term stability of this beat note signal which stays within 5 kHz.

2.2.4. Dye laser

The light at wavelength $\lambda_{650} = 650\,\text{nm}$ is generated by a Coherent CR-699 ring dye laser (Coherent Inc. Palo Alto, USA) by optically pumping

the DCM
(4-(dicyanomethylene)-2-methyl-6-(p-dimethylamino styryl)-4H-pyran) dye dissolved in benzyl-alcohol by a Coherent Verdi-V10 diode pumped solid state laser. This laser has a linewidth of 500 kHz and delivers output power in the range 80-100 mW at wavelength of λ_{650} with a pump power of 1.8 W. This light is transported to the laboratory where the ion traps are located via a 100 m long single mode optical fiber. A part of the light is split off and coupled to a wavelength meter (WS6 VIS, HighFinesse-Angstrom) to monitor the wavelength.

The short-term stability of the iodine-stabilized diode laser is to the dye laser by the method of frequency offset locking. Light from the dye laser and the iodine-stabilized diode laser are overlapped on a photodiode (PDS02). This beat note signal is then monitored with a 1 GHz spectrum analyzer (HM5510). For a very stable frequency with a slow drift the beat note frequency is compared with a reference frequency from an rf-synthesizer using a phase locked loop (PLL) circuit (ADE4007). The error signal produced by this PPL is fed back to the laser via a PID control which permits the selection of the desired frequency while stabilizing the frequency difference. The absolute frequency of the dye laser light is then

$$\nu_{dye} = \nu_{diode} + \nu'_{B_2}, \tag{2.3}$$

where ν'_{B_2} is the beatnote frequency between the light from the diode laser with light from the dye laser. A photograph of the display of the spectrum analyzer showing the beatnote between the light from the diode laser with light from the dye laser is shown in Fig 2.13. This dye laser light at λ_{650} is then transported to the Paul trap.

2.2.5. Ti:sapphire laser and frequency doubling

The light at wavelength $\lambda_{494} = 494$ nm is generated by second harmonic generation of light from optically pumped single mode Ti:Sapphire laser (Coherent MBR-110) by a diode pumped solid state laser (Coherent Verdi-V10). The power delivered at 7 W of output pump power at wavelength of Ti:Sapphire $\lambda_{987} = 987$ nm is typically 300 mW. This light has a linewidth of about 500 kHz. A part of the light is split off using a beam

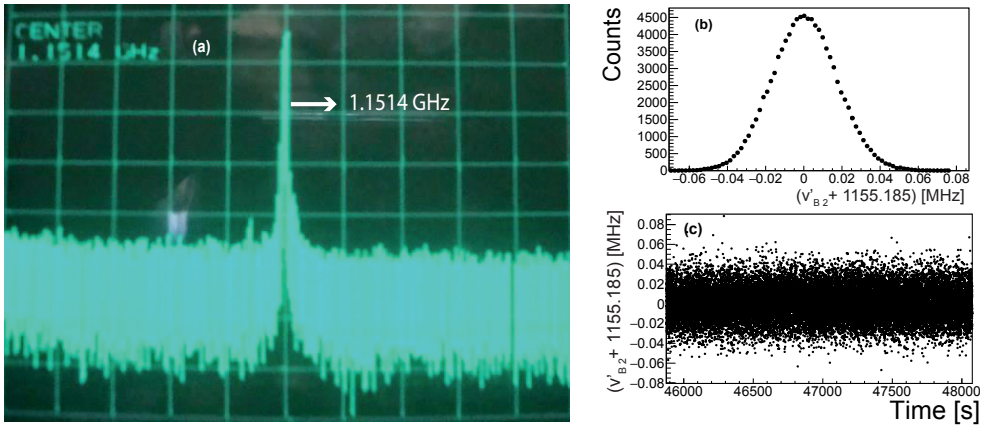

Figure 2.13.: (a) Offset beat note signal of dye laser with iodine stabilized-diode laser displayed on a spectrum analyzer. (b) Example of offset beat note of dye laser with iodine stabilized-diode laser. (c) The long term stability of the beat note.

splitter and is monitored on a wavelength meter. Frequency stabilization of Ti:Sapphire laser light to better than 100 kHz is achieved by locking it to the frequency comb (see Fig 2.14). The absolute frequency of this light at wavelength λ_{987} is then given by

$$\nu_{987} = m \times \nu_{comb,reprate} + 2 \times \nu_{comb,offset} + \nu_{B_1}, \tag{2.4}$$

where ν_{B_1} is the beatnote frequency between TiSa laser and frequency comb. The sign of the beat note is verified by modifying the frequency comb reference. The light at wavelength λ_{987} is transported to the laboratory where the ion traps are located via a 100 m long single mode optical fiber. Around 150 mW is coupled into an enhancement linear cavity. In the focus of the cavity a MgO-doped PPLN crystal (Covesion MSHG976-0.5-xx) is placed. The crystal is temperature tuned to achieve quasi phase matching at t=159 °C. This produces laser beam at wavelength λ_{494} with 10 mW of power. This light is then transported to the Paul trap.

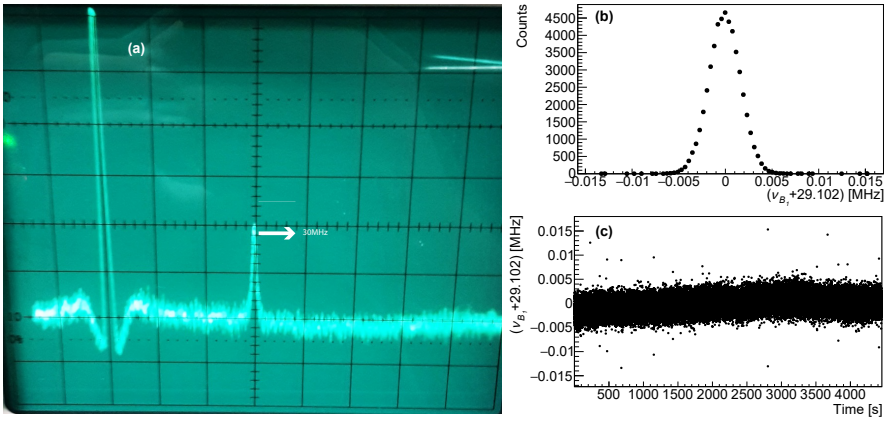

Figure 2.14.: (a) Beat note signal for light at wavelength λ_{987} with the frequency comb displayed on the oscilloscope. Example of (b) a beat note signal and (c) the long term stability of this beat note signal which is better than 10 kHz over typical hours.

2.3. Beam diagnostics and manipulation

Before entering the Paul trap the laser light at wavelength λ_{494} is passed through an Acousto-Optic Modulator (AOM-494) and the laser light at wavelength λ_{650} is passed through a double pass AOM (AOM-650) to shift the light frequency and for stabilizing the power. The double pass AOM-650 helps for directional stability.

RF frequency for the AOM-494 is provided by a signal generator HP8657B for spectroscopy and for the AOM-650 is provided by HP8656B signal generator. The intensity of this beam depends on the RF power applied to the AOMs. The first order diffracted beam for light at wavelengths λ_{494} and λ_{650} from the AOM-494 and AOM-650 respectively is coupled to the trapping set up via a single mode optical fiber. The center frequency of the RF synthesizer used for spectroscopy for the blue light is given by $\nu_{AOM-494}$ = 198.9 MHz and that for the red light is given by $\nu_{AOM-650}$ = 362 MHz.

Here we describe the manipulation of the timing and detuning of light

at wavelength λ_{494} and λ_{650} for high resolution spectroscopy. The laser light intensities, polarization, detuning and the beam profiles are the important parameters that are controlled and recorded. The determination of laser frequencies in the trap with the intermediate frequencies involved are given. The distribution of light to the trapped ions is described.

2.3.1. Timing and detuning control

A high precision measurement requires to have constant intensity of the laser lights at wavelengths λ_{494} and λ_{650} during the spectroscopy. In addition, efficient trapping of ions involve keeping the temperature of the ions constant at optimized frequency detunings for cooling. Hence cooling the ion for long time relative to probing the atomic transition is necessary. This is achieved by using an RF switch (Mini-Circuits ZASW-2-50) that selects the frequency of the acousto-optic modulators, $\nu_{AOM-650}$ between two frequencies $\nu^1_{AOM-650}$ and $\nu^2_{AOM-650}$ and for $\nu_{AOM-494}$ between $\nu^1_{AOM-494}$ and $\nu^2_{AOM-494}$. The frequencies $\nu^1_{AOM-494}$ and $\nu^1_{AOM-650}$ probes the atomic transition while $\nu^2_{AOM-494}$ and $\nu^2_{AOM-650}$ cools the ion. The timing between these two frequencies is manipulated by a switching frequency ν_s which is controlled using a square pulse signal from a function generator ranging from 1 kHz to 300 kHz. The duty cycle for AOM-494 and AOM-650 could be varied between 10% and 90%. The signals are recorded and sorted in the DAQ for the period of cooling and probing using a frequency counter. The duty cycle of the counter can be varied to synchronize with the switching. We observe a time delay, t_d between the gating time period for switching and for counting the frequency, due to which about 5% of the signal from cooling is leaked into the spectroscopy signal during the switching (see Fig 2.15). The time period for which the laser lights are used for spectroscopy is given by T_S and the time period for which the laser lights are used for cooling is given by T_C. Therefore, the switching frequency is given by,

$$\nu_s = \frac{1}{(T_S + T_C)}. \tag{2.5}$$

Manipulating the frequency of the light at wavelength λ_{650} is done by simultaneously scanning the frequency ν'_{B_2} and the frequency $\nu^2_{AOM-650}$

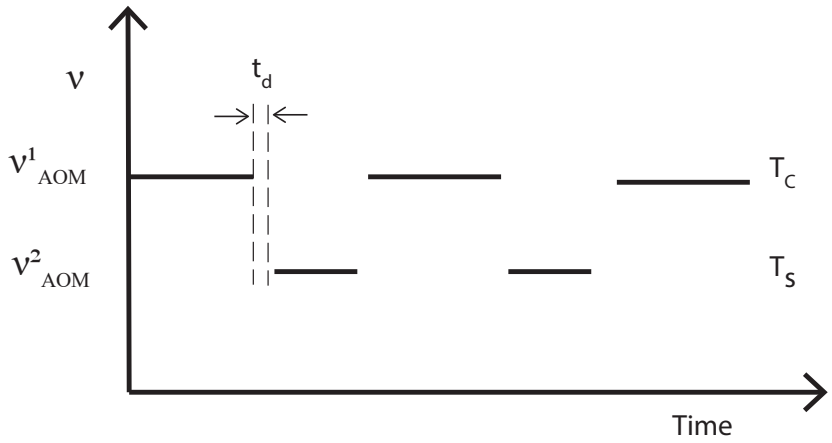

Figure 2.15.: The timing control of laser light frequencies for cooling and for spectroscopy of trapped ions. Duty cycle is set for switching the frequencies for spectroscopy and for cooling the trapped ions. ν^2_{AOM} represents the frequency of light optimized for probing the atomic transition and ν^1_{AOM} represents the frequency of light optimized for cooling. There is a time delay t_d between the time period for spectroscopy T_S and the time period for cooling T_C.

with a Voltage Controlled Oscillator (VCO) such that the frequency of light at wavelength λ_{650} is kept constant.

Manipulating the frequency of light at wavelength λ_{494} is done by controlling the frequency $\nu^2_{AOM-494}$ by an additional signal generator HP8644A. The center frequency of this synthesizer is varied, such that $\nu^2_{AOM-494}$ is optimized at a frequency detuning resulting in a constant cooling and $\nu^1_{AOM-494}$ is optimized at a different detuning where the atomic transition is probed simultaneously.

Laser light frequencies in the trap

After the frequency stabilization and power stabilization, the frequency of the light in the trap at wavelengths λ_{494} and λ_{650}, denoted by ν_1 and

ν_2 respectively are given by,

$$\nu_1 = 2 \times (\nu_{comb,offset} + m_1 \times \nu_{comb,rep} + \nu_{B1}) + \nu_{AOM-494} \tag{2.6}$$

$$\nu_2 = \nu_{comb,offset} + m_2 \times \nu_{comb,rep} + \nu_{B_2} + \nu'_{B_2} + 2 \times \nu_{AOM-650} \tag{2.7}$$

2.3.2. Delivery of laser beam to the trap

The light at wavelengths λ_{650} and λ_{494} is brought to the experimental table via a single mode optical fiber (Thorlabs, 460HP, 10-C0157-10-3D-12). The beam after passing through a set of achromatic lens with focal length, $f_1 = -20\,\text{mm}$ and $f_2 = 300\,\text{mm}$, is steered using mirrors to direct it to the trap and to focus it at the trap center.

Two wavelength selective quarter wave plates are fixed back to back on two separate rotational mounts on the beam path before the beam enters the trap. This is done in order to manipulate the polarization of the two beams independently by an appropriate choice of the two rotation angles.

The laser light at wavelengths λ_{494} and λ_{650} before entering the trap is split off using a beam splitter as shown in Fig. 2.17. It is imaged on a CCD camera (Thorlabs, DCU223M) which has a pixel size of 4.65 µm x 4.65 µm. The distance between the beam splitter and the sensor of the camera is equal to the distance between the beam splitter and the center of the trap. This makes it possible to estimate the beam properties at the position of the ion. Fig. 2.16 shows the CCD image of the laser beam at wavelengths λ_{494} and λ_{650}. The beams after going through the trap are split off using a beam splitter to two photo diodes with the appropriate filters for light at wavelengths λ_{494} and λ_{650} in order to monitor the power.

The laser light at wavelength λ_{494} has a beam diameter, d_{493nm} = 55(2) µm and the one at the wavelength λ_{650} has a beam diameter, d_{650nm} = 80(2) µm. We observe that the red and the blue beams do not overlap with each other perfectly because of the imperfections in the manufacturing of the commercial lenses and fiber couplers. Due to this the ion signal is very sensitive to the overlap of beams with the ion. A movement of the laser beam by less than a beam diameter imaged on the camera caused the signal to drop by a factor of 2.

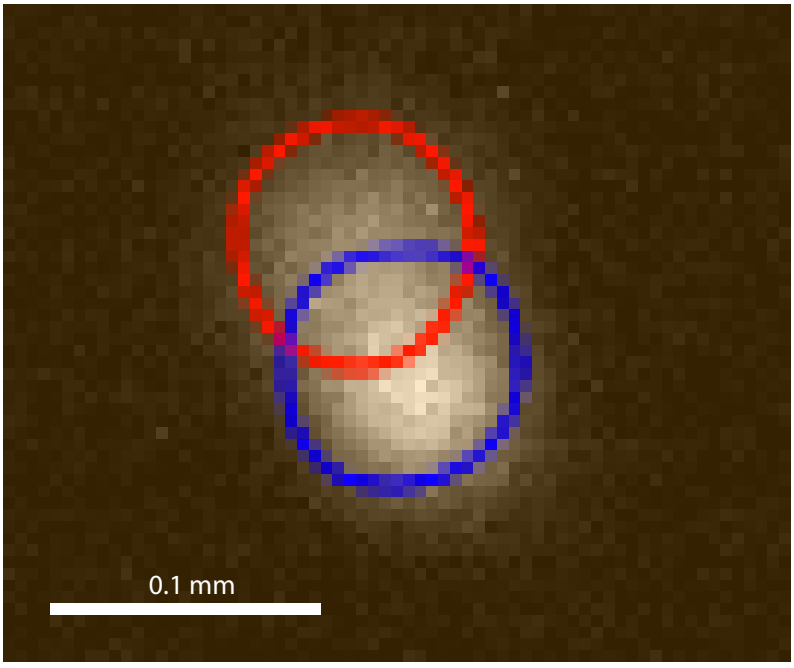

Figure 2.16.: Overlap of laser beams at wavelengths λ_{494} and λ_{650} at the trap center imaged on CCD camera. The blue beam has a beam diameter of d_{493nm}=55(2) µm and red beam has d_{650nm}=80(2) µm. The blue circle and red circle roughly sketch the position of the beams.

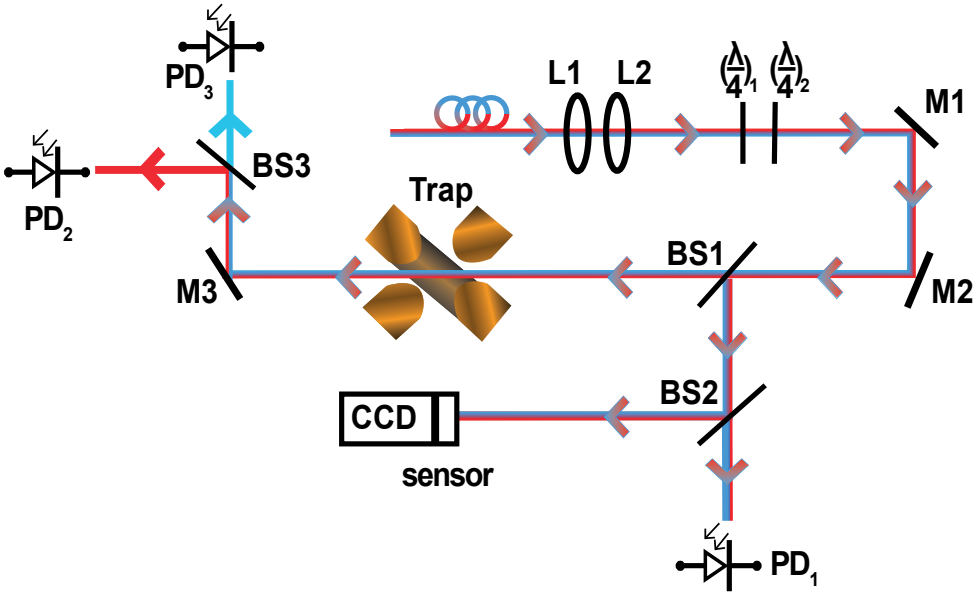

Figure 2.17.: Setup for monitoring the position of the beam on the CCD camera(Thorlabs, DCU223M). L1 and L2: Lenses for focusing the beam at the trap cente; L1 $=-20\,\mathrm{mm}$ and L2 $= 300\,\mathrm{mm}$. $(\lambda/4)_1$ and $(\lambda/4)_2$: quarter wave plates for controlling the polarization of the beams. M1 and M2: Mirrors to steer the beam to the trap center, M3: Mirror to steer the beam to a beam splitter, BS1: Beam-splitter to split off the beam going to the trap, BS2: Beam-splitter to split off the beam to image on the CCD and to a photo diode PD_1 to measure the power of the beams on the incoming side, BS3: beam splitter to split the beams on the outgoing side to photo diodes PD_2 and PD_3 to monitor the power of the light at wavelengths λ_{494} and λ_{650} respectively. Monitoring the beam in this way makes it possible to characterize the beam properties at the position of the ion.

2.4. Detection System

A Photo Multiplier Tube (PMT) and an Electron Multiplying Charge Coupled Device (EMCCD) are used for the detection of fluorescence from the trapped ions. The PMT provides for the temporal resolution and the EMCCD provides for the spatial resolution. The position of the detectors with respect to the vacuum chamber is shown in Fig 2.8.

2.4.1. Photo Multiplier Tube

A PMT (Hamamatsu H11123) is used for a high sensitivity photon counting in our experiment. The fluorescence from the ions is collected initially by a 40 mm best form lens mounted on the Cu base plate inside the vacuum chamber (see Fig 2.8) and this is then collimated on the PMT. The detection efficiency of the PMT is determined by the individual transmission of the different optical elements making up the PMT system, the solid angle for light collection and the quantum efficiency of the PMT. This is given by,

$$\varepsilon = QE \times \Omega \times T_{windows} \times T_{optics} \times T_{apertures} \times T_{filters}. \qquad (2.8)$$

where QE is the quantum efficiency of the PMT which is about 0.1, Ω is the solid angle subtended = 0.05 sr, $T_{windows}$, T_{optics}, $T_{apertures}$ and $T_{filters}$ represents transmission through windows, optics, apertures and filters. An overall detection efficiency of 10^{-6} for the PMT system is estimated considering these parameters. The scattering rate of a single cooled Ba^+ ion is about 10^8 photons/s, and hence the signal of a few times 10^2 cnts/s is obtained (see Fig 2.18). which is comparable to the typical dark count rate of the PMT at room temperature. This count rate can be further reduced by cooling the cathode of the PMT with a Peltier element. Therefore, the operating temperature of the PMT cathode is set to T_{PMT}=13 °C where we have in our laboratory the dew point. The dark count rate is then reduced to 60 s^{-1} in our new "trap 2" setup. The PMT signal is read out with a time resolution of 100 ms.

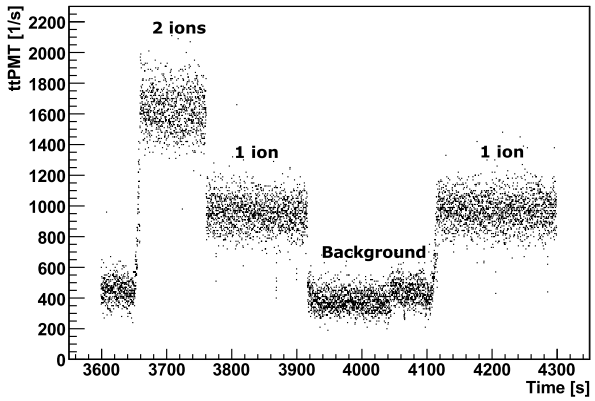

Figure 2.18.: PMT count rate from the trapped Ba^+ ions. Rate of photons scattered per ion could be determined from such a step on the PMT counter when an ion is lost from the trap (approximately 400 counts/s in this case). The background count rate is due to the scattering of laser light inside the vacuum chamber.

2.4.2. EMCCD

The trapped ions are imaged on an EMCCD (Andor iXon Ultra) camera with 512 x 512 pixels. This camera has an internal cooling system to reduce image noise. For each image the electron multiplying gain, the binning, the exposure time, frame rate etc. can be selected. The sharpness of the image is adjusted by moving a lens in the camera assembly along the axis of the trap. The image on the EMCCD is used to monitor the movement of the ions due to stray electric fields inside the trap so that active compensation can be done.

2.5. Magnetic field calibration

A defined magnetic field of the order of 80 µT removes the degeneracy of the Zeeman sublevels by sufficiently splitting them [79]. A pair of 3 Helmholtz coil each is fixed on all three axis the vacuum chamber so that

the magnetic field at the center of the trap is canceled and a homogeneous static magnetic filed is applied. The axis in which the laser beams are transmitted through the trap is defined as y-axis, the axis in which the detectors are placed is defined as x-axis and the axis perpendicular to these is defined as z-axis as indicated in Fig 2.19. This field defines the quantization axis. The magnetic filed at the center of the chamber, where the trap sits is measured using a Gauss meter (Model VGM, AlphaLab Inc.) and it is calibrated for the three axises as B_x= 0.72(5) G/A, B_y= 0.71(6) G/A and B_z= 2.12(2) G/A (see Fig 2.20).

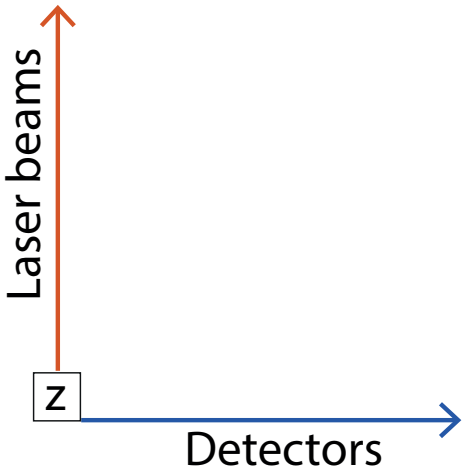

Figure 2.19.: The defined axis for the set of 3 pairs of Helmholtz coils. The y- axis is the axis of the laser beams through the trap, the x-axis is the axis in which the detectors are placed with respect to the vacuum chamber and the z-axis is the vertical axis perpendicular to the other two axes.

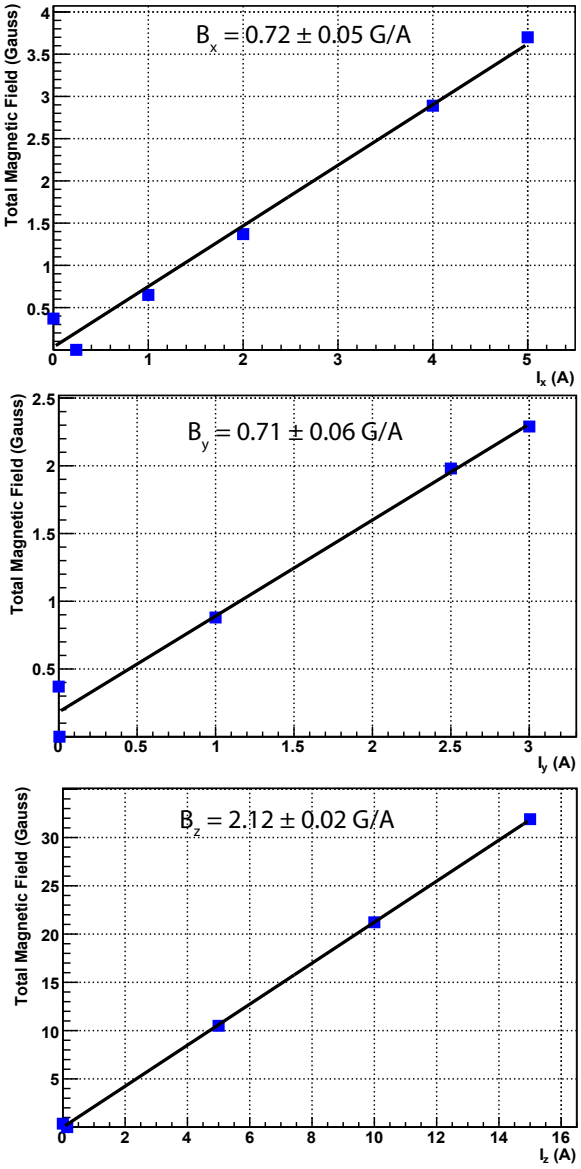

Figure 2.20.: The total magnitude of the magnetic field measured at the center of the vacuum chamber where the trap is placed for currents applied to the Helmhotz coils in the x, y and z direction. The total magnetic field at the center is zero at currents of $I_x = 0.24(2)$A, $I_y = 0.005(1)$A and $I_z = 0.14(1)$A in the z, y and z direction, respectively.

2.6. Section summary

A new hyperbolic Paul trap (trap 2) with some factor of 2 smaller dimensions has been set up to trap Ba^+ ions in an ultra high vacuum chamber at residual gas pressure of $<10^{-10}$ mbar. The RF circuit required to generate the trapping field is explained. Calibrating the auxiliary electrodes permits to apply the sufficient high voltages to compensate for the stray electric fields inside the trap which displaces the ion from the trap center. The laser systems required for the production of Ba^+ ions and for laser cooling including the set up for frequency stabilization is given. Set up for manipulating and recording the essential parameters such as laser light polarization, intensity, detuning, beam profile etc are implemented. Optical detection scheme for the trapped ions are set up using a PMT for time resolution and an EMCCD for spatial resolution.

3. Line Shape of Molecular Iodine in Frequency Modulation Spectroscopy

Frequency modulation (FM) spectroscopy is often employed in order to create a dispersive line shape for precision frequency determination and for frequency locking of lasers. Hyperfine transitions in molecular $^{127}I_2$ are widely employed as reliable frequency reference for laser stabilization in wavelength range of 500 nm - 900 nm [80]. The R(25)(6-5) transition in molecular I_2 is less than 485 MHz above the $6p^2P_{1/2} - 5d^2D_{3/2}$ transition in Ba^+ [81]. A narrow line from this spectrum is employed to stabilize the frequency of the light at wavelength 649.86 nm from a grating stabilized diode laser.

The line shape of signals from frequency modulated saturated absorption spectroscopy of hyperfine transitions in $^{127}I_2$ is affected by external parameters on the signal. The line shape obtained by FM spectroscopy are dispersive, i.e. with a zero-crossing at resonance. This shape is ideal as a reference point for the laser for frequency stabilization. However, the zero crossing is only at the center of the resonance line, if the line shape is symmetric around the line center. This symmetry can be broken in the experimental realization due to asymmetries in the modulation pattern. Such may arise from nonlinearities in the modulation amplitude and higher harmonic functions contained in the modulation frequency. Measuring the full line shape and analyzing it are relevant to estimate density shift, density broadening and hyperfine splitting. This requires the incorporation of all parameters in an experiment that can affect the line shape into the description of it. The derived line shape provides consistent results for line center, density broadening and density shift of spectral lines to 10^{-11} relative accuracy. Residual amplitude modulation,

which is inherent in modulation spectroscopy induces shifts of the zero crossing of the dispersive line shape.

3.1. Experimental Setup

A Doppler-free saturation absorption spectroscopy is achieved with counter-propagating beams passed through I_2 vapor cell which is placed inside a temperature controlled oven, Fig. 3.1. The vapor cell has a diame-

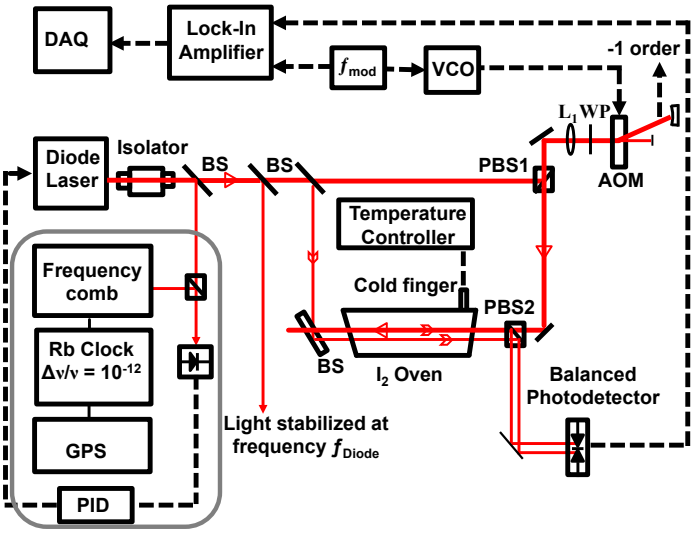

Figure 3.1.: Schematics of optical setup for the saturation absorption spectroscopy in molecular I_2. The gray frame indicates how the frequency stability is realized for the diode laser. Black dotted lines indicate the electric path and red lines indicate the optical path. BS: Beam Splitter, VCO: Voltage Controlled Oscillator, PBS: Polarizing Beam Splitter, L: Lens, WP: Wave Plate, PID: electronics servo loop

ter of 12 cm and a length of 70 cm. The cell temperature is maintained at 63 °C but is designed and fabricated for reaching temperatures up to 600 °C [82]. This particular I_2 cell was employed for absolute frequency calibration in a measurement of the two-photon 1S-2S transition in muo-

nium [18]. The vapor pressure of the molecular I_2 in the cell can be controlled by the temperature of a cold finger outside of the oven. The transmitted strong beam (pump beam) is directed through a polarizing beam splitter (PBS1) for double passing through an Acoustic-Optical Modulator (AOM). This AOM which is driven by an RF power amplifier (ZHL-1-2W) provides the frequency modulation for the pump beam. This creates different orders of diffraction. The separation between the zero order and the first order beam is 15 mrad. The zero order beam is blocked with an iris diaphragm and the first order is used as the modulation frequency. The polarizing beam splitter cube (PBS2) is used to superpose the pump and probe beams. The double pass AOM helps to improve optical isolation, intensity noise suppression and fast frequency modulation. The frequency modulation is provided by a Voltage controlled oscillator (ZOS-100+, 12 V) operated at the center frequency, $f_{mod} = 73$ MHz while maintaining pointing stability. This is attained by applying a voltage of certain amplitude between 100-800 mV and an offset voltage of 3.7 V using a waveform generator (HP 3314A). The typical modulation frequency and modulation depth which can be as large as 6 MHz are further controlled by this waveform generator.

The demodulated first derivative signal of the Lorentzian absorption signal is obtained with a 1- 100 kHz lock-in amplifier (Scitech, 420 dual phase lock-in amplifier). The main achievement of lock-in detection is that it filters a small-amplitude signal from a seemingly overwhelming amount of noise [81]. We make advantage that the output of the lock-in detector is proportional to the derivative of the absorption signal. The line shape of first harmonic, second harmonic and third harmonic of the modulation frequency is shown in Fig. 3.2. The first harmonic output signal generated by lock-in detection has a higher signal to noise ratio than the second or third harmonic. However the slope at the zero-crossing is less steep. The signal is hence less sensitive to a frequency change. Also, since the response of the lock-in detector is dispersive, it can be used for stabilizing the frequency modulated laser. The steep slope around the zero-crossing is a property of the lock-in response that can be used for stabilizing the laser frequency. The low noise balanced photo-detector signal together with the modulated signal are fed to the

lock-in amplifier. The frequency of the diode laser at 650 nm is stabilized by phase locking it to a frequency comb which transfers the stability of the GPS disciplined Rb clock of 10^{-12} optical range.

3.2. Doppler-free saturated absorption spectroscopy

The resolved Doppler free frequency modulated hyperfine spectrum of the transition in iodine is predicted by the Iodine Spec program based on model descriptions of the hyperfine and rovibronic structures [83]. The saturated absorption spectrum of R(25)(6-5) transition of $^{127}I_2$ at 649.86 nm after demodulation is shown in Fig. 3.3. The spectroscopy is carried out by scanning the laser frequency, ν_{diode} (see Eq. 2.2)by changing the reference frequency of the frequency comb in discrete steps for acquisition times of 100 ms per data point. The spectra is recorded by changing $\nu_{com,rep}$ in steps of 0.25 Hz yielding a frequency step size of 0.461 312 MHz on the laser frequency. In the spectrum, some weak lines are visible under the strong ones which are not listed in the Iodine spec program. Also, the program assumes a constant line width, and hence generates the hyperfine lines which look different in amplitude to those observed during the spectroscopy.

The first three hyperfine lines are selected for recording and further analysis since those are well separated from the rest and hence less perturbed by the neighboring lines.

3.3. Vapor Pressure dependence

The change in vapor pressure, which is essentially achieved by changing the cold finger temperature affects the I_2 hyperfine lines. A careful study is required to quantify this. The vapor pressure not only affects the amplitude, but also the line width and center frequency of the signal. A large uncertainty arises from the determination of the vapor pressure by changing the cold finger temperature because it takes approximately 30 min for the temperature to settle to the set value. The iodine vapor

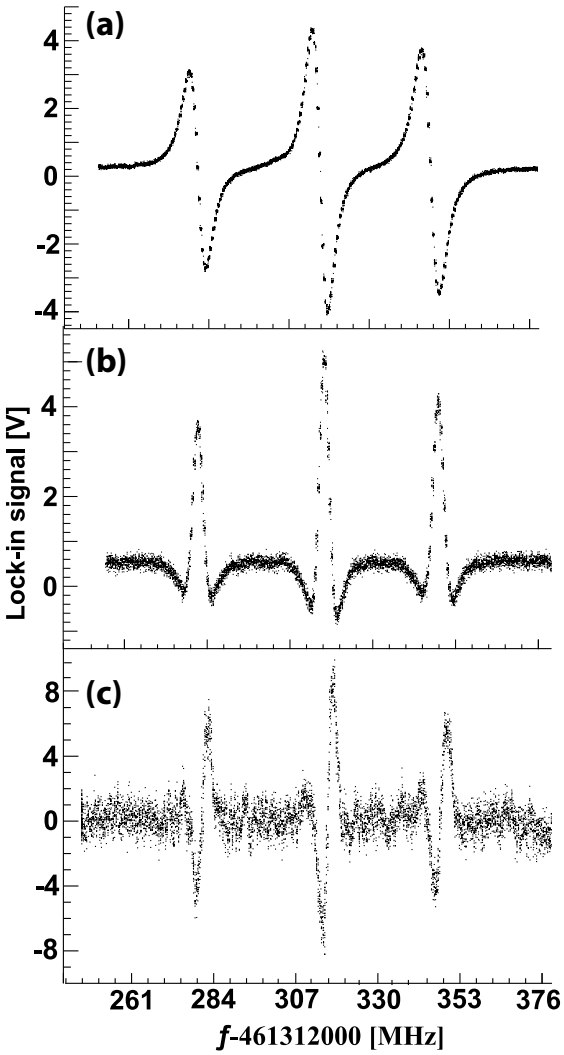

Figure 3.2.: (a) The first harmonic, (b) second harmonic and (c) the third harmonic of the modulation frequency of Lorentzian absorption signal from the output of lock-in amplifier(Scitech, 420 dual phase lock-in amplifier). They correspond to the 1^{st}, 2^{nd} and 3^{rd} derivative of the signal with respect to the frequency. The first and second harmonics signals have a modulation depth of 2.64 MHz and the third harmonic signal has a modulation depth of 3.3 MHz. The first harmonic of the absorption signal is used for spectroscopy and for laser stabilization.

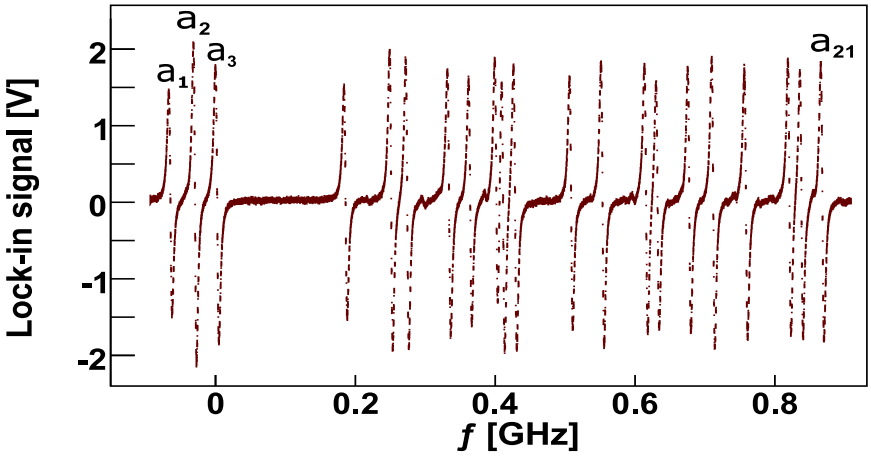

Figure 3.3.: Observed hyperfine spectrum of the R(25)(6-5) transition in molecular I_2. The nomenclature of the lines are indicated from a_1 to a_{21} . For experimental purpose where I_2 is used as a secondary standard, the zero crossing of line a_3 is used as reference for absolute frequency calibration.

pressure is calculated by the empirical formula [84],

$$\log(P) = \frac{-3512.830}{T} - 2.013 \cdot \log(T) + 18.37971, \tag{3.1}$$

where P is the iodine vapor pressure in Pascal and T is the cold finger temperature in Kelvin.

To determine the density of I_2 inside, the single pass absorption for different vapor pressures are measured which is shown in Fig. 3.4. The measured data agree very well with the empirical formula Eqn. 3.1, up to a temperature of approximately 30 °C. At this temperature the vapor pressure has reached approximately 82 Pa and all iodine in the cell is in the gas phase. We compare the measured points to the calculated value in order to find the pressure at higher temperatures and correct for it in the following measurements. In order to study the effect of pressure shift and pressure broadening the cold finger temperature is varied from

the least temperature we could attain, that is, 0.7 °C to 40 °C and the spectra is recorded.

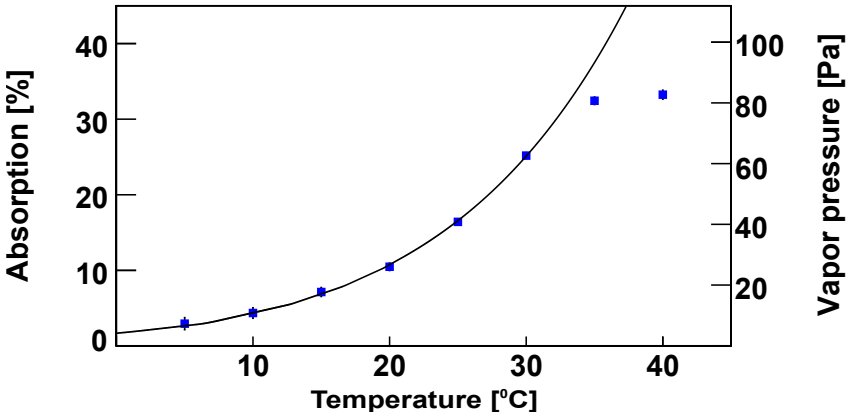

Figure 3.4.: Single pass absorption of resonant light passing through the iodine cell. This agrees well up to 30 °C with the calculated vapor pressure dependence as function of the cell's cold finger temperature. At higher temperature all iodine inside the cell is in vapor phase and hence density remains constant.

3.4. The fit function

The hyperfine transition lines a_1, a_2, a_3 are used for the analysis. A fit function is formulated with offset signal, the slope of the background, amplitude modulation, modulation depth, line center frequencies, Lorentzian width and amplitudes of the three lines as the fit parameters. These are the characteristics of the signal. Fig. 3.5 shows how the signal varies with different modulation depths. The fit function used for the analysis is given by,

$$S(f) = \int_0^{\frac{2\pi}{\omega_m}} \sum_i V(f + \delta sin(\omega_m t)) sin(n\omega_m t + \phi) dt \qquad (3.2)$$

where V is a Voigt profile [85], which is a convolution of a Gaussian and a Lorentzian profile describing the line shape, ω_m is the modulation frequency, δ is the modulation depth , n is the order of the derivative and ϕ is the phase. We see a clear indication of amplitude modulation up to 1% on the lines after fitting them to this function.

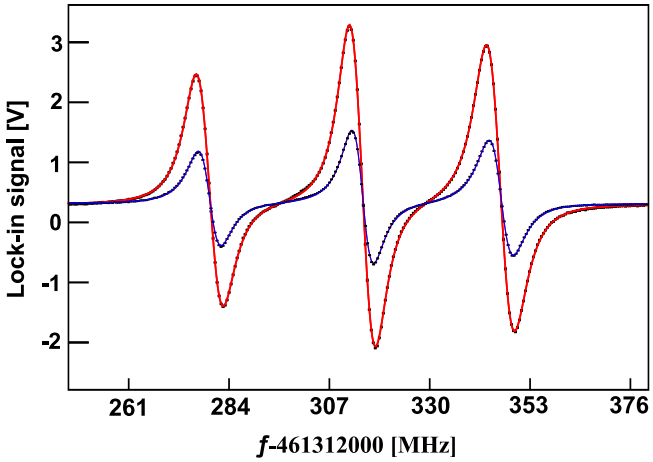

Figure 3.5.: The red line is a fit to the experimental data recorded with a modulation depth of 3.96 MHz and the blue line is a fit to the experimental data recorded with a modulation depth of 1.32 MHz. The integration time per point is 100 ms. The error bars represent rms values of the lock-in signal. The offset voltage of the lock-in detector is measured independently from off-resonant parts of the spectra.

3.5. Pressure shift and pressure broadening

Increasing the vapor pressure changes the center frequency and the line width of transitions because of the increase in collision rate of the molecules in the cell. The pressure shift of three hyperfine lines in molecular iodine as a function of vapor pressure is plotted in Fig. 3.6. By fitting a line, and extrapolating the data, the center frequency at zero vapor pressure could be determined for the three lines a_1, a_2 and a_3. We do not observe any

differences in the slopes of these three lines. The uncertainty is caused mainly due to the uncertainty in the vapor pressure in the iodine cell, which is approximately 1 Pa/K. From the slope of the fit, the shift in center frequency is determined to be about 10 kHz Pa^{-1}. The absolute line center frequencies extracted to an accuracy of 10^{-11} and pressure shift extrapolated to zero vapor pressure of the three components (a_1, a_2 and a_3) are tabulated in Table 3.1.

Table 3.1.: Center frequencies extrapolated to zero vapor pressure and pressure shift of a_1, a_2 and a_3 lines.

I_2 line	Center frequency(MHz)	Pressure shift(MHz/Pa)
a_1	461312279.9330(5)	−0.0105(3)
a_2	461312315.1104(5)	−0.0102(3)
a_3	461312346.9020(6)	−0.0101(1)

Hyperfine splitting between the lines is also determined which shows a consistent result, Fig. 3.7. A linear fit of the data points shows great linearity, proving that all three lines shift equally with change in vapor pressure. This makes molecular iodine a stable and reliable frequency standard. The hyperfine structure splitting is extracted in Table 3.2.

Table 3.2.: Hyperfine structure splitting of I_2 lines extrapolated to zero vapor pressure and the shift in the splitting with respect to change in vapor pressure.

Hyperfine Splitting	Frequency(MHz)	$\Delta f/\Delta$ P(MHz/Pa)
a_2 - a_1	35.1884(6)	1.980(2)
a_3 - a_1	66.9809(6)	2.622(2)
a_3 - a_2	31.7957(5)	1.358(2)

Similar to the center frequency, the line width of a transition also depends on the vapor pressure in the iodine cell. In Fig. 3.8, we see the relation between vapor pressure and the extracted Lorentzian width of the three hyperfine transitions in molecular iodine. Similarity in the

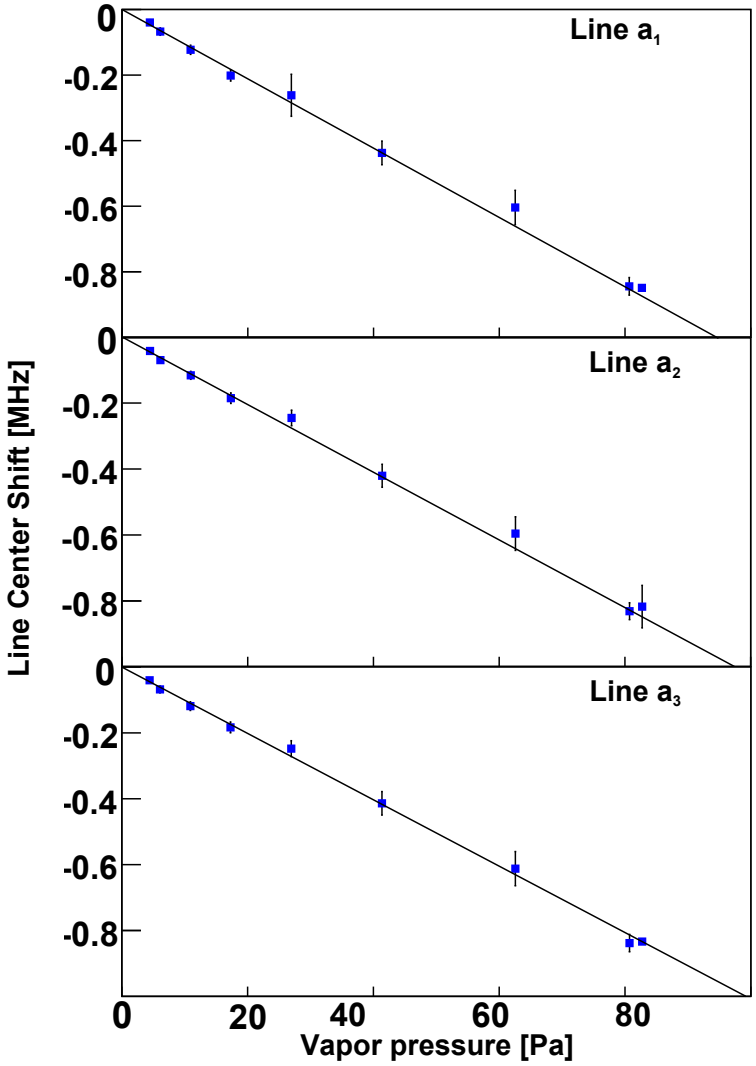

Figure 3.6.: Relative shifts of the center for the lines a_1, a_2 and a_3 as function of vapor pressure. The zero point of the frequency shift has been found by extrapolating to zero vapor pressure. We find for the center frequencies $fa_1(P) = fa_0(P) - 0.0105(3)\,\mathrm{MHz/Pa}$, $fa_2(P) = fa_0(P) - 0.0102(3)\,\mathrm{MHz/Pa}$ and $fa_3(P) = fa_0(P) - 0.0101(1)\,\mathrm{MHz/Pa}$, where fa_0 is the center frequency at zero vapor pressure .

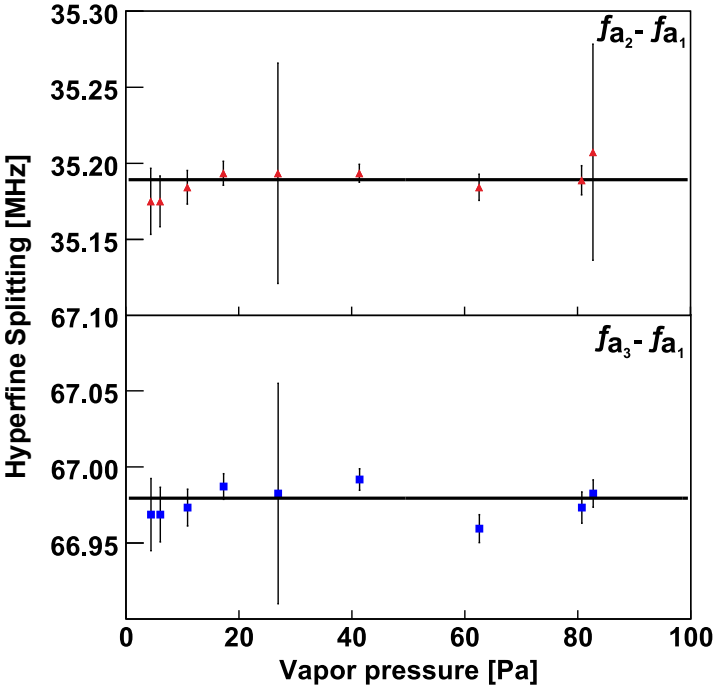

Figure 3.7.: Hyperfine splitting between lines a_2 and a_1 (red triangle data points) and between lines a_3 and a_1 (blue square data points) extrapolated to zero vapor pressure. A linear fit of the data points makes it evident the splitting shifts in a similar way with change in vapor pressure.

slopes of the fitted linear line indicates that all three lines broadens in the same way to about $60\,\mathrm{kHz\,Pa^{-1}}$. At high temperature it becomes difficult to estimate it accurately since the lines broadens in such a way that it perturbs the neighboring line and affects the fit procedure. The line widths and pressure broadening, extrapolated to zero vapor pressure are summarized for each components, a_1 , a_2 and a_3, in Table 3.3.

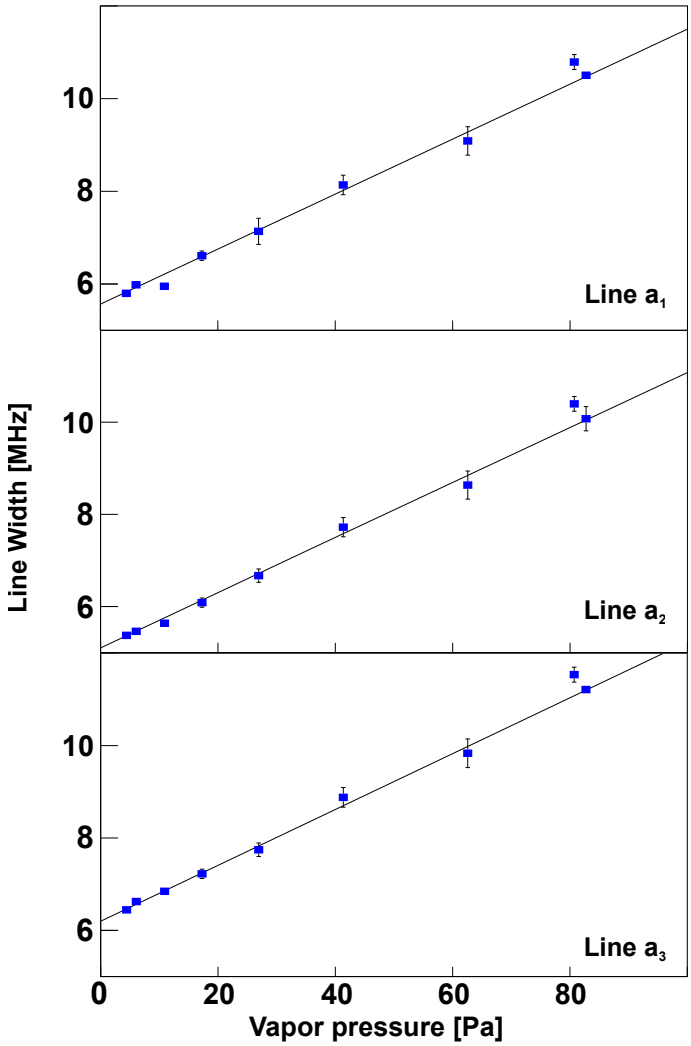

Figure 3.8.: Pressure broadening of the I_2 saturated absorption lines a_1, a_2 and a_3. The data points were extracted from data fitted with the line shape model (section 3.4). The linewidths extrapolated to zero vapor pressure, for a_1 is 5.564(3) MHz, for a_2 is 5.101(3) MHz and for a_3 is 6.198(3) MHz

.

Table 3.3.: Line widths and pressure broadening of a_1 , a_2 and a_3.

I_2 line	Line width(MHz)	Pressure broadening (MHz/Pa)
a_1	5.564(3)	0.059(9)
a_2	5.101(3)	0.060(6)
a_3	6.198(3)	0.060(7)

3.6. Clock comparison

Frequency modulated saturated absorption spectroscopy in I_2 was performed three months apart with two independent Rubidium(Rb) (FS 725) clocks as frequency reference. The parameters which affect the line shape of the signal such as modulation frequency, modulation depth, temperature of the cold finger were fixed to the same values for both the measurements. A shift of $27(5)\,\mathrm{kHz\,Pa^{-1}}$ in the line center with an accuracy of 5 x10^{-11} was observed due to change in the Rb clock (Fig. 3.9). It appeared that one of the Rb clock was broken. Although it was GPS time disciplined [86] it had a timing offset which disappeared after the repair. Such equipment failure is important to monitor constantly in order to be able to detect potential systematic offsets.

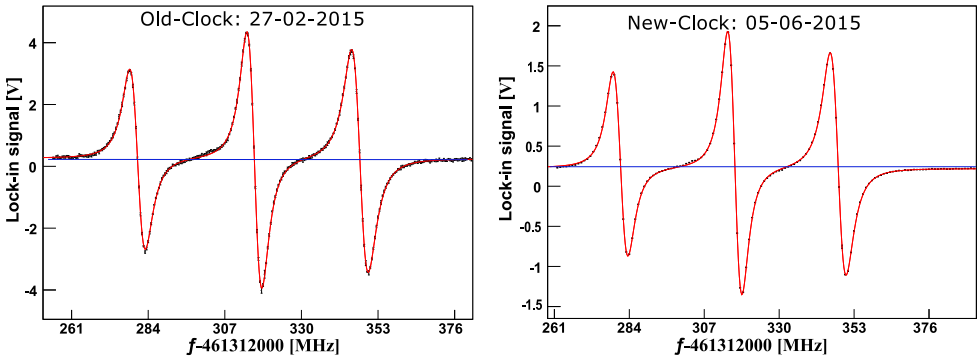

Figure 3.9.: The I_2 signal recorded with two independent Rubidium clocks three months apart. Both the measurements were carried out with a modulation depth of 400 mV, modulation frequency of 14.43 kHz, iodine cell temperature at 40 °C and cold finger temperature of the cell at 15 °C. The blue line indicates the residual electronic offset.

3.7. Section summary

Understanding the line shape is crucial in precision measurements to comprehend the effects of external parameters. The effects of the vapor pressure in the iodine cell on the line shape of transition lines in the spectrum have been investigated. A spectrum measured at low vapor pressures, i.e. below 10 Pa, provides the best signal-to-noise ratio for the determination of absolute frequencies due to minimized broadening and shift. The uncertainty in temperature of the cold finger gives the uncertainty in the vapor pressure which is about 1 Pa/K. The center frequencies of the lines in molecular iodine are shifted approximately by 10 kHz Pa^{-1}. The center frequency of the lines of about 6 MHz natural linewidth can be determined with an accuracy of 10^{-11} after correction of the pressure shift. In addition, the line width of the lines is increased by approximately 60 kHz Pa^{-1}. Measured results are consistent, as can be seen from the fact that the three hyperfine lines behave similarly. This means that molecular iodine is a reliable spectral reference. Also, we have a better defined lock point on narrow, single line which is well separated

from other I_2 lines. Another conclusion that can be taken from the fact that measured results are consistent, is that the fit function is valid over a large range of experimental parameters, including vapor pressure. Residual amplitude modulation up to 1% on the lines induces shifts of the zero crossing of the dispersive line shape. The results described in this section are indispensable for an unbiased analysis of the experimental spectroscopic data in the subsequent sections and a parity violation experiment. Without adequate data treatment a parity violation experiment will be hampered in its results.

4. Line Shape in Ba^+ Λ- System 6s-6p-5d[‡]

Comprehension of optical line shape is essential for applications based on high precision spectroscopy. A model based on optical Bloch equations (OBE) is implemented employing an optical frequency comb and transition frequencies in a single trapped $^{138}Ba^+$ ion stored in 'trap-1' are determined. This is an essential ingredient to determine Atomic Parity Violation in single Ba^+ [46, 47] and Ra^+ [36, 87] ion.

The sensitivity of the line shape due to various parameters are summarized and results are recapitulated following from the paper [81].

4.1. Optical line shape model

Transition between three of the lowest fine structure levels in Ba^+ form a Λ-configuration. When the two laser fields driving the transitions $6s\,^2S_{1/2}$ - $6p\,^2P_{1/2}$ (at wavelength λ_{494}) and $5d\,^2D_{3/2}$ - $6p\,^2P_{1/2}$ (at wavelength λ_{650}) are detuned by the same amount from their respective atomic resonances a coherent coupling between the $6s\,^2S_{1/2}$ and $5d\,^2D_{3/2}$ levels is observed, a phenomena known as Raman resonance. Under these conditions, a two-photon process reduces the population of the $6p\,^2P_{1/2}$ level [88]. The dynamics of the population of the $^2P_{1/2}$ level is described by OBE [89, 90, 91].

By solving the Liouville (optical Bloch) equation, which are the equations of motion for the elements of the density matrix, the Doppler- free spectrum of Ba^+ ion can be calculated for a three-level system as follows,

[‡]We summarize here the main contents of the paper where it distinguishes itself from the treatment in Chapter 5 of this thesis. The main contents of this chapter is also published under E. A. Dijck et al. [81], where also additional material is provided.

$$\frac{d}{dt}\rho_{ij} = \frac{i}{\hbar}[H, \rho] + R(\rho) \tag{4.1}$$

where H is the Hamiltonian describing the interaction of the ion with two laser fields and $R(\rho)$ is the damping matrix modeling relaxation and decoherence phenomena.

H contains the detunings Δ_1 and Δ_2 of the two laser frequencies and the corresponding Rabi frequencies Ω_1 and Ω_2 depending on the amplitude of the lasers E_1 and E_2.

$R(\rho)$ comprises of the spontaneous decay of the $6p\,^2P_{1/2}$ level and the decoherence effect due to finite laser linewidths. The matrix elements involve Γ_1 and Γ_2 which are the partial decay rates of the transitions $6p\,^2P_{1/2}$–$6s\,^2S_{1/2}$ and $6p\,^2P_{1/2}$–$5d\,^2D_{3/2}$ [92, 93] such that the total decay rate Γ=Γ_1+Γ_2 with associated decoherence rate $\gamma = \Gamma/2$ and γ_c which is the laser linewidth. These matrices together with the three- level scheme of Ba^+ is shown in Fig. 4.1.

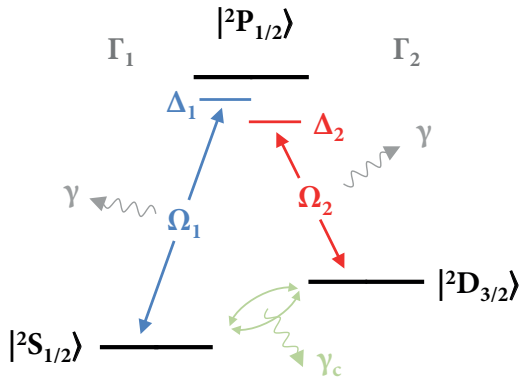

$$H = \hbar \begin{pmatrix} \Delta_1 & \Omega_1 & 0 \\ \Omega_1^* & 0 & \Omega_2 \\ 0 & \Omega_2^* & \Delta_2 \end{pmatrix}$$

$$R(\rho) = \begin{pmatrix} +\Gamma_1\rho_{22} & -\gamma\rho_{12} & -\gamma_c\rho_{13} \\ -\gamma\rho_{21} & -\Gamma\rho_{22} & -\gamma\rho_{23} \\ -\gamma_c\rho_{31} & -\gamma\rho_{32} & +\Gamma_2\rho_{22} \end{pmatrix}$$

Figure 4.1.: Low-lying energy levels of the Ba^+ ion. H is the Hamiltonian and $R(\rho)$ is the damping matrix in the Liouville equation. H includes the laser detunings Δ_1 and Δ_2 and the corresponding Rabi frequencies Ω_1 and Ω_2. $R(\rho)$ includes the relaxation rate Γ, decoherence rate γ and the laser linewidth γ_c.

4.2. Eight-level Bloch equation

The degeneracy of the magnetic sublevels is broken by applying a magnetic field of 170 µT. The atomic sub-levels of Ba^+ is then represented by Fig. 4.2.

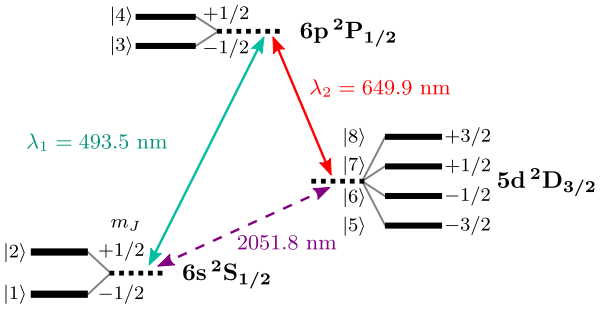

Figure 4.2.: The relevant energy levels along with their m_{ij} states and the transition wavelengths in $^{138}Ba^+$.

The Doppler- free spectrum of Ba^+ ion is then calculated by solving the Liouville equation for the eight-level system given by,

$$\frac{d}{dt}\rho_{ij} = \frac{i}{\hbar}\sum_k (H_{ik}\rho_{kj} - \rho_{ik}H_{kj}) + R_{ij}(\rho), \tag{4.2}$$

where the Hamiltonian H is given by 8×8 matrix as

$$H/\hbar = \begin{pmatrix}
\Delta_1 - \omega_B & 0 & -\frac{2}{\sqrt{3}}\Omega_1 & 0 & 0 & 0 & 0 & 0 \\
0 & \Delta_1 + \omega_B & 0 & \frac{2}{\sqrt{3}}\Omega_1 & 0 & 0 & 0 & 0 \\
-\frac{2}{\sqrt{3}}\Omega_1 & 0 & -\frac{1}{3}\omega_B & 0 & \frac{i}{\sqrt{2}}\Omega_2 & \frac{2}{\sqrt{6}}\Omega_2 & -\frac{i}{\sqrt{6}}\Omega_2 & 0 \\
0 & \frac{2}{\sqrt{3}}\Omega_1 & 0 & \frac{1}{3}\omega_B & 0 & \frac{i}{\sqrt{6}}\Omega_2 & \frac{2}{\sqrt{6}}\Omega_2 & -\frac{i}{\sqrt{2}}\Omega_2 \\
0 & 0 & -\frac{i}{\sqrt{2}}\Omega_2 & 0 & \Delta_2 - \frac{6}{5}\omega_B & 0 & 0 & 0 \\
0 & 0 & \frac{2}{\sqrt{6}}\Omega_2 & -\frac{i}{\sqrt{6}}\Omega_2 & 0 & \Delta_2 - \frac{2}{5}\omega_B & 0 & 0 \\
0 & 0 & \frac{i}{\sqrt{6}}\Omega_2 & \frac{2}{\sqrt{6}}\Omega_2 & 0 & 0 & \Delta_2 + \frac{2}{5}\omega_B & 0 \\
0 & 0 & 0 & \frac{i}{\sqrt{2}}\Omega_2 & 0 & 0 & 0 & \Delta_2 + \frac{6}{5}\omega_B
\end{pmatrix},$$

where $\omega_B = \mu_B|B|/\hbar$ is the Larmor frequency in a magnetic field $\vec{B}$. The corresponding Rabi frequencies are given by

$$\begin{aligned} \Omega_1 &= \frac{1}{2\hbar} E_1 \langle 6s\,^2S_{1/2}||er||6p\,^2P_{1/2}\rangle, \\ \Omega_2 &= \frac{1}{2\hbar} E_2 \langle 6p\,^2P_{1/2}||er||5d\,^2D_{3/2}\rangle. \end{aligned} \tag{4.3}$$

this is when the light at wavelength λ_{494} is linearly polarized, parallel to $\vec{B}_z$ and the light at wavelength λ_{650} is circularly polarized.

The detuning parameters Δ_1 and Δ_2 are,

$$\begin{aligned} \Delta_1 = \nu_1 - \nu_{(6s\,^2S_{1/2}-5d\,^2D_{3/2})} - \nu_{(5d\,^2D_{3/2}-6p\,^2P_{1/2})} \\ \Delta_2 = \nu_2 - \nu_{(5d\,^2D_{3/2}-6p\,^2P_{1/2})} \end{aligned} \tag{4.4}$$

where ν_1 and ν_2 are the laser frequencies (see Equations 2.6 and 2.7), $\nu_{(6s\,^2S_{1/2}-5d\,^2D_{3/2})}$, $\nu_{(5d\,^2D_{3/2}-6p\,^2P_{1/2})}$ and $\nu_{(5d\,^2D_{3/2}-6p\,^2P_{1/2})}$ are the Ba^+ transition frequencies.

The total 8×8 relaxation matrix R(ρ) is given by,

$$
\mathrm{R}=\begin{pmatrix}
\Gamma_1(\frac{1}{3}\rho_{33}+\frac{2}{3}\rho_{44}) & -\Gamma_1\frac{1}{3}\rho_{34} & -\gamma_{}^{'}\rho_{13} & -\gamma_{}^{'}\rho_{14} & -\gamma_l\rho_{15} & -\gamma_l\rho_{16} & -\gamma_l\rho_{17} & -\gamma_l\rho_{18} \\
-\Gamma_1\frac{1}{3}\rho_{43} & \Gamma_1(\frac{2}{3}\rho_{33}+\frac{1}{3}\rho_{44}) & -\gamma_{}^{'}\rho_{23} & -\gamma_{}^{'}\rho_{24} & -\gamma_l\rho_{25} & -\gamma_l\rho_{26} & -\gamma_l\rho_{27} & -\gamma_l\rho_{28} \\
-\gamma_{}^{'}\rho_{31} & -\gamma_{}^{'}\rho_{32} & -\Gamma\rho_{33} & -\Gamma\rho_{34} & -\gamma_{}^{'}\rho_{35} & -\gamma_{}^{'}\rho_{36} & -\gamma_{}^{'}\rho_{37} & -\gamma_{}^{'}\rho_{38} \\
-\gamma_{}^{'}\rho_{41} & -\gamma_{}^{'}\rho_{42} & -\Gamma\rho_{43} & -\Gamma\rho_{44} & -\gamma_{}^{'}\rho_{45} & -\gamma_{}^{'}\rho_{46} & -\gamma_{}^{'}\rho_{47} & -\gamma_{}^{'}\rho_{48} \\
-\gamma_l\rho_{51} & -\gamma_l\rho_{52} & -\gamma_{}^{'}\rho_{53} & -\gamma_{}^{'}\rho_{54} & -\Gamma_2\frac{1}{2}\rho_{33} & -\Gamma_2\frac{1}{2\sqrt{3}}\rho_{34} & 0 & 0 \\
-\gamma_l\rho_{61} & -\gamma_l\rho_{62} & -\gamma_{}^{'}\rho_{63} & -\gamma_{}^{'}\rho_{64} & -\Gamma_2\frac{1}{2\sqrt{3}}\rho_{43} & \Gamma_2(\frac{1}{3}\rho_{33}+\frac{1}{6}\rho_{44}) & \Gamma_2\frac{1}{3}\rho_{34} & 0 \\
-\gamma_l\rho_{71} & -\gamma_l\rho_{72} & -\gamma_{}^{'}\rho_{73} & -\gamma_{}^{'}\rho_{74} & 0 & \Gamma_2\frac{1}{3}\rho_{43} & \Gamma_2(\frac{1}{6}\rho_{33}+\frac{1}{3}\rho_{44}) & \Gamma_2\frac{1}{2\sqrt{3}}\rho_{34} \\
-\gamma_l\rho_{81} & -\gamma_l\rho_{82} & -\gamma_{}^{'}\rho_{83} & -\gamma_{}^{'}\rho_{84} & 0 & 0 & \Gamma_2\frac{1}{2\sqrt{3}}\rho_{43} & \Gamma_2\frac{1}{2}\rho_{44}
\end{pmatrix}
$$

where Γ_1= 14.7 MHz and Γ_2=5.4 MHz, The linewidths of the two lasers are both taken to be equal to γ_l and $\gamma^{'} = \gamma+\gamma_l$.

The OBE is solved numerically to determine the steady state solution for the density matrix ρ. The population in the $6p\,^2P_{1/2}$ state is represented by the sum of the matrix elements $(\rho_{33}+\rho_{44})$. This is proportional to the fluorescence rate at wavelength λ_{494} that is observed in the experiment.

4.3. Experimental determination and frequency stabilization

The schematics of the trap setup (trap 1) and the optical detection method used for the measurement is shown in Fig. 4.3. Both light fields are taken to propagate along the $-y$ direction and the magnetic field $\vec{B}$ defines the z direction.

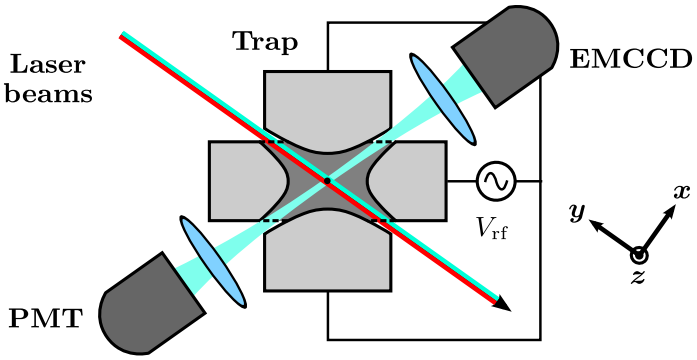

Figure 4.3.: Schematics of the Paul trap used for trapping $^{138}Ba^+$ ions. The inner diameter of the ring is 5 mm. Optical detection of the florescence from the ions are done by a PMT and an EMCCD camera. Both light fields propagate along the -y direction.

The scheme to transfer the $\Delta\nu/\nu = 10^{-11}$ frequency stability of the frequency comb to light at wavelengths λ_{494} and λ_{650} are shown in Fig 4.4. The important parameters required for a measurement is tabulated in

Table 4.1. The settings relevant to the laser frequencies are tabulated in Table 4.2.

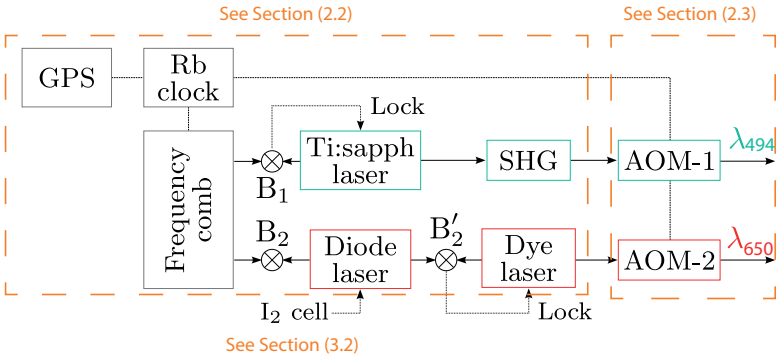

Figure 4.4.: Scheme to transfer the $\Delta\nu/\nu = 10^{-11}$ frequency stability of the frequency comb to light at wavelengths λ_{494} and λ_{650}. The implementation of the different laser light sources, frequency stabilization, timing and detuning controls of the laser lights are explained in the respective sections as indicated.

Table 4.1.: Important parameters for the experimental determination. w_0 is the beam waist.

Parameters	Value
w_0	60 µm
ν_s	53.6 kHz
t_c	0.80
t_s	0.20

Table 4.2.: Intermediate frequencies to determine the laser frequencies in the trap (see also Fig 2.17) according to Eqns. 2.6 and 2.7. During measurements the repetition rate of the comb $\nu_{comb,rep}$ has been varied in order to change ν_1.

Frequency	Value
$\nu_{\mathrm{comb,rep}}$	250 000 233.5 Hz
$\nu_{\mathrm{comb,offset}}$	−40 000 000.0 Hz
For light at wavelength λ_{494}:	
m_1 (mode number)	1214851
ν_{B_1}	29.01(1) MHz
$\nu_{\mathrm{AOM\text{-}1}}$	198.90 MHz
For light at wavelength λ_{650}:	
m_2 (mode number)	1845248
ν_{B_2}	−27.33(1) MHz
$\nu_{\mathrm{B}_2'}$	−[1116.8(1)–1274.2(1)] MHz
$\nu_{\mathrm{AOM\text{-}2}}$ (double pass)	348.00 MHz

4.4. Results for transition frequencies in $^{138}Ba^+$

Spectra are recorded for different magnetic field settings, laser intensities, and laser polarization by scanning across the $5d\,^2D_{3/2}$–$6p\,^2P_{1/2}$ resonance. The line shape calculated numerically by solving the eight-level optical Bloch equations is fitted to each individual spectrum. The atomic transition frequencies are determined by estimating and confirming the parameters of the Bloch equations describing the system. This is required, because these parameters cannot be found in a fitting procedure.

4.4.1. Line shape as a function of detuning

In Fig 4.5 spectra recorded with constant laser intensities and different detunings Δ_1 varied in steps of 12 MHz are displayed. The red solid lines correspond to the fitting of OBE to the data. We observe here a substantial change in the shape of the resonances. Nevertheless they are described well by OBE fits.

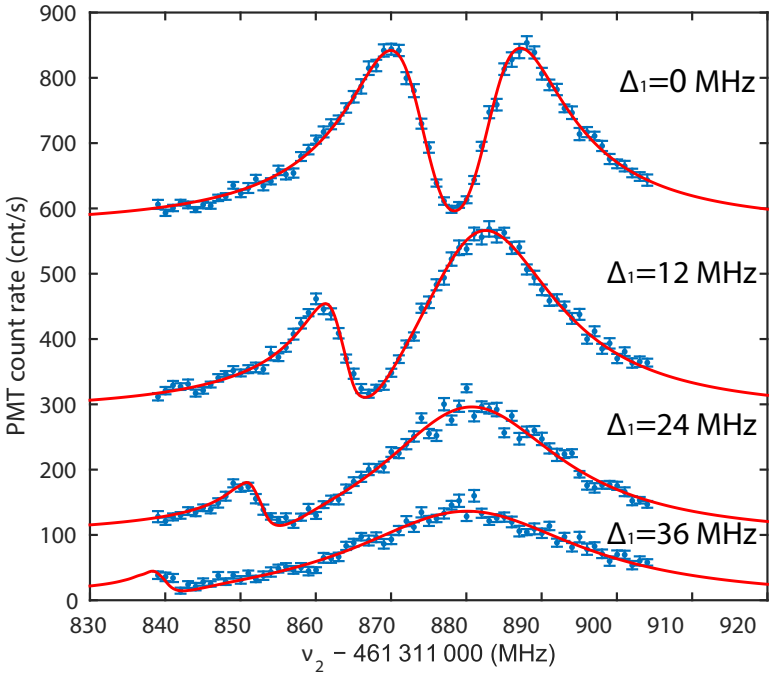

Figure 4.5.: Spectra of the $5d\,^2D_{3/2}$–$6p\,^2P_{1/2}$ transition in a single Ba^+ ion recorded for different detunings Δ_1 varied in steps of 12 MHz. Note that the baselines are shifted to show the spectra. The intensities of the light fields are kept constant. Solid lines correspond to the result of fitting the OBE to the data.

4.4.2. Line shape as a function of intensity

In Fig 4.6 a set of four spectra recorded with different intensities of the light at wavelength λ_{650}, corresponding to different Rabi frequencies Ω_2 is given. The intensity ranged from 0.3 to 4 times the saturation intensity of the $5d\,^2D_{3/2}$–$6p\,^2P_{1/2}$ transition. The frequency ν_1 is kept constant during these measurements. The prominent feature in the spectra is a dip in the fluorescence caused by the two-photon process at Δ_1=Δ_2 appearing at $\Delta_1 \simeq \Delta_2 \simeq 0$ MHz . The polarizations of the two laser fields

determine which coherences cause a fluorescence dip. For the measurements presented here the dominant contributions are from coherences $|1\rangle\langle 5|$ and $|2\rangle\langle 8|$ (see Fig 4.2). In this case, the magnetic field magnitude is too small to resolve the two individual components here.

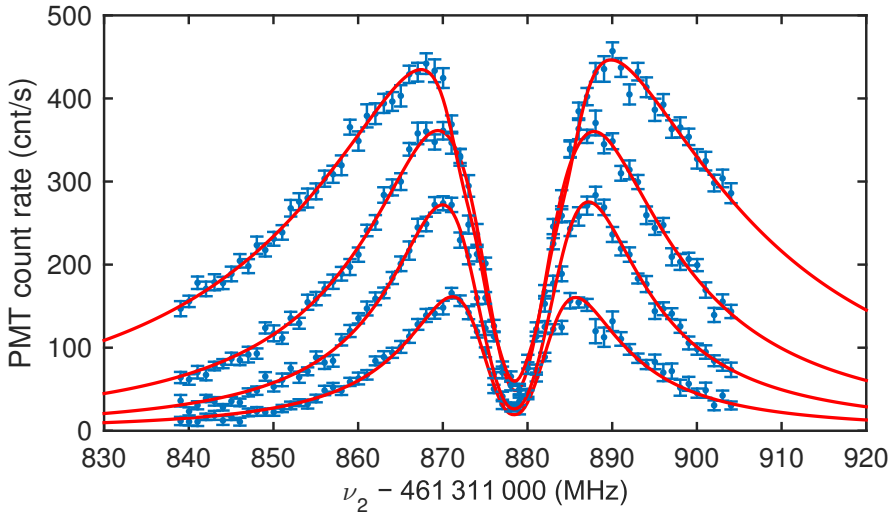

Figure 4.6.: Spectra of the $5d\,^2D_{3/2}$–$6p\,^2P_{1/2}$ transition in a single Ba^+ ion recorded for different light frequencies Ω_2, ranging from 0.3 to 4 times the saturation intensity. Frequency ν_1 is kept constant with $\Delta_1 \approx 0$. Solid lines correspond to the result of fitting the OBE to the data. The width of the spectra shows power broadening.

4.4.3. Line shape as a function of polarization

An example of spectrum is displayed in Fig. 4.7 where both the light at wavelength λ_{494} and λ_{650} is about 85% linearly polarized under an angle of 75° to a magnetic field of 600 µT. In this more complex polarization state, multiple dips in the fluorescence appear. The outermost features are due to coherences $|1\rangle\langle 8|$ and $|2\rangle\langle 5|$. The frequency difference between these outer dips can be employed as a calibration of the magnetic field strength (ω_B).

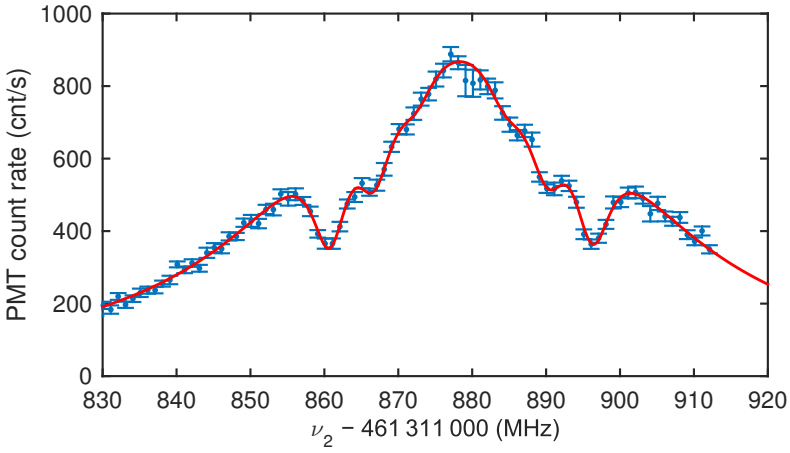

Figure 4.7.: Spectra of the $5d\,^2D_{3/2}$–$6p\,^2P_{1/2}$ transition in a single Ba^+ ion. Both light fields are linearly polarised at an angle of 75 ° to the magnetic field direction, with about 15 % admixture of circularly polarised light. The solid line corresponds to the fit of the adjusted OBE, taking into account the polarisation of the laser light. Detuning $\Delta_1 \approx 0$ results in the symmetric line shape.

4.4.4. Transition frequencies

The atomic transition frequency is determined by extrapolating the fitted value to zero laser intensity (see Fig 4.8). Intensity-dependent light shift effects are included in the OBE and will drop out in the fitting procedure. However, a small mismatch in polarization or magnetic field orientation between model and experiment can modify a transition amplitude component resulting in a mismatch in the light shift.

The weighted average of the $5d\,^2D_{3/2}$–$6p\,^2P_{1/2}$ and $6s\,^2S_{1/2}$–$5d\,^2D_{3/2}$ transition frequencies as well as their sum, the $6s\,^2S_{1/2}$–$6p\,^2P_{1/2}$ transition frequency in $^{138}Ba^+$, are given in Table 4.3. The results presented here are limited by statistics and the stability of the laser system.

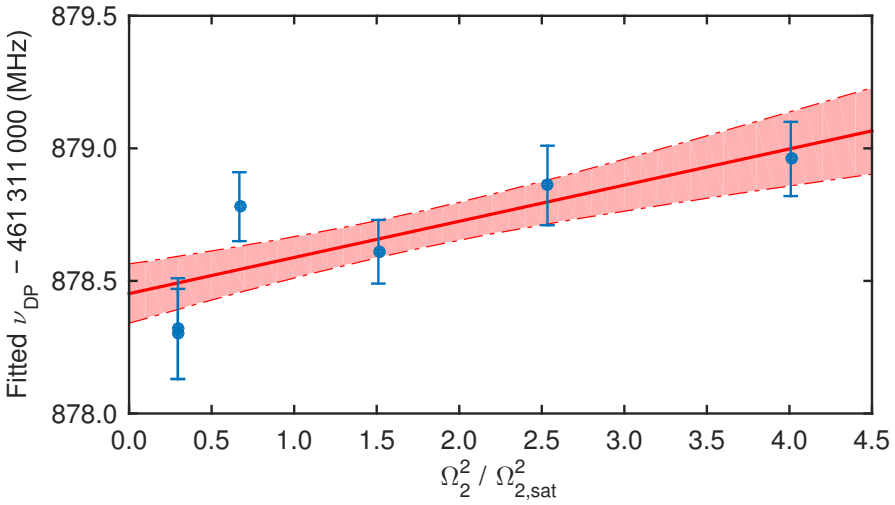

Figure 4.8.: Extracted transition frequency $\nu_{(5d\,^2D_{3/2}-6p\,^2P_{1/2})}$ as function of laser intensity Ω_2^2 (given in terms of saturation intensity $\Omega_{2,sat}^2$) for $\Delta_1 \approx 0$. The data shown include those from the spectra in Fig. 4.6. An intensity-dependent shift can be seen, which is attributed to a small mismatch between model and experiment in magnetic field direction. The solid line corresponds to a linear extrapolation to zero laser light intensity, with 1σ confidence bounds indicated.

Table 4.3.: Transition Frequencies of the $5d\,^2D_{3/2}$–$6p\,^2P_{1/2}$ and $6s\,^2S_{1/2}$–$5d\,^2D_{3/2}$ transitions in Ba^+. Their sum yields the frequency of the $6s\,^2S_{1/2}$–$6p\,^2P_{1/2}$ transition.

Transition	Frequency (MHz)	Relative uncertainty
$\nu_{(5d\,^2D_{3/2}-6p\,^2P_{1/2})}$	461 311 878.5(1)	2×10^{-10}
$\nu_{(6s\,^2S_{1/2}-5d\,^2D_{3/2})}$	146 114 384.0(1)	6×10^{-10}
$\nu_{(6s\,^2S_{1/2}-6p\,^2P_{1/2})}$	607 426 262.5(2)	3×10^{-10}

4.5. Section summary

The optical line shape is described by an eight-level optical Bloch model. Spectra have been recorded by trapping a single $^{138}Ba^+$ ion and varying parameters such as laser polarization with respect to the magnetic field, intensities and detunings of the laser fields. These are in excellent agreement with the OBE. The atomic transition frequencies of $6s\,^2S_{1/2}$ – $6p\,^2P_{1/2}$, $5d\,^2D_{3/2}$ – $6p\,^2P_{1/2}$, and $6s\,^2S_{1/2}$ – $5d\,^2D_{3/2}$ transitions in $^{138}Ba^+$ have been determined to sub-MHz precision by selecting the suitable parameters. This work provides an improvement of 3 orders of magnitude over previous measurements that had obtained these transition frequencies between low-lying levels to order 100 kHz accuracy using Fourier transform spectroscopy in large ion samples [94, 95].

This was possible due to the laser cooling of the ion, the technical implementation of scanning over the full resonance without significant effects from heating of the ion sample and the full description of the line shape in the frame work of the optical Bloch equations.

5. Transition Frequencies in $^{134}Ba^{+}$ and $^{136}Ba^{+}$

Measurement of isotope shifts (IS) for different transitions provide probe for the atomic wave functions at the position of the nucleus. Extracting the transition frequencies for $5d\,^2D_{3/2} - 6p\,^2P_{1/2}$, $6s\,^2S_{1/2} - 5d\,^2D_{3/2}$ and $6s\,^2S_{1/2} - 6p\,^2P_{1/2}$ transitions in different isotopes of Ba^{+} enable us to determine the isotope shifts for these transitions with unprecedented accuracy. Transition frequencies extracted from measurements on a single trapped $^{138}Ba^{+}$ ion were presented in Chapter 4. Here we extend this study to the isotopes $^{134}Ba^{+}$ and $^{136}Ba^{+}$ ions stored in the modified trap described in Chapter 2. We explore the dependence of line shape in particular to the detuning, intensities, polarization of the laser lights and number of ions with a model based on quantum interference.

The spectral response is dependent on the way of excitation of the system. We describe the spectral line shape in the steady state limit which means that the interaction time of the atomic system with laser fields of constant intensities and frequency is much longer than any coherence time in this system. In the previous chapter (Chapter 4) the experimentally observed spectra are analyzed by comparing experimental spectra to numerical solution of the Optical Bloch Equation (OBE). These had to be generated for every change in the parameters. The OBE, based on the rotating wave approximation, is capable of describing the time evolution of the system, which is not studied here. The observable in the experiments discussed in this thesis is proportional to the steady state solution. It can be shown that for a 3-level Lambda system under certain conditions the steady state solution of the OBE is equivalent to a Fano profile [96]. Fano profiles describe the interference between two pathways to a common final state. The linewidth of the first transition pathway is typically assumed to be much larger than the second transition. In that

limit, the transition amplitude of the first can be considered as constant over the resonance width of the second transitions. The characteristic shape arises from the phase shift between the two contributions leading to constructive or destructive interferences. This result in spectra observed in a wide variety of physical systems such as solid state physics, particle physics, e.g. the $\eta - \rho$ resonance and atomic physics. The phase shift of the two interfering amplitudes becomes a parameter with physical meaning. An approach by putting the emphasis on the interpretation of the physical phenomena has been employed in the discussion of dark resonances in the Ba^{+} ion system [89].

The light - ion interactions are used to discern the influence of the various parameters by recording individual spectrum for different experimental conditions. The experimental procedure and control on experimental parameters are investigated further to understand the influence of these to the obtained line shape. The line shape depends on experimental parameters. These can be extracted through a line shape description with a Fano profile, i.e. the ion can be employed as a detector of such experimental parameters.

5.1. Light shift in Λ-system

The light shift (Section 1.3.3) enables the test of atomic theory and improves the understanding of atomic structure which are essential for an atomic parity violation experiment. The calculation approach of the optical Bloch equations employs unperturbed energy levels and Rabi frequencies which are not "a priori" known (Fig. 5.1(a)) in order to calculate the spectral line shape. The Fano-profile results from the interference between two paths $^{2}S_{1/2}$ - $^{2}P_{1/2}$ and $^{2}D_{3/2}$ - $^{2}P_{1/2}$ to the final state $^{2}P_{1/2}$ on the basis of the light shifted energy levels (dressed states) as shown in Fig. 5.1(b).

In a three level system, forming a Λ-configuration (see Fig. 5.1(a)) the two transitions $^{2}S_{1/2}$ - $^{2}P_{1/2}$ and $^{2}D_{3/2}$ - $^{2}P_{1/2}$ are driven by two lasers with frequencies ω_{494} and ω_{650}, respectively to the atomic frequencies

$$\omega_{SP} = (E_P - E_S)/\hbar \tag{5.1}$$

$$\omega_{DP} = (E_P - E_D)/\hbar \tag{5.2}$$

and

$$\omega_{SD} = (E_D - E_S)/\hbar \tag{5.3}$$

respectively with the detunings between the laser frequencies and atomic frequencies given as

$$\begin{aligned} \delta_1 &= \omega_{494} - \omega_{SP} \\ \delta_2 &= \omega_{650} - \omega_{DP}. \end{aligned} \tag{5.4}$$

The stimulated Raman resonance condition between unperturbed energy levels leading to coherent population trapping when $\delta_1 = \delta_2$ is then given as

$$\hbar\omega_{494} - \hbar\omega_{650} = E_D - E_S. \tag{5.5}$$

This is only valid in the limit of very low intensities such that light shifts do not play a role. Intensity-dependent light shifts occur at finite intensities of light at wavelengths λ_{494} and λ_{649} driving the transitions $6s\,^2S_{1/2} - 6p\,^2P_{1/2}$ and $5d\,^2D_{3/2} - 6p\,^2P_{1/2}$, respectively (see Fig. 5.1(b)). A shift of energy level $\Delta E_{L.S(B)}$ is caused due to laser light at wavelength λ_{494} and an energy level shift of $\Delta E_{L.S(R)}$ is caused due to laser light at wavelength λ_{649}. This light shift is also dependent on the detunings δ_1 and δ_2. Then the stimulated Raman resonance condition becomes

$$\hbar\omega_{494} - \hbar\omega_{650} = E_D + \hbar\delta_{LS} - E_S, \tag{5.6}$$

where δ_{LS} is the shift in frequency due to light shift caused by the laser fields. The light shift of level $^2P_{1/2}$ is opposite to that of level $^2D_{3/2}$ [96]. The approach with OBE takes the intensities and detuning depended shifts into account but requires the knowledge of all parameters such as intensities and detunings.

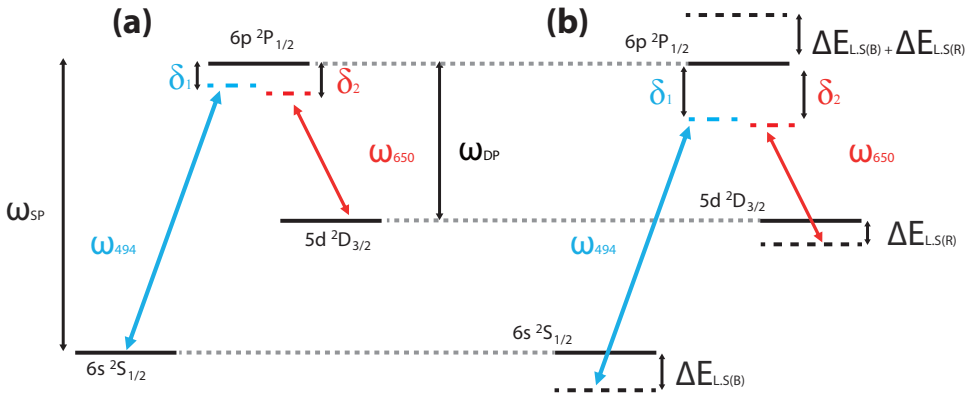

Figure 5.1.: (a) Three level Λ-configuration ($^2P_{1/2}$, $^2S_{1/2}$, $^2D_{3/2}$) driven by two laser fields at frequencies ω_{494} and ω_{650}. δ_1 and δ_2 are the two detunings and light shifts are negligibly small. (b) Light shifted energy levels due to the presence of high intensity laser fields. $\Delta E_{L.S(B)}$ is the change in energy of the atomic state caused by laser at wavelength λ_{494} and $\Delta E_{L.S(R)}$ is the change in energy of the atomic state caused by laser at wavelength λ_{649}. The light shift depends both on the detunings and the intensity of the laser light.

5.2. Fano Profile

Fano profiles have a wide range of applications in nuclear, atomic, and solid-state physics [97, 98, 99, 100, 101, 102, 103, 104, 105, 106]. They result in systems where interfering pathways lead to a common final state which is observed in the experiment. As a result the shape of the spectrum exhibits more features than just the sum of two Lorentzian line shapes. We analyze the Ba^{+} system where we want to calculate the spontaneous emission rate from the 6p $^2P_{1/2}$ state (dashed line in Fig. 5.1). The interfering pathways to the 6p $^2P_{1/2}$ state are excitation of the S-P transition by one photon from the laser field at frequency ω_{494} and the three step process via a virtual intermediate state. The lineshape can be written as an interference pattern of two detuning dependent complex

transition amplitudes a_1 and a_2, with

$$a_j = \frac{\sqrt{N_j/\Gamma_j}}{1 + i\,(\nu - \nu_j)/\Gamma_j} = \sqrt{N_j/\Gamma_j}\frac{1 + i(\nu - \nu_j)/\Gamma_j)}{1 + ((\nu - \nu_j)/\Gamma_j)^2}, \tag{5.7}$$

where j is a label for the transition, N_j the normalization, Γ_j the linewidth and ν_j the resonance frequency for transition j. The detuning can be then written as,

$$\delta_j = \nu - \nu_j. \tag{5.8}$$

The resultant transition amplitude is the sum of the individual amplitudes, where an additional free parameter ϕ accounts for a relative phase between a_1 and a_2.

$$a_{tot} = a_1 + a_2\, exp(-i\phi); \tag{5.9}$$

Multiplying the amplitude with its complex conjugate yields an analytical form for the spectrum S_{int} as a result of the interference. The spectral line shape S_{int} becomes

$$S_{int} = a_{int} \cdot a^*_{int} = |a_1|^2 + |a_2|^2 + a_1 a_2^*\, exp(i\phi) + a_1^* a_2\, exp(-i\phi), \tag{5.10}$$

where the first two parts represent the spectrum in case of no interference between the two contributions and the last part is the interference contribution. (Note: the sum of a complex number and its complex conjugate is real). The interference term is explicitly given by

$$\begin{aligned} A_{int} = 2\{&(\Re(a_1)\Re(a_2) + \Im_\mu(a_1)\Im_\mu(a_2))cos(\phi) \\ &+ (\Re(a_2)\Im(a_1) - \Re(a_1)\Im(a_2))\sin(\phi)\}. \end{aligned} \tag{5.11}$$

.

The spectral shape exhibits a strong deviation from the sum of two Lorentzian contributions. The interference term dominates the spectrum and its particular shape strongly depends on the value of the phase ϕ (Fig. 5.2). We observe constructive interference for $\phi = 0$ and destructive interference for $\phi = -\pi$. The parameter $\epsilon = -cot(\phi)$ is called the Fano factor in the classical description by Fano [107].

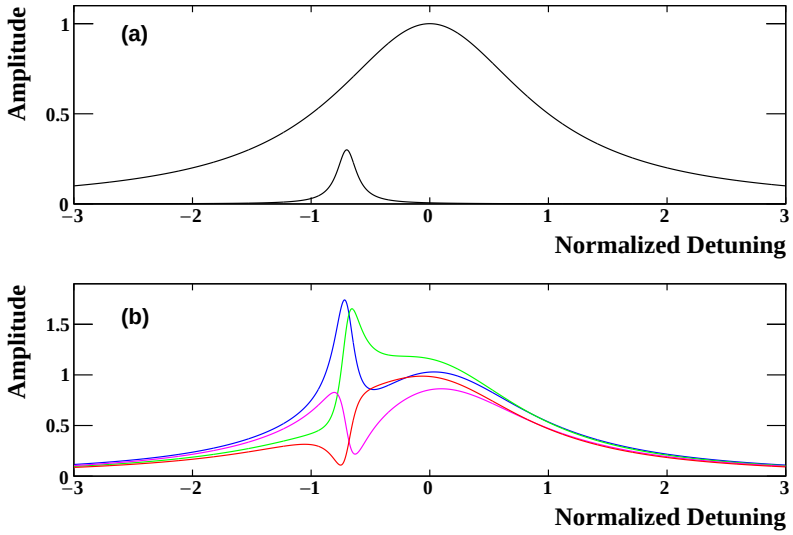

Figure 5.2.: (a): The spectral lineshape for the two individual resonances. The wider one is centered at 0 and has a width of 1, while the narrow line is centered at -0.7 with a width of 0.1. (b): The resultant spectral lineshape due to the interference for different phase shifts. Note: Neither the minima nor the maxima of the interference line shape appears at the location of the center (-0.7) of the narrow transition.

.

The fit function of the Fano profile is given by

$$\begin{aligned} F(\nu) =& S_{int}(a_1, a_2, \phi) + bkg \\ =& S_{int}(a_1(\delta_1, \Gamma_1, N_1), a_2(\delta_2, \Gamma_2, N_2), \phi) + bkg, \end{aligned} \tag{5.12}$$

where a_1 and a_2 are the complex transition amplitudes. This form is easily written in a closed form in programming languages like C++ which include complex algebra. The explicit form in real algebra will require many more terms and results in a less stable fitting function.

The Fano profile is equivalent to steady state solution of the OBE under the conditions that the two laser lights at wavelengths λ_{494} and λ_{649} driving the respective transitions have intensities such that the atomic

transitions are not saturated. There are advantages of the description of the line shape as a Fano profile rather than the solution of the OBE. The Fano-profile can be written in analytically closed function which is better suited for a χ^2 - fitting (Eqn. 5.10). We verify the equivalence of the Fano - profile and the steady state solutions of the eight level optical Bloch equations by fitting the analytic function (Eqn. 5.10) to 8-level OBE simulations (see Fig. 5.3). Here we have chosen the parameters for the polarization of the laser light and the direction of the magnetic field to be the same as in the measurements. The polarization of light at λ_{494} is linear and parallel to the magnetic field direction $\vec{B_z}$. Light at wavelength λ_{649} is elliptically polarized. In particular we have studied the parameters for the extraction of the transition frequencies and the light shifts of the relevant energy levels.

We verified the validity of Eqn. 5.10 by comparison with a number of parameters such as detuning (Fig. 5.4) and intensities (Fig. 5.5 and Fig. 5.6) which had been employed in the experiment. The analysis of the line shape (Eqn. 5.10) in terms of the intensities I_{494} of the light at wavelength λ_{494} and the intensity I_{649} of the light at wavelength λ_{649} shows excellent agreement of the two methods for extracting the spectral line shape. An example of such a test is demonstrated in Fig. 5.3 where for fixed intensities of light at wavelength λ_{494} and λ_{649} the detuning δ_1 is varied from -15 MHz to +14 MHz. The results comprise of the change in (i) the frequency at the Raman condition if the light shift is also taken into account together with the detuning from the unperturbed energy level at resonance given as $\delta_1 - \delta_2 + \delta_{LS} = 0$ (ii) the width of the Raman feature (iii) the frequency of the transition of the unperturbed S-P level (iv) the width of the S-P transition and (v) the phase between S-P and D-P transitions with respect to changes in the intensities I_{494} and I_{649} of the light at wavelengths λ_{494} and λ_{649}, respectively. The light shift in these transitions can be extracted with the Fano line shape model.

The agreement between OBE and Fano profile is on a level of 30 kHz which is much better than the achieved statistical accuracy. This gives us confidence to use the Fano profile model for the extraction of transition frequencies in the Ba^{+} system with a high accuracy.

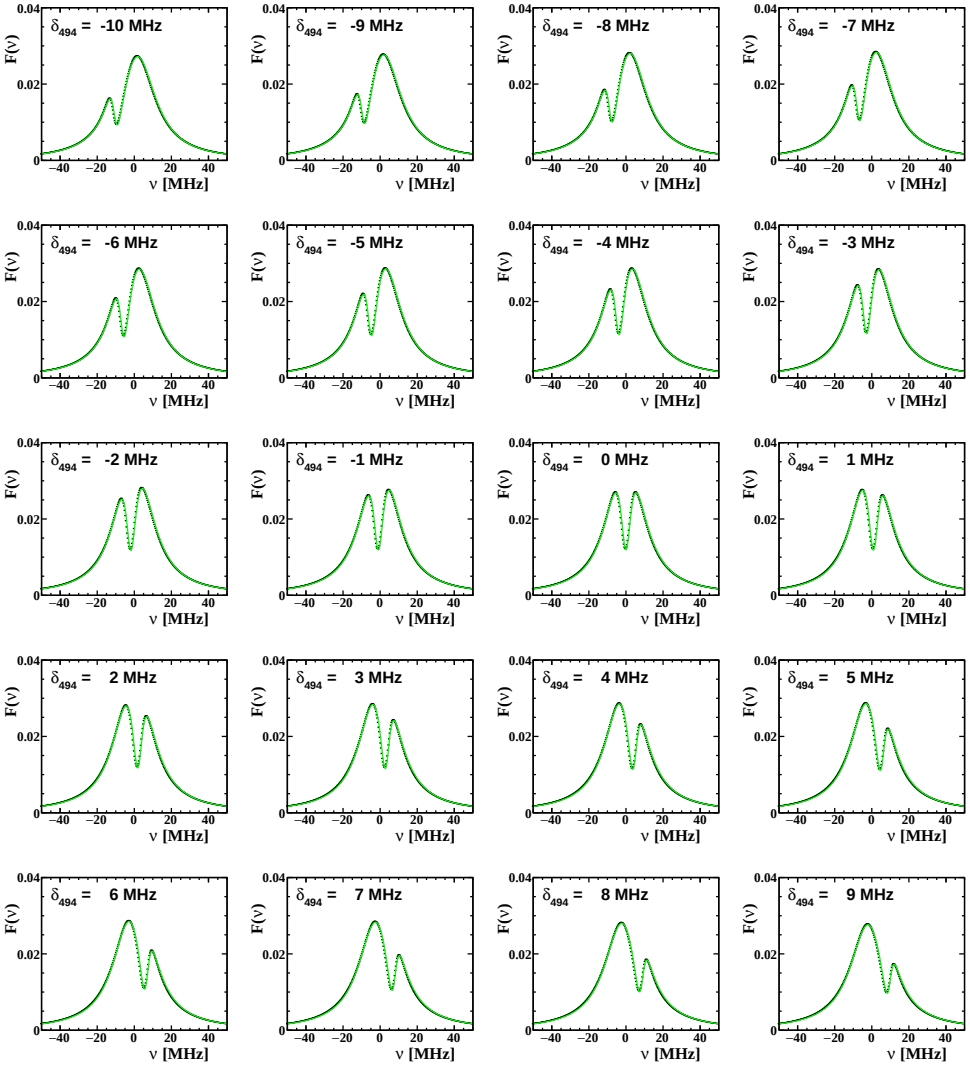

Figure 5.3.: Fano profile fit to the calculated steady state solution of the OBE for a 3-level lambda system at different laser detunings δ_1 of light at wavelength λ_{494} with constant intensity I_{494} and I_{649} for light at wavelengths λ_{494} and λ_{649}, respectively. Detuning δ_{494} is changed in the OBE calculations in steps of 1 MHz while other parameters are kept constant.

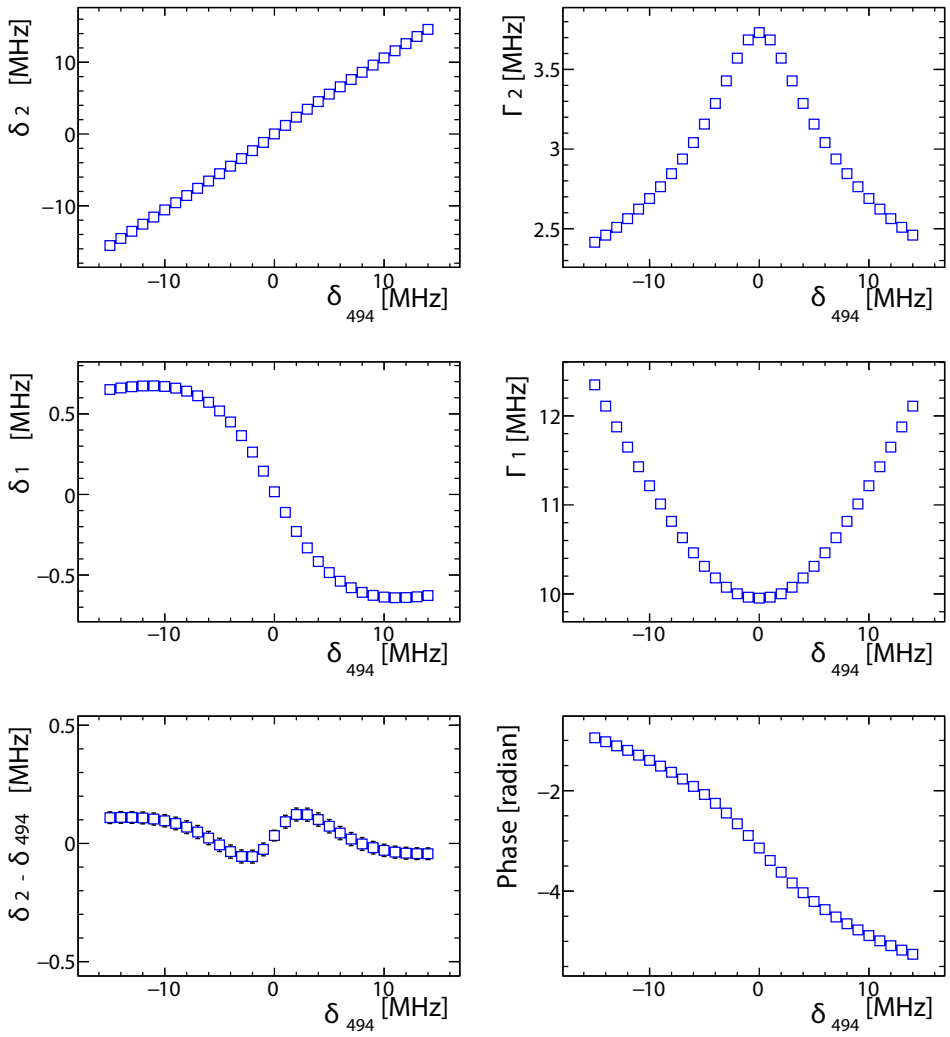

Figure 5.4.: Results from the Fano profile fit for light at different detunings δ_{494}. The calculated data has wider range than the data range from the experiments. The uncertainty on the extracted fitting parameters are below the size of the symbols.

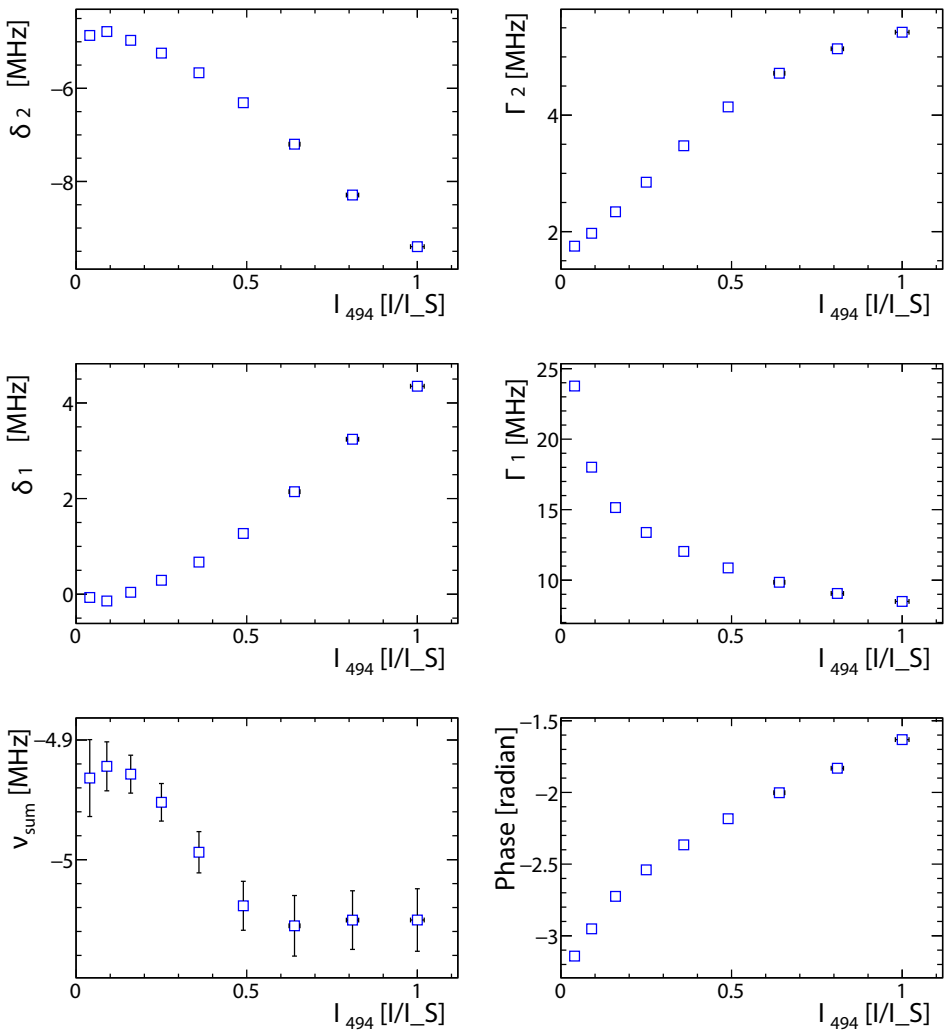

Figure 5.5.: Results obtained after fitting a Fano-profile to the calculated steady state solution of the Optical Bloch Equation at different intensity I_{494} for light at wavelength λ_{494} and at a constant detuning δ_{494}. The frequencies. The width of the Raman resonance increases with increase in intensity I_{494} when the width of D-P transition decreases at higher intensities I_{494}. Shift in the phase as a function of intensity I_{494} explains the origin of the asymmetric line shape of the Fano profile.

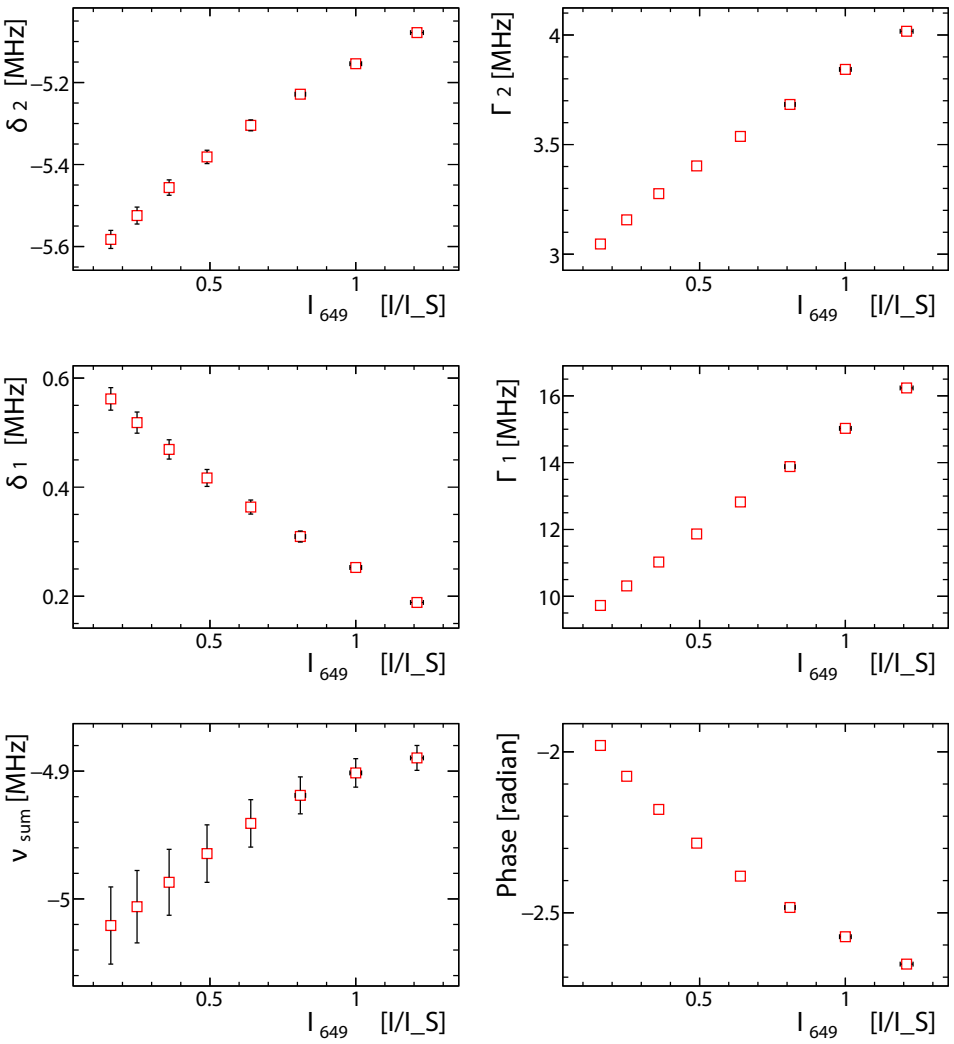

Figure 5.6.: Results obtained after fitting a Fano-profile to the calculated steady state solution of the Optical Bloch Equation at different intensity I_{649} for light at wavelength λ_{649} and at a constant detuning δ_{494} and constant intensity I_{494} for light at wavelength λ_{494}. The width Γ_1 increases with respect to increase in intensity I_{649} of light at wavelength λ_{649} due to power broadening.

5.3. Experimental procedure and conditions

The apparatus, laser light sources, stabilization of power and frequencies used for the measurements are discussed in Chapter 2. Here we describe the experimental steps which have been taken to record a resonance spectrum. One of the two ovens is operated to produced Ba atoms of the two isotopes $^{134}Ba^{+}$ and $^{136}Ba^{+}$. When switching to the other isotope the trap is emptied. Suitable voltages are applied to the end cap electrodes and the auxiliary electrodes in order to minimize the micro motion by compensating for the stray electric fields developed inside the trap.

The line shape of the Λ-System is recorded as a function of the $5d\,^2D_{3/2}$ – $6p\,^2P_{1/2}$ transition at various experimental parameters for the detuning from $6s\,^2S_{1/2} - 6p\,^2P_{1/2}$ transition and intensities at the two transition frequencies. The determination of the absolute laser light frequencies and the sensitivity of the line shape to the method of recording the spectra and to different experimental conditions such as number of ions trapped and polarization of the laser light field with respect to the magnetic field direction is estimated in prior to extracting the transition frequencies. The details of the experimental procedures are identical to those reported in Chapter 4 with an improvement that the frequency ν_{494} during the cooling can be independently controlled in frequency and power. This results in a better control of the ion temperature over a large range of detunings and powers. In section 5.4 the absolute frequencies are determined.

5.3.1. Determination and control of absolute laser light frequencies

The determination of absolute laser light frequencies are required in order to determine the frequencies ν_1 and ν_2 at the position of the ions as given by Eqns. 2.6 and 2.7. This approach is identical to the method used in the determination of the transition frequency in $^{138}Ba^{+}$ as described in Chapter 2. The intermediate frequencies required to determine this are tabulated in Table 5.1.

In order to monitor and stabilize the frequency of light at wavelength λ_{494} the beat note between the TiSa laser light and the frequency comb is constantly recorded (see Chapter 2) and small variations are corrected

for. The absolute frequency of light at wavelength λ_{649} is given by Eq. 2.3. The absolute frequency accuracy is derived from frequency modulated saturated absorption spectroscopy of $^{127}I_2$ (see Chapter 3). In these experiments a diode laser is stabilized against the iodine transition and the absolute frequency is determined with the frequency comb. The stability of the iodine-stabilized diode laser is monitored as shown in Fig 5.7(a). The fit for the calibration of the diode laser frequency results in a frequency of 461312347.8392(15)MHz (Fig 5.7(b)).

Table 5.1.: Intermediate frequencies to determine the absolute laser frequencies according to the Eqns. 2.6 and 2.7. During measurements the repetition rate of the comb $\nu_{comb,rep}$ has been varied in order to change ν_1. ν_2.
*referenced to the Rb clock at 10^{-12} relative accuracy.
**limited by the accuracy of the line width of the laser lights within 100 ms counting period. The frequency of the laser light ν_{649} at wavelength λ_{649} is controlled by changing this frequency.

Frequency	Value
$\nu_{\mathrm{comb,rep}}$	250 000 332.5 Hz*
$\nu_{\mathrm{comb,offset}}$	−40 000 000.0 Hz*
For light at wavelength λ_{494}:	
m_1 (mode number)	1214851
$\nu_{\mathrm{B_1}}$	29.01(1) MHz**
$\nu^1_{AOM_{494}}$	198.8 MHz*
$\nu^2_{AOM_{494}}$	188.8 MHz*
For light at wavelength λ_{649}:	
m_2 (mode number)	1845248
$\nu_{\mathrm{B_2}}$	−30.44(3) MHz**
ν'_{B2}	−[976.2(1)–1072.0(1)] MHz**
$\nu_{\mathrm{AOM\text{-}2}}$ (double pass)	362.00 MHz*

In order to study the heating effects due to the change in laser detunings the spectra is recorded. The frequency of the laser light at λ_{649} is determined by see Eq 2.7. It is stepped across resonance. This frequency is controlled by changing the reference frequency to the frequency offset lock between the iodine stabilized diode laser and the dye laser (see section 2.2.4). Fluorescence photons from the $6p\,^2P_{1/2} - 6s\,^2S_{1/2}$ tran-

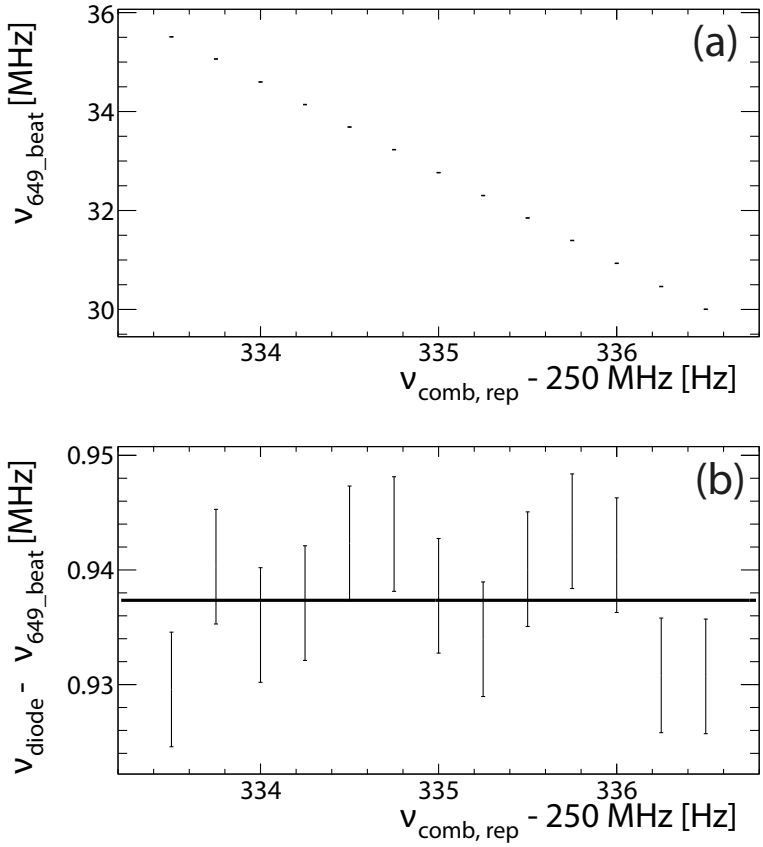

Figure 5.7.: (a) Beat note between iodine stabilized diode laser and frequency comb as a function of the repetition rate $\nu_{comb,rep}$ of the frequency comb. (b) The fit for the calibration of the diode laser frequency. Adding the offset for the calibration of the diode laser frequency results in a frequency of 461312347.8392(15)MHz.

sition are counted in 100 ms intervals. These are stored together with the other experimental parameters such as frequency ν_1, power P_{494} and P_{649} for laser light at wavelengths λ_{494} and λ_{649} respectively. Frequency is stepped in ascending and descending order for a frequency span of

100 MHz each in 200 s. We do not observe any difference in the line shape between stepping the frequency in ascending and descending order accross the resonance. This indicates that there is no observable bias in such a procedure towards extracting the transition frequencies.

The ion temperature is kept constant by Doppler cooling for most of the data acquisition time. This is achieved by fast switching between a fixed detuning for cooling for a fraction of 80% of the time and a detuning for spectroscopy (see Eqns. 2.5).The implementation of this method is described in Section 2.3.1. Sensitivity of the line shape to the switching duty cycle T_S is studied by recording spectra by varying the switching frequency, ν_s as 53 kHz, 23 kHz, 13 kHz and 6 kHz. The duty cycle for the measurements is given in Table. 5.2. This is done at a fixed frequency ν_{494} and fixed power of laser lights, P_{494} and P_{649} at wavelengths λ_{494} and λ_{649} respectively. No substantial change in the line shape was observed with different switching frequencies. The delay between switching rate and counter rate, t_d results in increased background scattering rate on the PMT when ν_s is higher.

Table 5.2.: Period for cooling and probing of the ion signal for the switch and the counter

	Fraction of cooling period T_c	Fraction of spectroscopy period T_s	Fraction-delay t_d
Switching duty cycle	0.80	0.20	0.05

5.3.2. Laser light properties

The optical resolution of spectral features depends on the intensity of laser light. Understanding the influence of intensity I_{494} of the laser light at λ_{494} to the spectrum is essential for this.

Fluorescence detected by the PMT is recorded for different power levels P_{494} of light at λ_{494} ranging from 0.26(2) µW to 27.8(2) µW at fixed frequency, ν_1 and at a fixed detuning δ_{494}. This low intensity become feasible by independently controlling the power P_{494} of laser light at wavelength λ_{494} during the cooling phase T_c (see section 2.3.1). The power P_{494} is recorded using a photo diode placed at the exit of the beams after going through the trap (see Fig. 2.17). The intensity is given by power per cross-sectional area of the beam overlapping the ion. A defined part of the spectra which is within 5 MHz is taken to determine the count rate at different power levels P_{494} as shown in Fig. 5.8(a). At higher intensities, the count rate drops. This is because the line shape changes with change in intensity I_{494} as expected in an eight-level system. The background scattering increases linearly with increase in power P_{494} as observed in Fig. 5.8(b). The relevant parameters for this measurement could be found in Appendix C.2.

The polarization of the laser light with respect to the magnetic field direction influences the line shape of the spectrum. The polarization of the two laser fields at wavelength λ_{494} and λ_{649} determine which coherence cause a florescence dip. This is explained in Chapter 4.

The influence of number of ions in the recorded line shape is studied here, see Fig 5.9. Spectra are recorded with six, five and one number of ions at a fixed frequency ν_1 and fixed power $P_{494} = 5.0(2)$ µW. The count rate increases with increase in photons scattered per ion and the spectrum gets distorted because of the heating from the ions. The spectra is less perturbed with a smaller number of ions in the trap. Appendix C.3 has a table of the relevant parameters for this measurement.

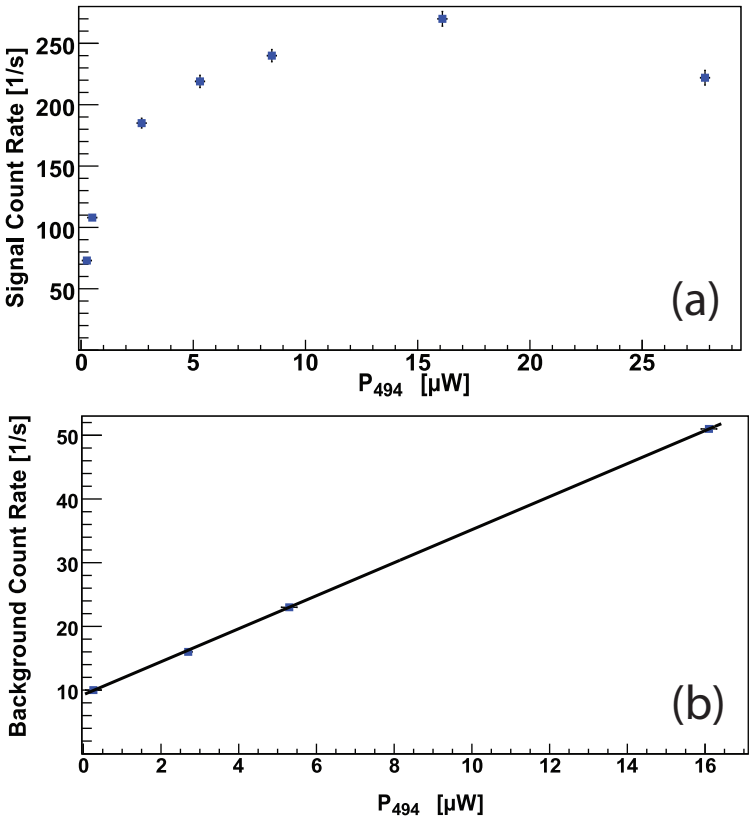

Figure 5.8.: Fuorescence from trapped ions detected by the PMT for different power P_{494} of laser light at λ_{494} at a fixed detuning, δ_{494}. The background scattering is subtracted from florescence from the ion signal detected by the PMT. The power dependence displays the saturation behavior in the three-level system. The background scattering detected by the PMT for various power levels of laser light at λ_{494} at a fixed detuning. The background scattering increases linearly with power, P_{494}. The dark count rate of the PMT accounts for the offset at $P_{494} = 0\,\mu W$. The uncertainties on the count rates are below symbol size.

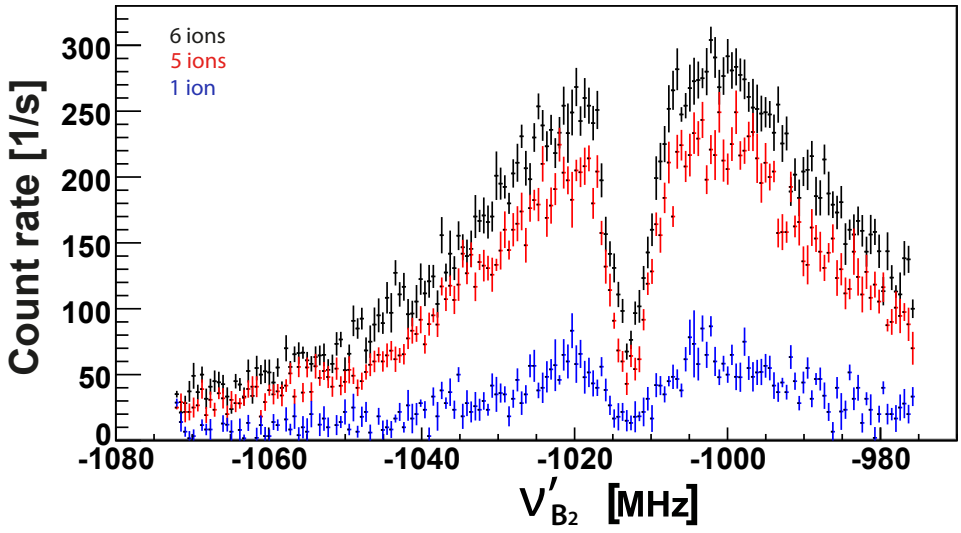

Figure 5.9.: Spectra of the $5d\,^2D_{3/2}$ – $6p\,^2P_{1/2}$ transition in $^{134}Ba^{+}$ ion recorded for six, five and one number of ions. The spectrum is less distorted when there is less number of ions.

5.4. Determination of transition frequencies in Ba^{+} ion

The choice of experimental parameters determines the observed spectral shape in order to extract the transition frequencies in the Ba^{+}. Spectra of the $5d\,^2D_{3/2} - 6p\,^2P_{1/2}$ are recorded for different experimental parameters by confining $^{134}Ba^{+}$ ions in the hyperbolic Paul trap. The Fano profile model (Eqn. 5.12) is fitted to individual spectra.

The quantization axis is defined by the magnetic field which is in the z-direction and both light fields are taken to propagate along the -y direction (see Fig. 4.3). The polarization of the light at wavelength λ_{494} is chosen to be linearly polarized, parallel to the magnetic field direction $\vec{B_z}$ and light at λ_{649} is chosen to be elliptically polarized. The line shape as a function of laser light intensities I_{494} and I_{649} of light at wavelengths λ_{494} and λ_{649} respectively and of laser detunings δ_1 (see Eqn. 5.4) are studied.

5.4.1. Fano model and experimental observation

The two photon induced dip in the spectrum appear near the condition of equal detuning $\delta_1 = \delta_2$ from the unperturbed states. The light shifts cause a small deviation from this condition in the experimentally observed signals. Only under the condition that both of the detunings approach zero, light shifts will vanish and the resultant spectrum becomes symmetric. Hence this becomes a preferred condition for extracting the absolute transition frequencies.

We collected series of data for different detuning $\delta 494$ but otherwise constant conditions (Fig. 5.11). The step size of 0.61 MHz arises from a change of the repetition rate $\nu_{comb,rep}$ of 0.25 Hz. The two -photon resonance then appear at different frequencies and we come close to the condition of zero detuning from the unperturbed transition frequency ω_{494} in the Ba^{+} ion. The spectra are fitted individually to the Fano-profile (Eq. 5.12)and fit results are depicted in Fig. 5.11. The fit parameters for a Fano - profile is described in Fig. 5.12. The overall behavior of the fitted parameters agree very well with the fitting to the OBE calculations (Fig. 5.3. The statistical uncertainty from the experimental spectra of about 0.3 MHz do not allow to resolve the fine structure seen in the OBE calculations. The relevant parameters for this measurement is tabulated in Appendix C.4.

Uncertainties of the recorded data are extracted from counting statistics. The obtained reduced χ^2/NDF ranges from 1.0 - 1.8. This is slightly larger than the expectation value of $\chi^2/NDF = 1$. The explanation for the increased χ^2 in these experiments are other noise sources which have not been taken explicitly into account. These other contributions to the uncertainty arise from fluctuations in the power of the laser lights, laser light intensity variation and possible fluctuation of the ion temperature during the recording period of the spectrum (about 200 s). Taking into account that the atomic system under consideration is an eight-level system, the data is highly non-linear and therefore cannot be normalized although this is not a limitation for the extraction of the relevant transition frequencies.

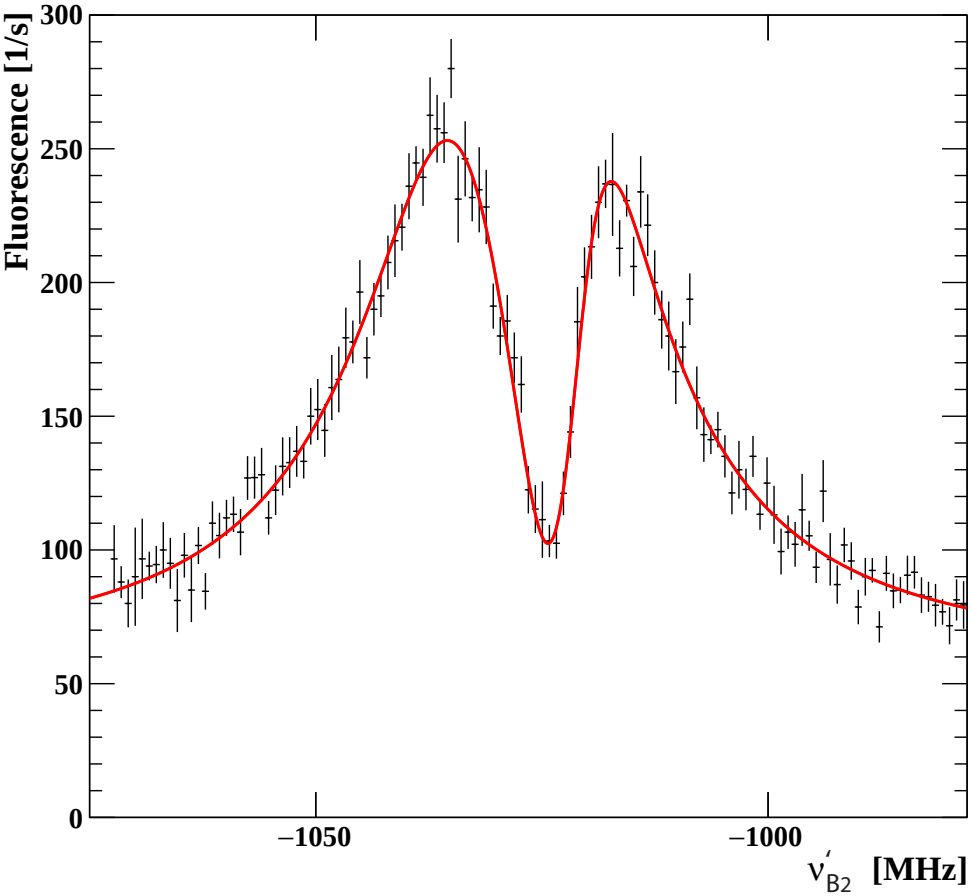

Figure 5.10.: An example of the spectrum of the $5d\,^2D_{3/2} - 6p\,^2P_{1/2}$ transition in $^{134}Ba^{+}$ ion for a positive detuning δ_{494} of the $6s\,^2S_{1/2} - 6p\,^2P_{1/2}$ transition. The uncertainties for any given data point is taken from counting statistics on the number of recorded fluorescence photons. The red solid line is the result from fitting the data against the Fano profile (Eqn. 5.12), which yields reduced χ^2 of 121.4/115. The extracted parameters are: ν_1 = -1031.3(4) MHz, Γ_1 = 18.9(7) MHz, N_1 = 2230(250), ν_2 = -1021.5(4) MHz, Γ_2 = 5.2(3) MHz, N_2 = 570(90), ϕ = -4.47(13) rad, and bkg = 59(3).

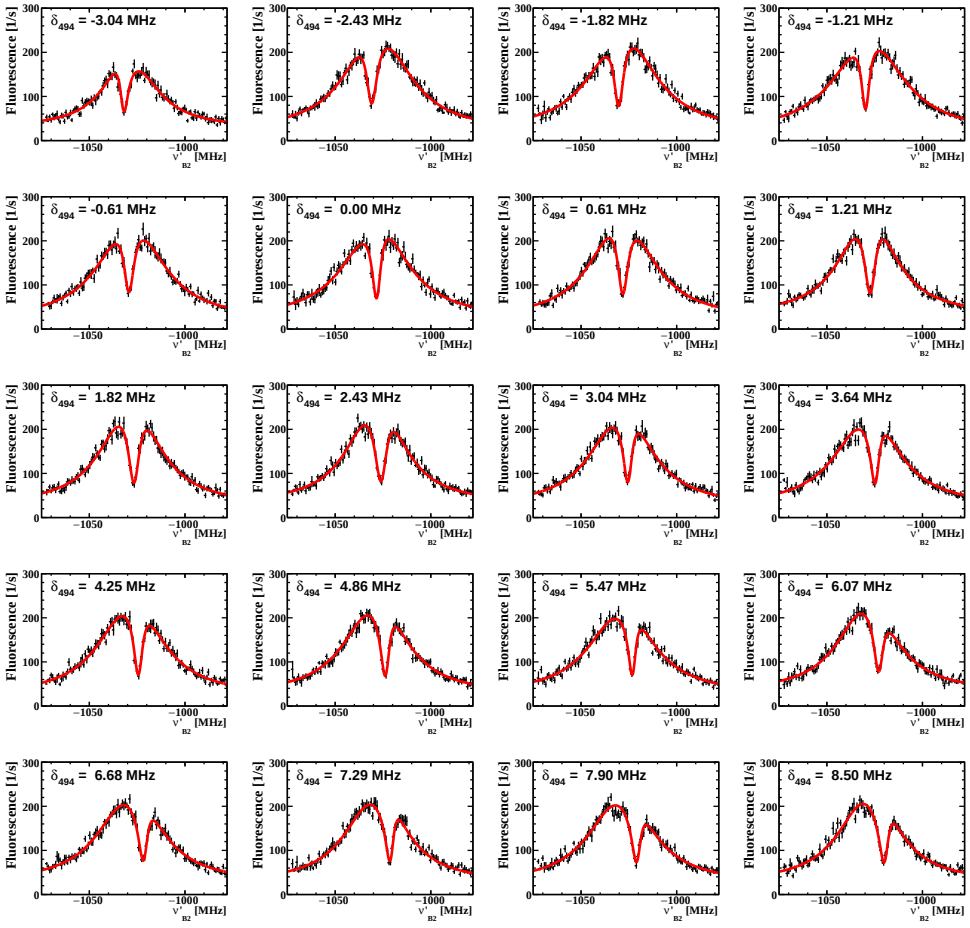

Figure 5.11.: Raman spectra of the $5d\,^2D_{3/2}$ - $6p\,^2P_{1/2}$ transition in $^{134}Ba^{+}$ ion recorded for different detunings δ_{494}. Solid lines correspond to the result of fitting the Fano-profile to the individual spectra. Time taken for a single scan to obtain the spectra is 200 s. The statistical uncertainty on the frequencies extracted for a single scan is about 400 kHz.

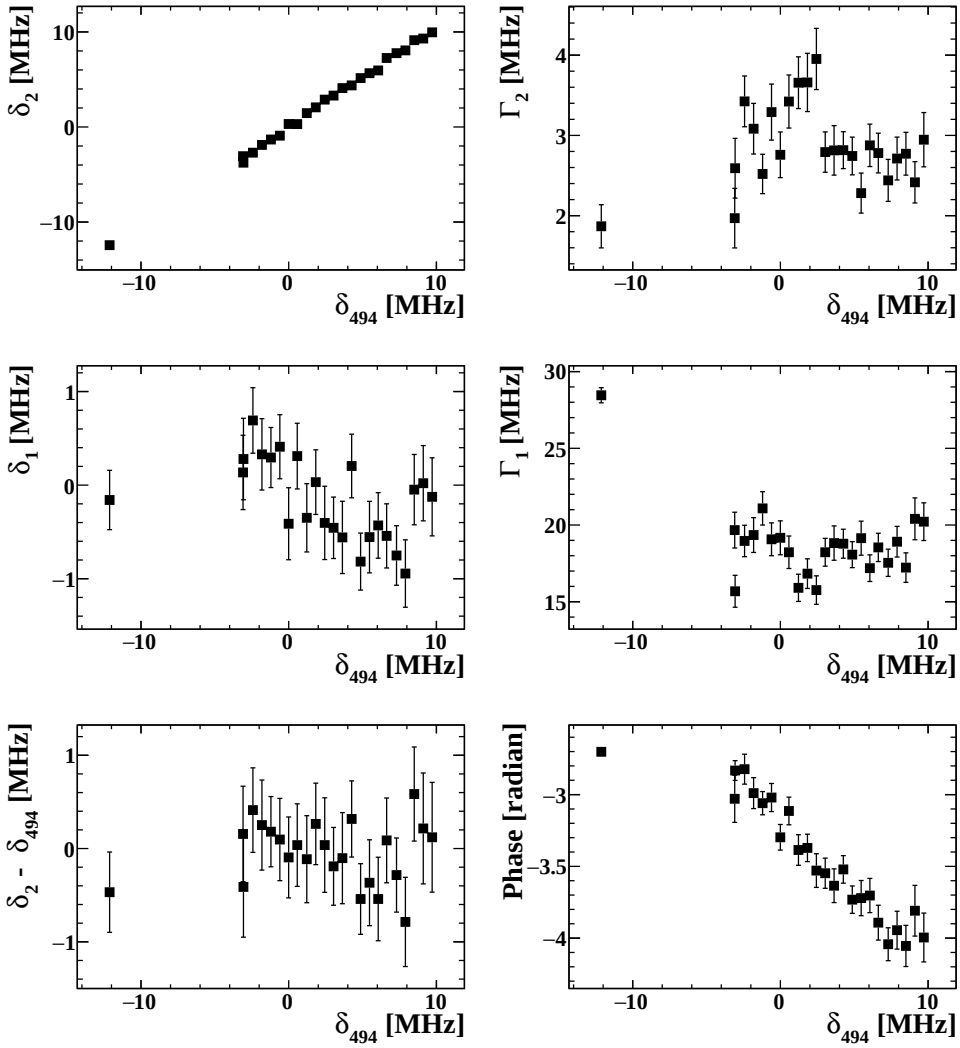

Figure 5.12.: Results from fitting a Fano profile to Raman spectra of the $5d\,^2D_{3/2}$ - $6p\,^2P_{1/2}$ transition in Ba^+ ion recorded for different detunings δ_{494} for laser at wavelength λ_{494}. Spectra are recorded with positive and negative detunings δ_{494}. A symmetric response to frequencies ν_{Raman} and ν_{D-P} on either side of the resonance (at $\nu_{494} = 0$) indicates the light shift. The data point at δ_{494}= -12 MHz has a higher power P_{649} of light at wavelength λ_{649}. The results obtained are comparable with the results from simulation given in Fig 5.4 within the error bars with change in detuning. The range of experimental data is smaller than the calculated data.

5.4.2. Laser light intensities

Laser light intensities not only influence the rate of observed scattering photons, but also the line shape and the extracted transition frequencies. The quantitative determination of the transition frequencies in the Fano line shape model provides access to intensity depended shifts. These near resonant light shifts do not scale linear in intensities. Their dependence can be experimentally determined in the discussed approach. A good understanding of the observed spectra thus permits the calibration of the intensities at the ion position. Such a method is indispensable for the exploitation of single ion spectroscopy in order to extract the contribution from weak interactions in atomic systems (Chapter 2). The light intensities are varied using changing rf-voltage to AOM-494 and AOM-649 for light at wavelengths λ_{494} and λ_{649} (see Section 2.3.1). This changes the power level but not the mode of the laser light. The intensity is given by the power per cross-sectional area of the beam overlapping the ion. The Rabi frequencies Ω_1 and Ω_2 are obtained by quantifying the laser powers at wavelengths λ_{494} and λ_{649}.

The sensitivity of the Raman spectra for power P_{494} for light at wavelength λ_{494} is inspected. A Fano-profile is fitted to individual spectra of the $5d\,^2D_{3/2}$ - $6p\,^2P_{1/2}$ transition in $^{134}Ba^{+}$ ion recorded with different power P_{494} at a fixed frequency ν_{494} and a fixed detuning δ_{494}. The results following from the fitted data are shown in Fig 5.14. Table containing the relevant parameters for this measurement is given in Appendix C.5. The results are in excellent agreement with the one obtained in Fig. 5.5 which is the result from fitting a Fano profile to the simulated data from the calculated steady state solutions of the Optical Bloch Equation. This justifies that the Fano profile is a valid model which provides a physical insight in coherent population trapping.

Additional spectra of the $5d\,^2D_{3/2}$ - $6p\,^2P_{1/2}$ transition in $^{134}Ba^{+}$ ion have been recorded at different power P_{649} for laser light at wavelength λ_{649} at a fixed frequency ν_1 and a fixed detuning δ_1. A Fano-profile is fitted to individual spectra and the results are shown in Fig. 5.16. This is comparable to the results obtained in Fig. 5.6. Table containing the relevant parameters for this measurement is given in Appendix C.8.

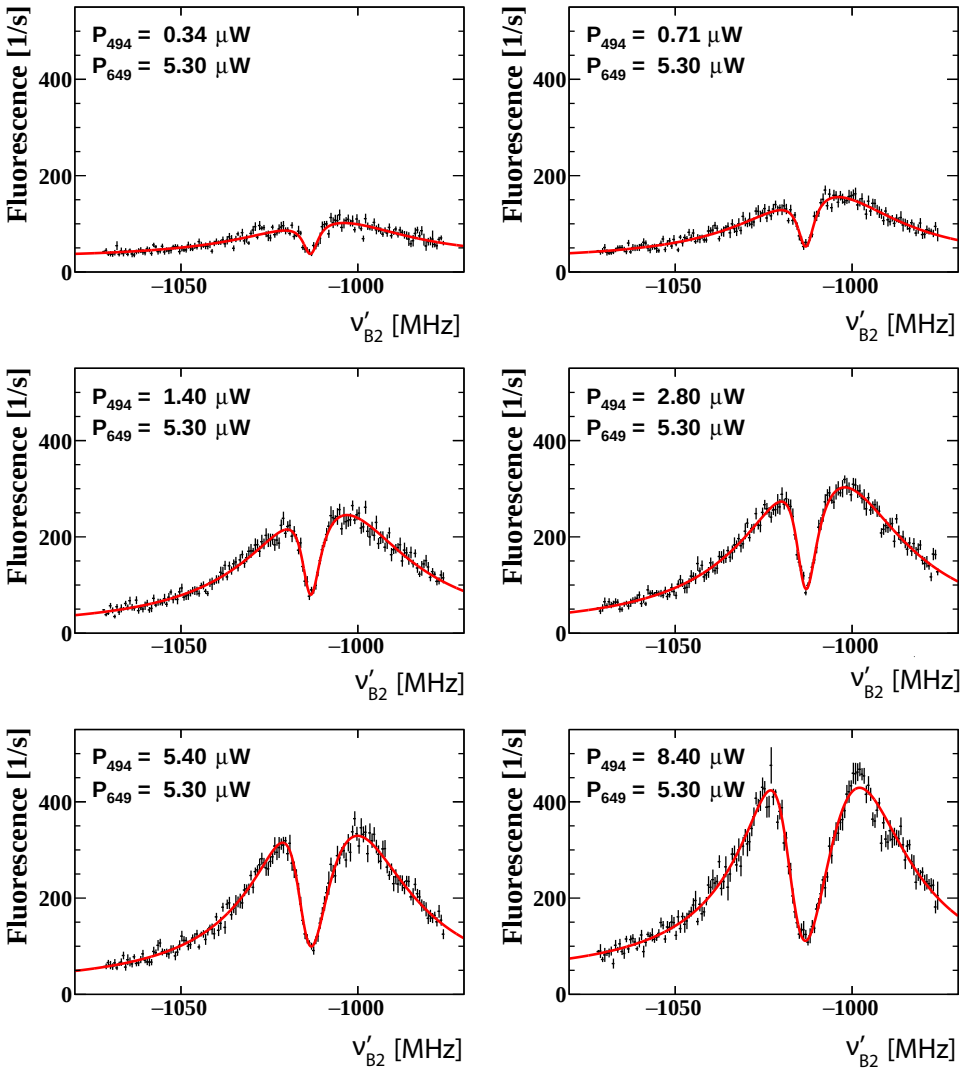

Figure 5.13.: Individual fit of Fano-profile to spectra of the $5d\,^2D_{3/2} - 6p\,^2P_{1/2}$ transition in $^{134}Ba^{+}$ ion recorded for different powers P_{494} of light at wavelength λ_{494}. The power is measured using a power meter outside the vacuum chamber with an accuracy of about 5% (Fig. 2.16).

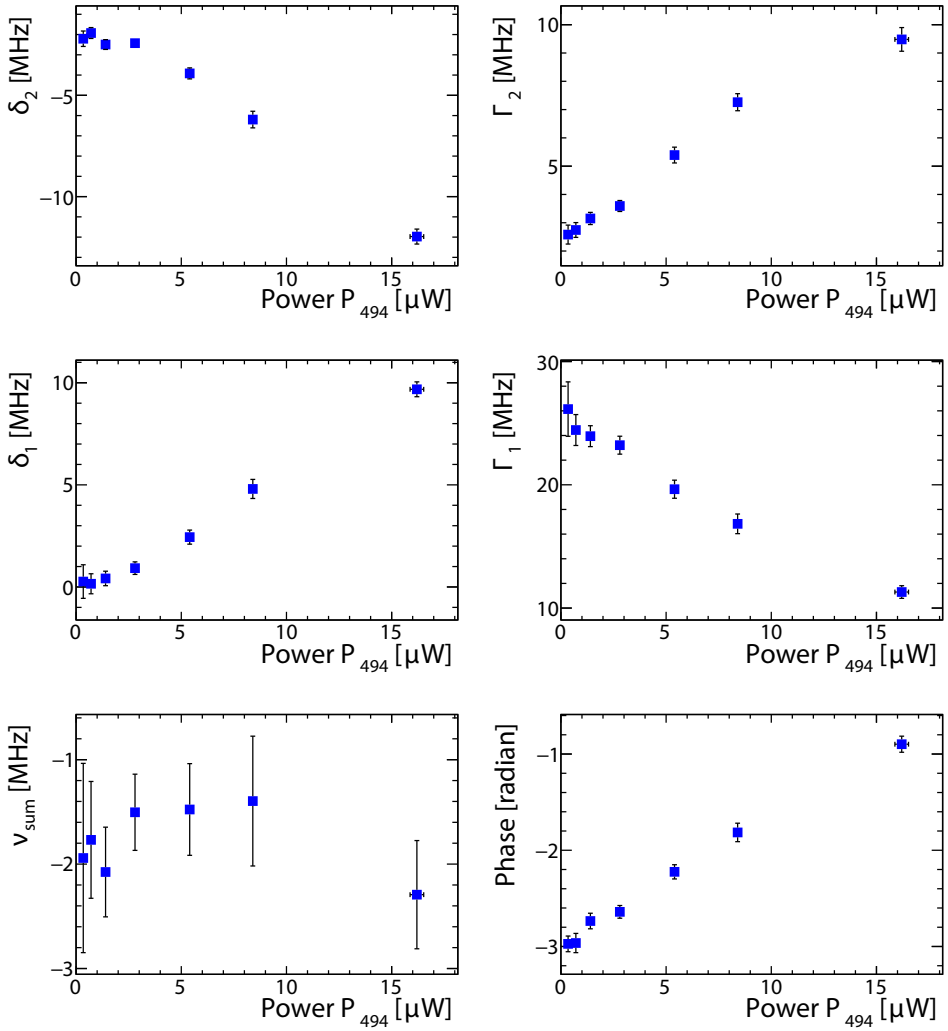

Figure 5.14.: Results from fitting a Fano-profile to spectra of the $5d\,^2D_{3/2} - 6p\,^2P_{1/2}$ transition in Ba^+ ion recorded for different powers P_{494} of light at wavelength λ_{494}. The results are comparable to that obtained by fitting Fano profile to the simulated data from the calculated steady state solutions of the OBE as given in Fig. 5.5. The shift is small at lower intensities.

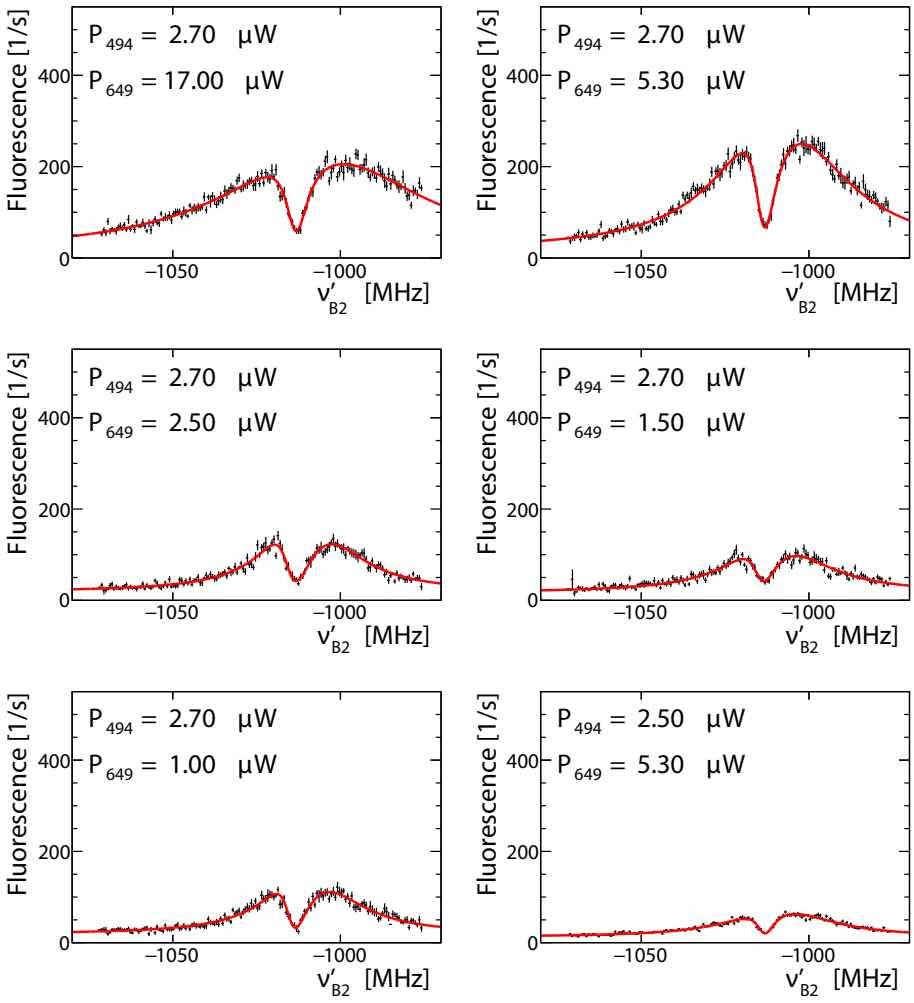

Figure 5.15.: Fano-profile fit to spectrum of the $5d\,^2D_{3/2} - 6p\,^2P_{1/2}$ transition in Ba^+ ion recorded for different powers P_{649} of light at wavelength λ_{649}. The power is measured using a power meter outside the vacuum chamber with an accuracy of about 5% (Fig. 2.16).

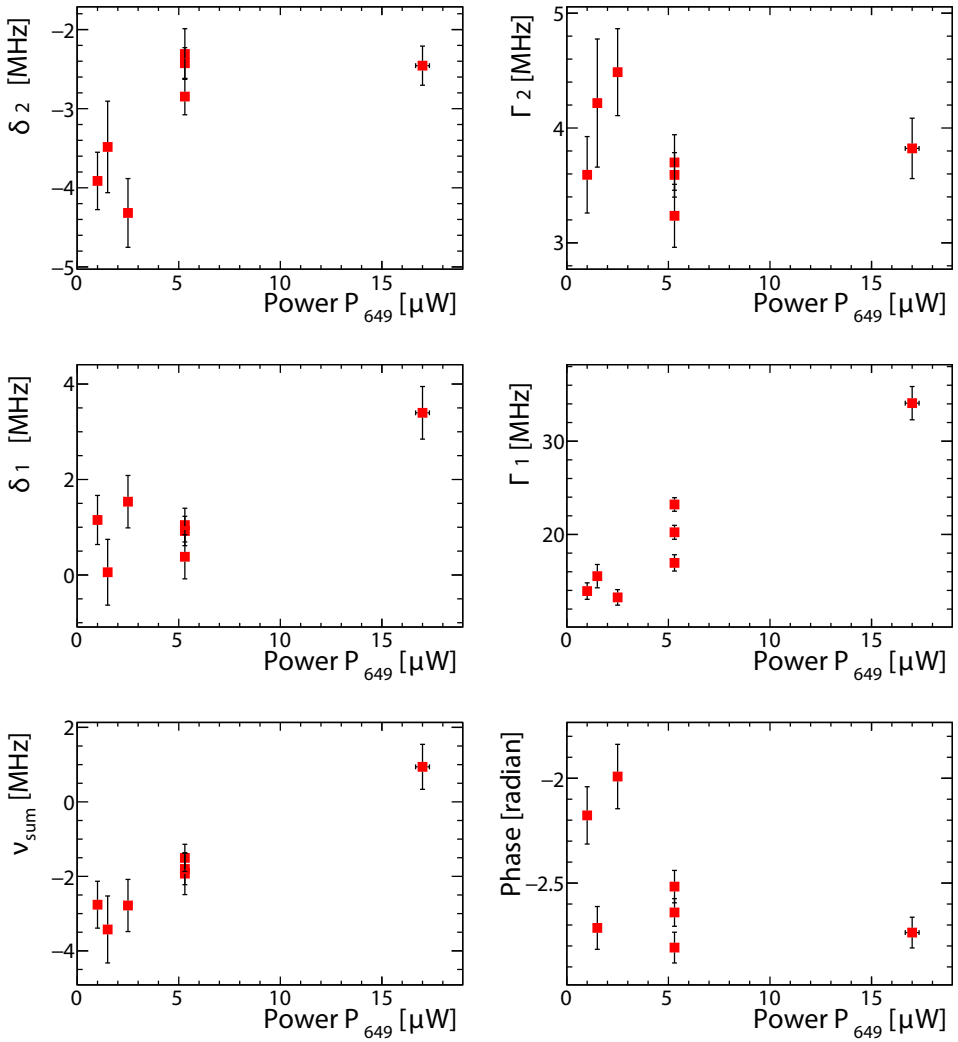

Figure 5.16.: Results from fitting a Fano-profile to spectrum of the $5d\,^2D_{3/2} - 6p\,^2P_{1/2}$ transition in Ba^{+} ion recorded for different powers P_{649} of light at wavelength λ_{649}. We observe that the shift is small at lower intensities.

5.4.3. Determination of transition frequencies in $^{136}Ba^{+}$ system

The oven containing the isotope $^{136}Ba^{+}$ is resistively heated and by on resonant photoionization $^{136}Ba^{+}$ ions are produces and trapped (see Chapter 2) in order to extract the transition frequencies of $5d\,^2D_{3/2} - 6p\,^2P_{1/2}$, $6s\,^2S_{1/2} - 5d\,^2D_{3/2}$ and $6s\,^2S_{1/2} - 6p\,^2P_{1/2}$ transitions in $^{136}Ba^{+}$. Spectra of the $5d\,^2D_{3/2}$ - $6p\,^2P_{1/2}$ transition in Ba^{+} ion are recorded at a fixed detuning δ_{494} with different power P_{494} of light at wavelength λ_{494}. The relevant parameters required to determine the frequencies ν_1 and ν_2 are tabulated in Table 5.3. Some unknown impurities in the sample of $^{136}Ba^{+}$ mixture resulted in producing too small atomic flux from the oven which limited the quantity of the data collected.

Raman spectra of the $5d\,^2D_{3/2}$ - $6p\,^2P_{1/2}$ transition in $^{136}Ba^{+}$ ion is recorded for different detunings δ_{494} and Fano - profile is fitted to individual spectra (Fig. 5.17). Since the spectrum is not measured on resonance but slightly negative detuned the frequency has been estimated from light shifts. Fig.5.18 shows the result from fitting the Fano-profile to the recorded data.

Table 5.3.: The parameters for spectra recorded to determine transition frequency in $^{136}Ba^{+}$ system. Measurements are taken at a constant frequency ν_1 .

Parameter	Value
$\nu_{comb,rep}$	250 000 314.5 Hz
ν'_{B2}	-[1080(1)-1180.0(1)] MHz
$\nu_{AOM_{649}}$	352.00 MHz

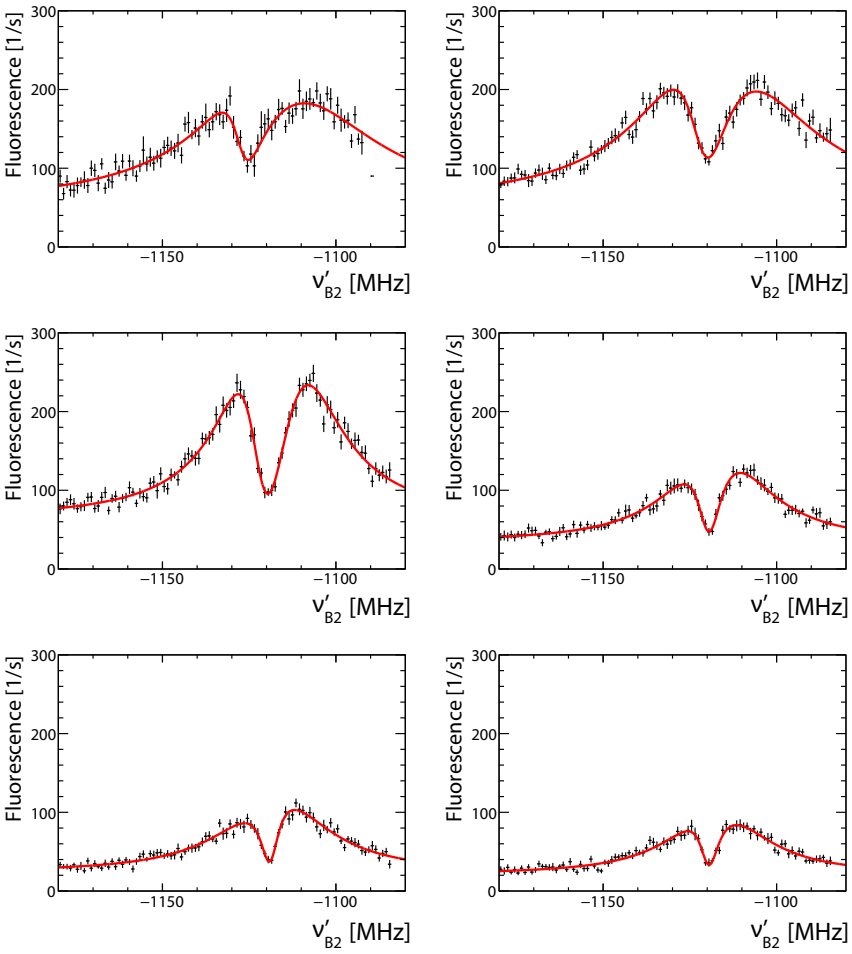

Figure 5.17.: All data sets collected with isotope $^{136}Ba^{+}$. Solid lines correspond to the result of fitting the Fano-profile to the individual spectra.

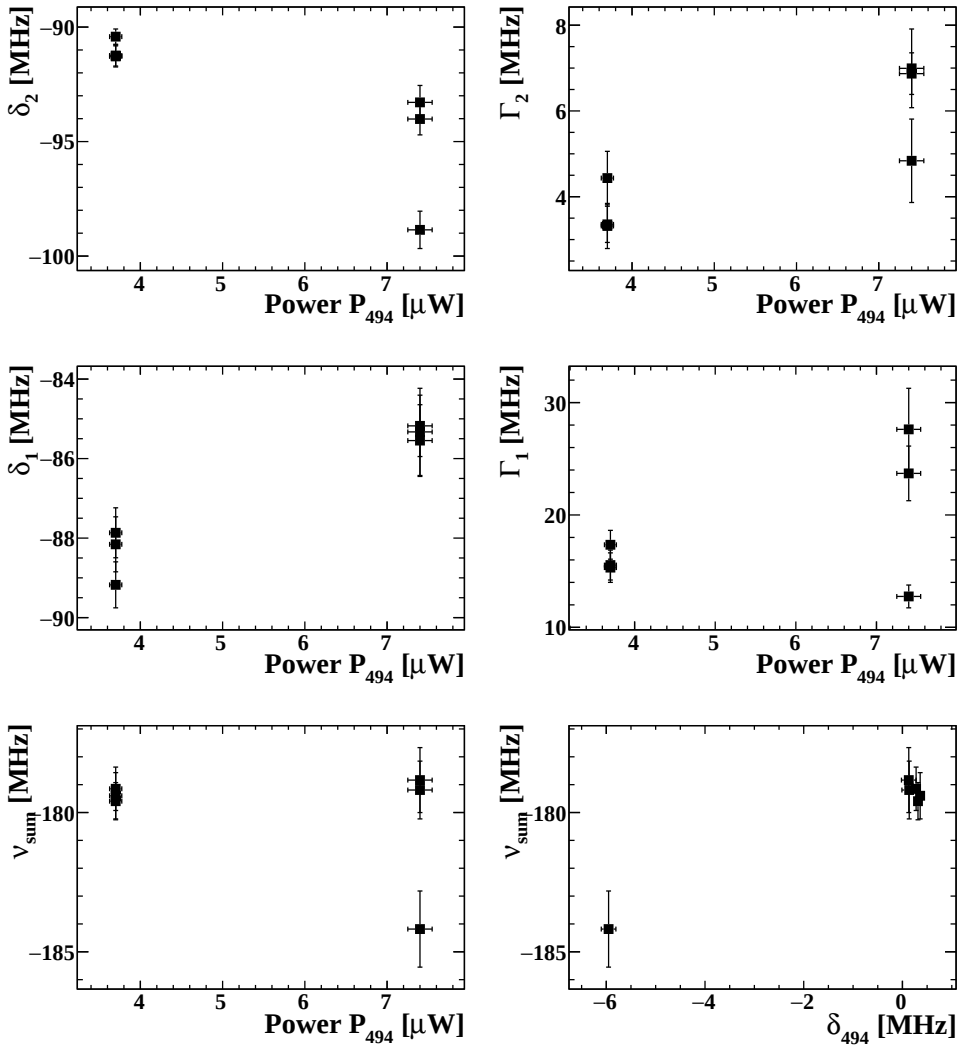

Figure 5.18.: Results from fitting a Fano profile to Raman spectra of the $5d\,^2D_{3/2}$ - $6p\,^2P_{1/2}$ transition in $^{136}Ba^{+}$ ion recorded for different detunings δ_{494} for laser at wavelength λ_{494}.

5.5. Results and conclusions

In virtue of the line shape analysis using a Fano profile fit, optimum parameters are selected in order to extract the transition frequencies of $5d\,^2D_{3/2} - 6p\,^2P_{1/2}$, $6s\,^2S_{1/2} - 5d\,^2D_{3/2}$ and $6s\,^2S_{1/2} - 6p\,^2P_{1/2}$ transitions in $^{134}Ba^{+}$ and $^{136}Ba^{+}$ system. The spectrum chosen to extract the relevant transition frequencies involve,

1. Polarization of the light at wavelength λ_{494} as linearly polarized, parallel to the magnetic field direction $\vec{B_z}$ and light at wavelength λ_{649} as elliptically polarized which makes the dominant contributions from coherence $|1\rangle\langle 8|$ and $|2\rangle\langle 5|$ resulting in a spectra with a dip in fluorescence caused by the two-photon process.

2. Spectra recorded at resonance condition that $\delta_1 = \delta_2 = 0$ so that the spectra is symmetric and the light shifts and other systematic effects are zero (see section 5.4.1).

3. Low intensity for light at wavelengths λ_{494} and λ_{649} which drives the transition $6s\,^2S_{1/2} - 6p\,^2P_{1/2}$ and $5d\,^2D_{3/2} - 6p\,^2P_{1/2}$ respectively. This choice makes the frequency shifts reasonably small (see section 5.4.2).

From our measurements we extract the transition frequencies between the 3 lowest lying states in $^{134}Ba^{+}$ and $^{136}Ba^{+}$(see table 5.4 and table 5.5). Measurements in isotopes other than $^{138}Ba^{+}$ suffer from the low abundance of these isotopes and associated experimental difficulties to prepare clean sample.

5.5.1. Transition frequencies in $^{134}Ba^{+}$

The transition frequencies between the 3 lowest lying states in $^{136}Ba^{+}$ are extracted. The accuracy is within a factor of 4 to the one obtained previously for $^{138}Ba^{+}$. These measurements are a factor of about 50 better than very recent results in $^{130,132}Ba^{+}$ [108].

Table 5.4.: Transition frequencies of the $5d\,^2D_{3/2}$ – $6p\,^2P_{1/2}$ and $6s\,^2S_{1/2}$ – $5d\,^2D_{3/2}$ transitions in $^{134}Ba^{+}$. Their sum yields the frequency of the $6s\,^2S_{1/2}$ – $6p\,^2P_{1/2}$ transition.

Transition	Frequency (MHz)	Relative uncertainty
$\nu_{(5d\,^2D_{3/2}-6p\,^2P_{1/2})}$	461 312 056.5(2)	5×10^{-10}
$\nu_{(6s\,^2S_{1/2}-5d\,^2D_{3/2})}$	146 114 429.1(4)	3×10^{-09}
$\nu_{(6s\,^2S_{1/2}-6p\,^2P_{1/2})}$	607 426 485.5(4)	7×10^{-10}

5.5.2. Transition frequencies in $^{136}Ba^{+}$

The transition frequencies between the 3 lowest lying states in $^{136}Ba^{+}$ are extracted. The accuracy is within a factor of 4 to the one obtained previously for $^{138}Ba^{+}$. These measurements are a factor of about 50 better than very recent results in $^{130,132}Ba^{+}$ [108].

Table 5.5.: Transition frequencies of the $5d\,^2D_{3/2}$ – $6p\,^2P_{1/2}$ and $6s\,^2S_{1/2}$ – $5d\,^2D_{3/2}$ transitions in $^{136}Ba^{+}$. Their sum yields the frequency of the $6s\,^2S_{1/2}$ – $6p\,^2P_{1/2}$ transition.

Transition	Frequency (MHz)	Relative uncertainty
$\nu_{(5d\,^2D_{3/2}-6p\,^2P_{1/2})}$	461 311 949.1(3)	7×10^{-10}
$\nu_{(6s\,^2S_{1/2}-5d\,^2D_{3/2})}$	146 114 494.5(4)	3×10^{-09}
$\nu_{(6s\,^2S_{1/2}-6p\,^2P_{1/2})}$	607 426 443.5(2)	3×10^{-10}

5.5.3. Isotope shifts of the $6s\,^2S_{1/2} - 6p\,^2P_{1/2}$ and $6p\,^2P_{1/2} - 5d\,^2D_{3/2}$ electronic transitions of barium ions

Isotope shift in the three transitions $6p\,^2P_{1/2}-5d\,^2D_{3/2}$, $6s\,^2S_{1/2}-6p\,^2P_{1/2}$ and $6s\,^2S_{1/2} - 5d\,^2D_{3/2}$ for the even Ba^+ isotopes, $^{130}Ba^+$, $^{132}Ba^+$ [109, 108], $^{134}Ba^+$, $^{136}Ba^+$ [this work] with respect to $^{138}Ba^+$ [this work] are tabulated in table 5.6.

Table 5.6.: Isotope shifts of the $6p\,^2P_{1/2}$ - $6s\,^2S_{1/2}$ ($\delta\nu^b$) and $6p\,^2P_{1/2}$ - $5d\,^2D_{3/2}$ ($\delta\nu^r$) electronic transitions of barium ions. The isotope shift is relative to the transitions in $^{138}Ba^+$ and $\delta\nu^i = \nu^i_A$-ν^i_{138}.

A	I	$\delta\nu^b$ (MHz)	$\delta\nu^r$ (MHz)	Ref
130	0	355(20)	394(10)	[108]
132	0	278(20)	292(10)	[108]
134	0	223.0(0.3)	177.9(0.3)	this work
136	0	181.1(2)	70.6(2)	this work

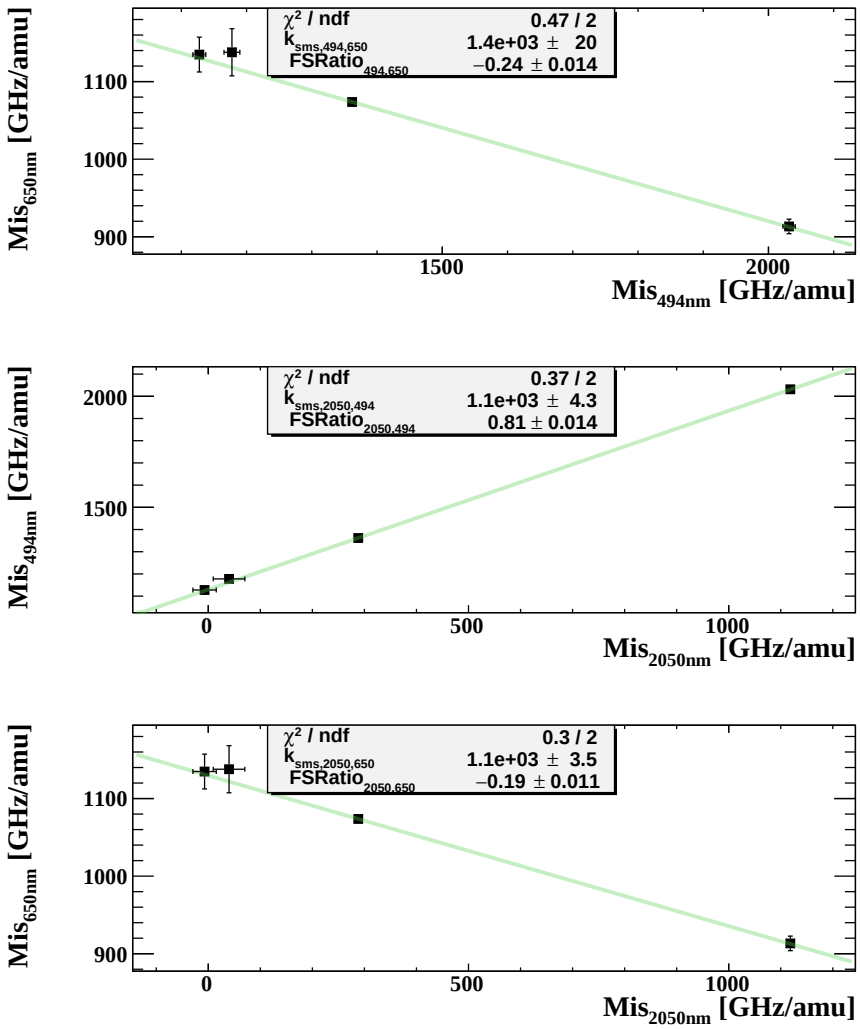

Figure 5.19.: Comparison of isotope shifts in a King plot in the three transitions $6p\,^2P_{1/2} - 5d\,^2D_{3/2}$, $6s\,^2S_{1/2} - 6p\,^2P_{1/2}$ and $6s\,^2S_{1/2} - 5d\,^2D_{3/2}$ for the even Ba^+ isotopes, $^{130}Ba^+$, $^{132}Ba^+$ [109, 108], $^{134}Ba^+$, $^{136}Ba^+$ [this work] with respect to $^{138}Ba^+$ [this work]. This method and usage of frequency comb technology have resulted in 100 times improved precision compared to previous work.

A test of consistency of isotope shift measurement can be done by comparing the scaling of shifts for different transitions. Here we have data on three optical transitions $5d\,^2D_{3/2} - 6p\,^2P_{1/2}$, $6s\,^2S_{1/2} - 6p\,^2P_{1/2}$ and $6s\,^2S_{1/2} - 5d\,^2D_{3/2}$ and five isotopes, $^{130}Ba^{+}$, $^{132}Ba^{+}$, $^{134}Ba^{+}$, $^{136}Ba^{+}$ and $^{138}Ba^{+}$ are available (see King plot in Figure 5.19). The isotope shift calculations are given in subsection 1.3.2. This work achieved a 100 fold improved precision due to the method and the usage of frequency comb technology.

The description of three-level system with Fano-profile rather than Optical Bloch Equations offers direct access to parameters such as intensity and detuning dependent light shifts. The analysis of the recorded data using Fano profiles provides most accurate values for the transition frequencies in the electronic three-level system $^{134}Ba^{+}$ and $^{136}Ba^{+}$, in particular the $6s\,^2S_{1/2} - 6p\,^2P_{1/2}$, $5d\,^2D_{3/2} - 6p\,^2P_{1/2}$ and $6s\,^2S_{1/2} - 5d\,^2D_{3/2}$ transitions. The achieved precision is 0.3 MHz for $^{134}Ba^{+}$ and 3 MHz for $^{136}Ba^{+}$, where we had less atoms available for these experiments. This improves the isotope shifts by a factor of 3 to 10 over previous measurements and confirms previous results on transition in $^{138}Ba^{+}$.

6. Conclusion and Outlook

High-precision test of electroweak theory puts strong constraints on the Standard Model (SM) of particle physics. Atomic Parity Violation (APV) utilizes low-energy system and gives access to the weak mixing angle, $\sin^2\theta_W$, a fundamental SM parameter, at low-momentum transfer. APV experiments are sensitive to new physics beyond SM at energies that cannot be currently achieved in colliders. The APV effects has strong enhancement in heavy atom. An independent measurement of the weak mixing angle ($\sin^2\theta_W$) is designed by doing experiments with laser and radio frequency cooling and trapping techniques on barium and radium ion. This enables to improve on the landmark result for APV measured in atomic cesium over some five orders of magnitude. A technique for single ions using an APV spin rotation produced by the "light shift" of the ground state Larmor precession frequency [46] is employed for measuring APV.

Essential for an APV measurement is the understanding of atomic theory at few percent level of accuracy. This depends on the accuracy of the knowledge of the atomic structure of the ion in consideration. This thesis discusses about the significance of underlying line shape, absolute transition frequencies and isotope shifts in Ba^+ which are the essential ingredients towards atomic wavefunction calculations.

For long measurement time and for excellent control of experimental parameters the ion needs to be localized to better than one optical wavelength. Hence a hyperbolic rf- Paul trap for trapping Ba^+ ion is constructed and mounted inside a vacuum chamber with the residual gas pressure maintained below a few times 10^{-11} mbar. It serves as a precursor for the isoelectric Ra^+ ion. The Paul trap ("trap 1") contains $^{138}Ba^+$ isotope and the trap discussed in this thesis ("trap 2") is a modification of "trap 1" and contains two different isotopes $^{134}Ba^+$ and $^{136}Ba^+$

(Chapter 2). The trap is mounted with eight auxiliary electrodes to compensate for the stray electric fields developed inside which shortens the lifetime of the trapped ions. Relative frequency stability of 10^{-11} for the laser system is achieved by employing hyperfine transitions in molecular $^{127}I_2$ and an optical frequency comb.

Understanding the underlying line shape is important in precision measurements to define and investigate the effects of external parameters. A line shape analysis of signals from frequency modulated saturated absorption spectroscopy of hyperfine transitions in molecular $^{127}I_2$ as frequency reference is carried out to determine the absolute center frequencies of the lines and to understand the effect of external parameters on the signal (Chapter 3). A Voigt function is used to describe the line shape and the center frequency of the lines are determined with an accuracy of 10^{-11} after correction to the pressure shift. The fit function is valid over a large range of experimental parameters, including vapor pressure in the range of 4 Pa to 137 Pa. Residual amplitude modulation, which is inherent in modulation spectroscopy, up to 1% on the lines induces shifts of the zero crossing of the dispersive line shape.

Transition frequencies between low-lying energy levels in a single trapped $^{138}Ba^+$ ion have been measured with laser spectroscopy referenced to an optical frequency comb (Chapter 4). An eight level optical Bloch model is used to describe the line shape and to extract the frequencies of one-photon and two-photon components of the line shape. A line shape calculated by numerically solving the eight level optical Bloch equations (OBE) is fitted to each individual spectrum. Intensity-dependent light shift effects are included in the optical Bloch equations drop out in the fitting procedure and the atomic transition frequency is determined by extrapolating the fitted value to zero laser intensity. The transition frequencies of the $6s\,^2S_{1/2} - 6p\,^2P_{1/2}$, $6s\,^2S_{1/2} - 5d\,^2D_{3/2}$, $6p\,^2P_{1/2} - 5d\,^2D_{3/2}$ transitions in $^{138}Ba^+$ are determined to sub-MHz precision which is an improvement of more than a factor of 100 over previous determinations.

A Fano-profile is employed to describe the line shape for trapped $^{134}Ba^+$ and $^{136}Ba^+$ ions towards the determination of the transition frequencies of the $6s\,^2S_{1/2} - 6p\,^2P_{1/2}$, $6s\,^2S_{1/2} - 5d\,^2D_{3/2}$, $6p\,^2P_{1/2} - 5d\,^2D_{3/2}$ transitions (Chapter 5). Under certain conditions for a 3-level Lambda system

the steady state solution of OBE is equivalent to a Fano-profile. A set of simulated data is provided to verify the same. The Fano-profile describes the two interference pathways, the excitation of the S-P transition by one photon from the laser field at ν_1 and the three step process via a virtual intermediate state to get to the final state which is the spontaneous emission of a photon from the P state. This approach gives a physical interpretation of the Raman resonance condition thereby making it possible to extract the light shift due to the coupling of the energy levels with the photons.

The determination of transition frequencies for the three isotopes, $^{138}Ba^+$, $^{134}Ba^+$ and $^{136}Ba^+$ gives access to the isotope shift in Ba^+. Isotope shifts (IS) are ideal probes for the atomic wave functions at the position of the nucleus and experimental IS data can be used to test the precise theoretical predictions. In addition, by comparing very accurate APV measurements on a string of isotopes of the same element the atomic calculations could be improved by canceling atomic structure uncertainties.

Validity of calculated atomic structure, in particular the wave functions is crucial for measurements on atomic systems. Lifetime measurements provide transition matrix elements. Continuous quantum jump spectroscopy is employed and the lifetime of the long-lived $5d^2D_{5/2}$ level in $^{138}Ba^+$ ions is measured in trapped single ions and small ion crystals [110, 61] (see Fig 6.1).

Experimental parameters that could potentially have caused systematic effects have been scrutinized. The lifetime is found to be $\tau_{D_{5/2}} = 25.6(0.5)$s, which is significantly below previously reported values (see Fig 6.2). This includes a correction for the statistically significant contribution to the decay rate of quenching caused by background gas collisions, a small correction from black-body radiation, and a small correction for bias introduced by the analysis procedure.

The systematic effects for an APV experiment need an elaborate and careful study. Deviation of relevant experimental parameters such as polarization of light fields and ion location, may cause systematic level shifts that mimic the parity violating light shift.

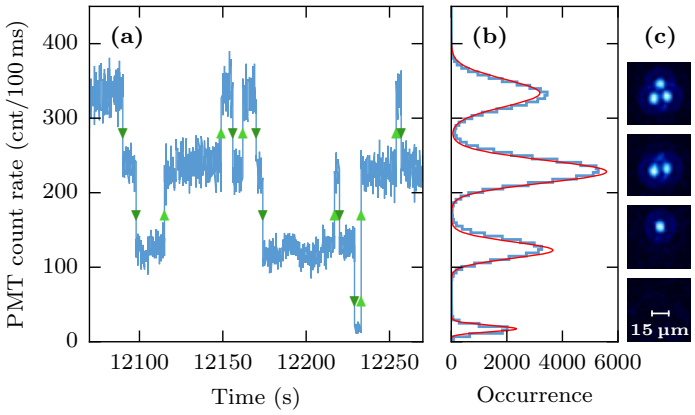

Figure 6.1.: Example of quantum jump data of a crystal of three Ba^+ ions. (a) A 3-min recorded trace of fluorescence at 494 nm. Arrows indicate crossing the thresholds set in the analysis. (b) Projection of the count rate at 100 ms time resolution fitted with a model based on Poisson statistics to determine the threshold levels. (c) Example of EMCCD images of the ion crystal. (Adapted from [110]).

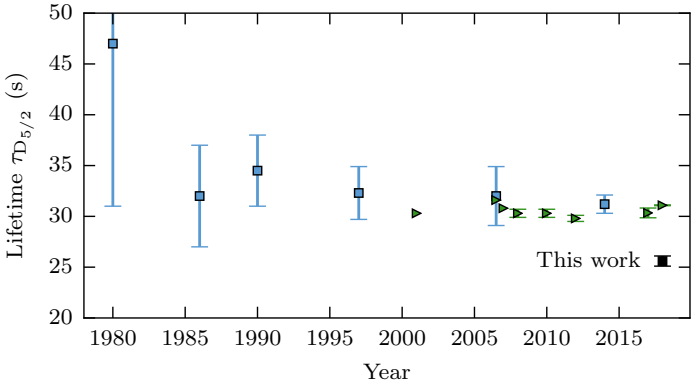

Figure 6.2.: History of measurements (■) and calculations (▶) of the $5d^2D_{5/2}$ level lifetime in Ba [110].

A method of measuring an on-resonant, parity violating, vector light shift in the $6S_{1/2}$ state of Ba^+ with the application of standing waves with 2050 nm light (see Fig 1.12) is planned. Vacuum compatible high finesse cavities to produce and control these standing waves are in preparation. This experiment also has a good perspective for a single ion clock with a potential of 10^{-18} relative uncertainty. The long term drift in the clock frequency, once the atomic energy level shifts are under control can be interpreted as temporal variations in the fundamental constants of nature itself. All aspects of the APV measurement described so far can not only be applied to Ba^+, but also to Ra^+, the heaviest of the earth-alkalies and isoelectronic to Ba^+. The extraction of $\sin^2\theta_W$ at sub % level accuracy will provide a sensitive means to extract physics beyond standard model, e.g. measuring the proton's weak charge [111], dark Z bosons [30, 29, 18].

7. Nederlandse Samenvatting

Uiterst nauwkeurige testen van de elektrozwakke theorie leggen sterke beperkingen op het Standaardmodel (SM) van deeltjesfysica. Atomaire pariteitsschending (Atomic Parity Violation, APV) maakt gebruik van een systeem met een lage energie en geeft toegang tot de menghoek van de zwakke kernkracht, $\sin^2\theta_W$, een fundamentele SM-parameter, bij lage impulsoverdracht. APV experimenten zijn gevoelig voor nieuwe natuurkunde bij energieën die momenteel niet kunnen worden bereikt door deeltjesversnellers. De APV-effecten worden versterkt in een zwaar atoom. Een onafhankelijke meting van de zwakke menghoek ($\sin^2\theta_W$) is ontworpen door het uitvoeren van experimenten met laser- en radiofrequente koeling- en vangtechnieken met barium en radium ionen. Dit maakt het mogelijk om het mijlpaalresultaat voor gemeten APV in atomair cesium te verbeteren met enkele ordes van grootte. Voor het meten van APV van een enkel ion wordt een techniek gebruikt dat een APV-spinrotatie produceert door de lichtverschuiving van de grondtoestand-Larmor-precessiefrequentie[46].

Essentieel voor een APV-meting is het begrip van de atomaire theorie tot op enkele procenten nauwkeurigheid. Dit hangt af van de nauwkeurigheid van de kennis van de atomaire structuur van het betreffende ion. Dit proefschrift bespreekt de essentiële ingrediënten voor atomaire golffunctieberekeningen, te weten de onderliggende lijnvorm, absolute overgangsfrequenties en isotoopverschuivingen in Ba^+.

Voor een lange meettijd en voor uitstekende controle van experimentele parameters moet het ion beter dan één optische golflengte worden gelokaliseerd. Daarvoor is een hyperbolische rf- Paul-val voor het vangen van Ba^+ ionen gebouwd en gemonteerd in een vacuümkamer met een gasdruk gehandhaafd onder een paar keer 10^{-11} mbar. Het dient als een voorloper van het iso-elektrische Ra^+ -ion. De Paul val ("val 1") bevat het isotoop $^{138}Ba^+$

en de val besproken in dit proefschrift ("val 2") is een aanpassing van "val 1ën bevat de twee verschillende isotopen $^{134}Ba^+$ en $^{136}Ba^+$ (Hoofdstuk 2). Op de val zijn acht extra elektroden gemonteerd om te compenseren voor de intern opgewekte elektrische strooivelden, die de val-levensduur van de gevangen ionen zouden verkorten. Een relatieve frequentie-stabiliteit van 10^{-11} wordt verkregen met het lasersysteem door gebruik te maken van hyperfijntransities in moleculair $^{127}I_2$ en een optische frequentiekam.

Het begrijpen van de onderliggende lijnvorm is belangrijk in precisie-experimenten, om de effecten van externe parameters te definiëren. Een lijnvorm-analyse van signalen van frequentie-gemoduleerde verzadigde absorptiespectroscopie van hyperfijne transities in moleculair $^{127}I_2$ als een frequentiereferentie wordt toegepast. Dit wordt gedaan om de absolute centrale frequenties te bepalen en om het effect van externe parameters op het signaal te begrijpen (Hoofdstuk 3). Een Voigt-functie wordt gebruikt om de lijnvorm te beschrijven. De centrale frequenties van de lijnen worden bepaald met een nauwkeurigheid van 10^{-11} na correctie van verschuiving door druk. De fitfunctie is geldig over een groot bereik van experimentele parameters, waaronder een dampdruk tussen 4 en 137 Pa. Overgebleven amplitudemodulatie van ongeveer 1%, die inherent is aan modulatiespectroscopie, veroorzaakt verschuivingen van de nuldoorgang van de dispersieve lijnvorm.

Overgangsfrequenties tussen laag-liggende energieniveaus in een enkel gevangen $^{138}Ba^+$ ion zijn gemeten met laserspectroscopie met een optische frequentiekam als referentie (Hoofdstuk 4). Een optisch Blochmodel met acht niveaus wordt gebruikt om de lijnvorm te beschrijven en om de frequenties van één- en twee-foton componenten van de lijnvorm te verkrijgen. Een lijnvorm berekend door het numeriek oplossen van de optische Bloch-vergelijkingen (OBE) met acht niveaus wordt gefit aan elk individueel spectrum. Intensiteit-afhankelijke lichtverschuivingseffecten die zijn inbegrepen in de optische Bloch-vergelijkingen vallen weg in de fitprocedure en de atomaire overgangsfrequentie wordt bepaald door de gefitte waarde te extrapoleren naar nul laserintensiteit. De overgangsfrequenties van de $6s\,^2S_{1/2} - 6p\,^2P_{1/2}$, $6s\,^2S_{1/2} - 5d\,^2D_{3/2}$, $6p\,^2P_{1/2} - 5d\,^2D_{3/2}$ transities in $^{138}Ba^+$ worden bepaald tot op sub-MHz precisie. Dit is een verbetering van meer dan een factor 100 ten opzichte van eerdere metin-

gen.

Een Fano-profiel wordt toegepast om de lijnvorm van gevangen $^{134}Ba^+$ en $^{136}Ba^+$ ionen te beschrijven om de overgangsfrequenties van de $6s\,^2S_{1/2}-6p\,^2P_{1/2}$, $6s\,^2S_{1/2}-5d\,^2D_{3/2}$, $6p\,^2P_{1/2}-5d\,^2D_{3/2}$ transities te bepalen (Hoofdstuk 5). Onder zekere condities is de stationaire oplossing van de OBE equivalent aan een Fano-profiel. Een verzameling van gesimuleerde data is verstrekt om hetzelfde te verifiëren. Het Fano-profiel beschrijft de twee interferentiepaden, de excitatie van de S-P transitie door een foton van het laserveld bij ν_1 en het driestap-proces via een virtuele tussenliggende toestand om bij de eindtoestand te komen, welke de spontane emissie van een foton uit de P staat is. Deze benadering geeft een fysische interpretatie van de Raman resonantieconditie die het mogelijk maakt om de lichtverschuiving als gevolg van de koppeling van de energieniveaus met de fotonen te verkrijgen.

De bepaling van overgangsfrequenties voor de drie isotopen $^{138}Ba^+$, $^{134}Ba^+$ and $^{136}Ba^+$ geeft toegang tot de isotoopverschuiving in Ba^+. Isotoopverschuivingen (IS) zijn ideale instrumenten voor de atomaire golffuncties op de positie van de kern en experimentele IS data kan gebruikt worden om de precieze theoretische voorspellingen te testen. Bovendien kunnen de atomaire berekeningen worden verbeterd door het vergelijken van zeer nauwkeurige APV metingen van een aantal isotopen van hetzelfde element, doordat hierbij de atomaire structuuronzekerheden wegvallen. De geldigheid van de berekende atoomstructuur, in het bijzonder de golffuncties, is cruciaal voor metingen van atomaire systemen. Levensduurmetingen geven transitiematrix-elementen. Continue kwantumsprong-spectroscopie wordt toegepast en de levensduur van het lang-levende $5d^2D_{5/2}$ niveau in $^{138}Ba^+$ ionen wordt gemeten in gevangen enkele ionen en kleine ionenkristallen [110, 61] (zie Fig 7.1).

Experimentele parameters die zouden kunnen hebben leiden tot systematische effecten zijn onderzocht. De gevonden levensduur is $\tau_{D_{5/2}} = 25.6(0.5)$s, wat significant kleiner is dan eerder gerapporteerde waarden (zie see Fig 7.2). Dit bevat een correctie voor de statistisch significante contributie aan de vervalsnelheid van afschrikking (quenching) veroorzaakt door achtergrond-gasbotsingen, een kleine correctie voor zwarte-lichaamstraling, en een kleine correctie voor bias geïntroduceerd in de analyseprocedure.

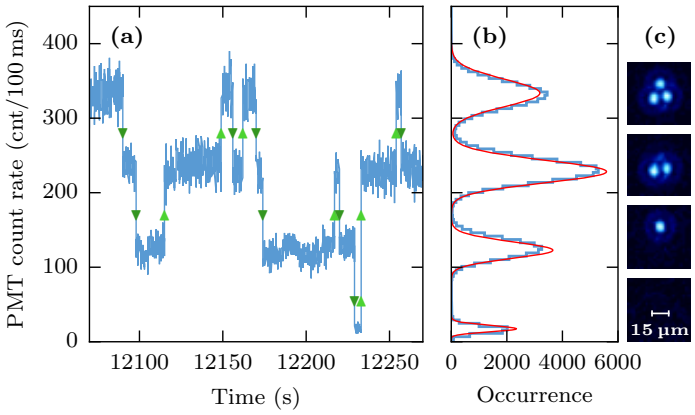

Figuur 7.1.: Voorbeeld van een kwantumspong van een kristal van drie Ba^+-ions. (a) Data verzameld gedurende 3 minuten van fluorescentie bij 494 nm. Pijlen geven het passeren van grenzen gezet in de analyse aan. (b) Een projectie van de telsnelheid bij een 100 ms tijdresolutie gefit met een model gebaseerd op Poisson-statistiek om de grenswaarden te bepalen. (c) Een voorbeeld van EMCCD afbeeldingen van het ionenkristal. (Aangepast van [110])

.

De systematische effecten van een APV-experiment vragen om een uitgebreide en zorgvuldige studie. Afwijkingen van relevante experimentele parameters, zoals polarisatie van lichtvelden en ionlocatie, zouden systematische niveauverschuivingen kunnen veroorzaken die lijken op pariteitschendende lichtverschuiving.

Een methode is nodig om op-resonante, pariteitschendende vectorlichtverschuiving in de $6S_{1/2}$ toestand van Ba^+ met de toepassing van staande golven met 2050 nm licht (zie Fig 1.12) te meten. Vacuümcompatibele trilholtes met een hoge finesse, om deze staande golven te produceren en besturen, zijn in voorbereiding. Dit experiment heeft ook goede vooruitzichten voor een enkele-ionklok met een potentiële relatieve nauwkeurigheid van 10^{-18}. De lange-termijndrift in de klokfrequentie, wanneer de atomaire energieverschuivingen eenmaal onder controle zijn, kan worden geïnterpreteerd als temporele variaties in de fundamentele constanten van de natuur

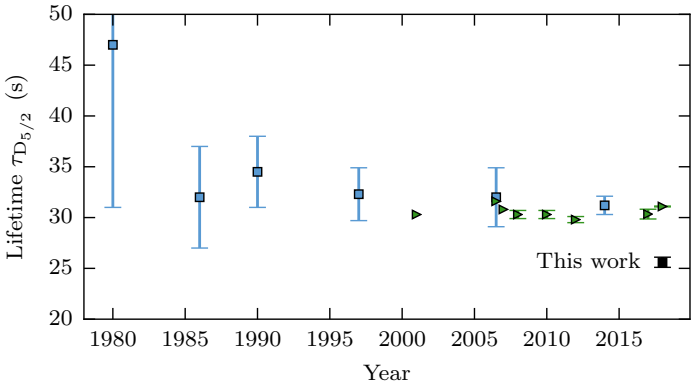

Figuur 7.2.: Geschiedenis van metingen (■) en berekeningen (►) van de levensduur van het $5d^2D_{5/2}$-niveau in Ba [110]

zelf. Alle tot zover beschreven aspecten van de APV meting kunnen niet alleen worden toegepast op Ba^+, maar ook op Ra^+, de zwaarste van de aard-alkaliën en iso-elektrisch aan Ba^+. De bepaling van $\sin^2\theta_W$ op sub-% nauwkeurigheid zal een nauwkeurige manier geven om nieuwe natuurkunde te vinden, bijvoorbeeld het meten van de zwakke menghoek van het proton [111], donkere Z bosonen [30, 29, 18].

8. Acknowledgment

This work is part of a research program 'Broken Mirrors and Drifting Constants' funded in part by the Stichting voor Fundamenteel Onderzoek der Materie (FOM), which is financially supported by the Nederlandse Organisatie voor Wetenschappelijk Onderzoek (NWO) and carried out at Van Swinderen Institute for Particle Physics and Gravity (VSI), University of Groningen. The research included in this dissertation could not have been performed if not for the assistance, patience, and support of many individuals.

I owe sincere thanks to my supervisors Klaus Jungmann and Lorenz Willmann for their guidance and support through out this project. With the many hours spent in the lab, even late nights for collecting data I feel truly lucky to have them as my mentors. Klaus, thank you for reminding me to put a smile on my face everyday. Many thanks to you for the patient and careful inspection of my manuscript multiple times. Lorenz, thank you for putting me on the right path whenever I got derailed and for your many insights and immense help towards the completion of this work. I would also like to thank my assessment committee members Prof. R. A. Hoekstra, Prof. P. van der Straten and Prof. K.Wendt for their thorough review, valuable comments and corrections. I would like to acknowledge Gerco Onderwater for his support and advice. Gerco, thank you for your time and effort for helping me with data analysis with which I could successfully finish my thesis. I express my sincere gratitude to the other senior staff of the FIS group, Steven Hoekstra, Hans Wilschut, Rob Timmermans and Anastasia Borschevsky for their work in the group and advice.

I am thankful for the technical support from Leo Huisman and Oliver Böll. I have learned a lot from you both. Leo, thank you for all the kindness and care you have shown to me either work related or otherwise.

Oli, thanks for always being there to share a good laugh and to prank each other. I am grateful to Hilde van der Meer for all the administrative work done for me from the day I joined the group. Hilde, you are such a nice person to talk to and a wonderful listener as well. Thank you for the very thoughtful sent-off gift you got me. I would also like to thank the mechanical and electrical workshop of KVI-CART for all their assistance in building the experimental set up.

I have to thank my colleagues Amita, Elwin, Artem, Kevin, Parul, Mina, Auke, Bai, Corine, Joost, Mayerlin, Sreekanth, Thomas and Olivier for any scientific advice, assistance and all the fun time we had together. Special thanks to Auke for his patience and long hours spent for helping me in making the 'Nederlandse Samenvatting' and to Thomas for proof reading it and correcting.

Next I would like to thank my support system in the Netherlands whom I consider as family, Abdu, Bahjoos, Josin, Honey, Jyothsna, Justin, Prashob, Sunitha, Sijeesh, Reeja, Babitha, Sibi, Arun, Dhanya, Jaison, Mariamma, Sheena, Salin, Guna, Elizabeth, Noby, Neethu, Motty, Dibin, Krishna, Sneha, Sruthy and all the kids. I am thankful to the people who have supported me and stayed with me through thick and thin, John, Shyama, Anoop, Dhanoj, Anandu, Joseph, Aarthi, Sarrvesh, Raveen, Ketan, Kavya, Prachi, Hemanth, Eswar, Gowtham, Sandeep, Aneesh. I thank my dear friends Amala, Ann, Ritika, Merlin, Sreeju, Eddy, Alka, Neethu, Nayana, Sumesh, Arjun, Shyam, Sanu, Naina, Priyanka, Gowtham, Uma, Sree, Amrith, Sujina, Swetha for always being there for me and for all the support and encouragement.

I am utterly grateful to my teacher and mentor Suman Sir without whom I wouldn't be able to achieve any of this. Thank you for believing in me and guiding me to the right path. Thank you Veena aunty for your constant support. I am very thankful to my husband Pius for being very understanding, caring and tolerating with all my tantrums during some of the hectic days. Finally I would like to thank my family, my father- Raveendran, mother-Vineetha, brother-Navjot, my father in-law-Augustine, mother in-law- Elezabath, Amrutha chechi and Sam chettan for their love, affection, support and encouragement.

List of Symbols

Table .1.: Laser and frequency related symbols employed in this text

Symbol	Description
λ_{494}	Wavelength of laser light at 494 nm
λ_{650}	Detuning of laser light at 650 nm
δ_{494}	Detuning of laser light at 494 nm
δ_{650}	Detuning of laser light at 650 nm
ν_s	Switching frequency
$\nu^1_{AOM-650}$	AOM frequency for spectroscopy with laser light at λ_{650}
$\nu^2_{AOM-650}$	AOM frequency for cooling the ion for laser light at λ_{650}
$\nu^1_{AOM-494}$	AOM frequency for spectroscopy with laser light at λ_{494}
$\nu^2_{AOM-494}$	AOM frequency for cooling the ion for laser light at λ_{494}
P_{494}	Power of light at λ_{494}
P_{650}	Power of light at λ_{650}
I_{494}	Intensity of light at λ_{494}
m	Mode number
ν_m	Frequency of each mode of the frequency comb
$\nu_{comb,reprate}$	Comb repetition rate
$\nu_{comb,synth}$	Synthesizer frequency
$\nu_{comb,offset}$	Carrier-envelop offset frequency
ν_{diode}	Absolute frequency of diode laser
ν_{dye}	Absolute frequency of dye laser light
ν'_{B_2}	Beatnote frequency: light from diode laser with light from the dye laser
ν_{B_1}	Beatnote frequency: light from TiSa laser and frequency comb light
ν_1	Frequency of the light in the trap at wavelength λ_{494}
ν_2	Frequency of the light in the trap at wavelength λ_{650}

A. Dimensions of various trap parts

In this chapter we collect the mechanical specifications of the new small trap (trap 2) constructed within the framework of this thesis (see Chapter 2).

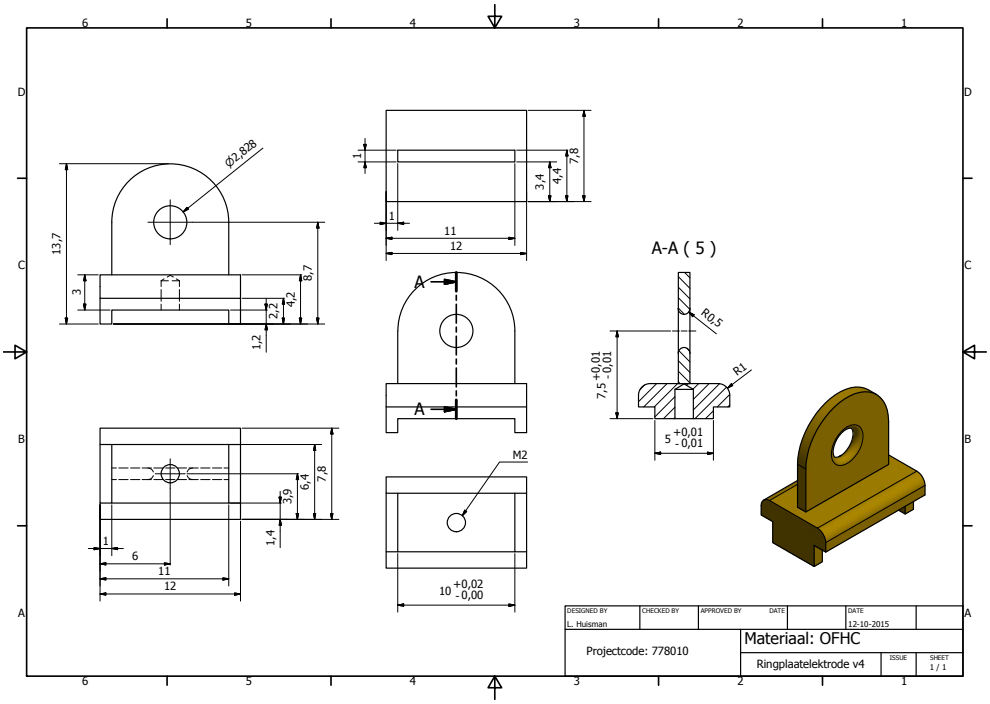

Figure A.1.: Center ring electrode.

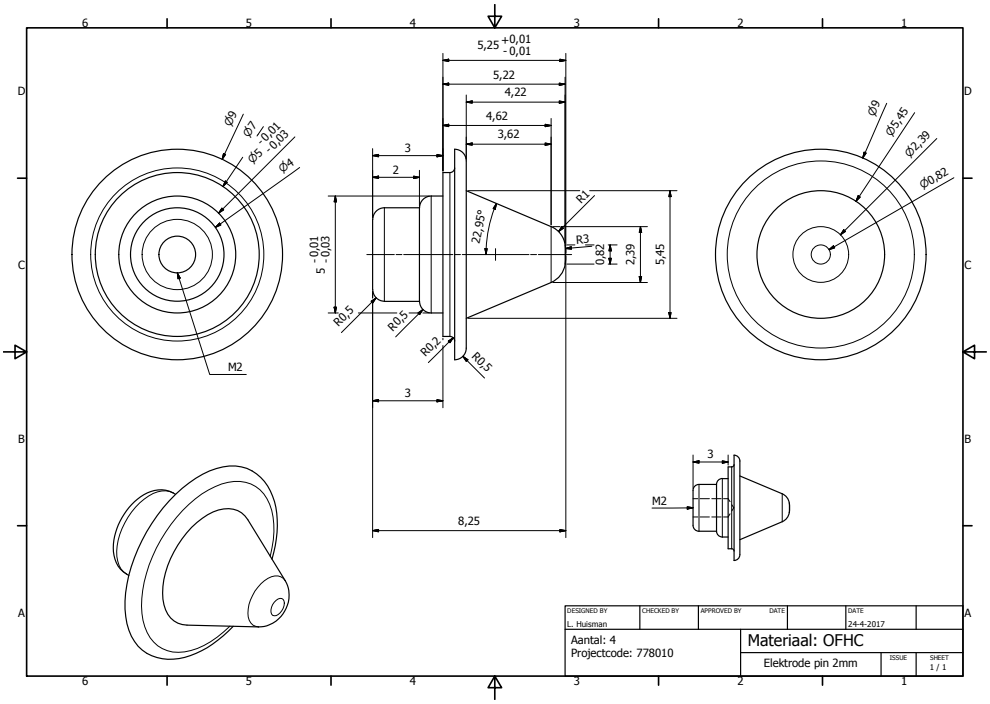

Figure A.2.: End cap electrodel.

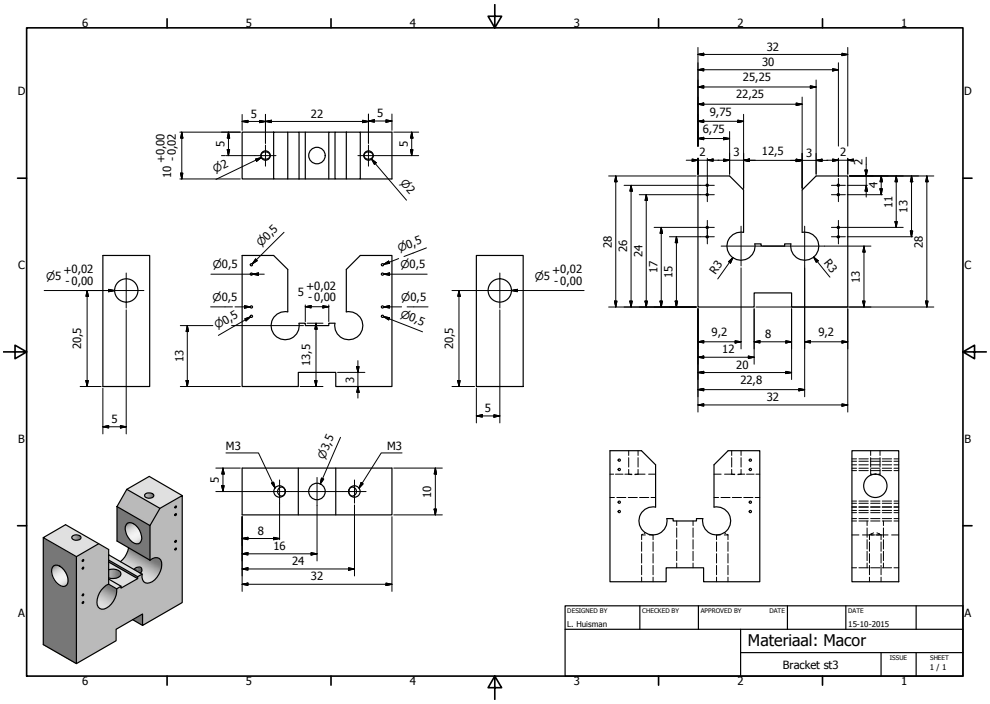

Figure A.3.: Macor.

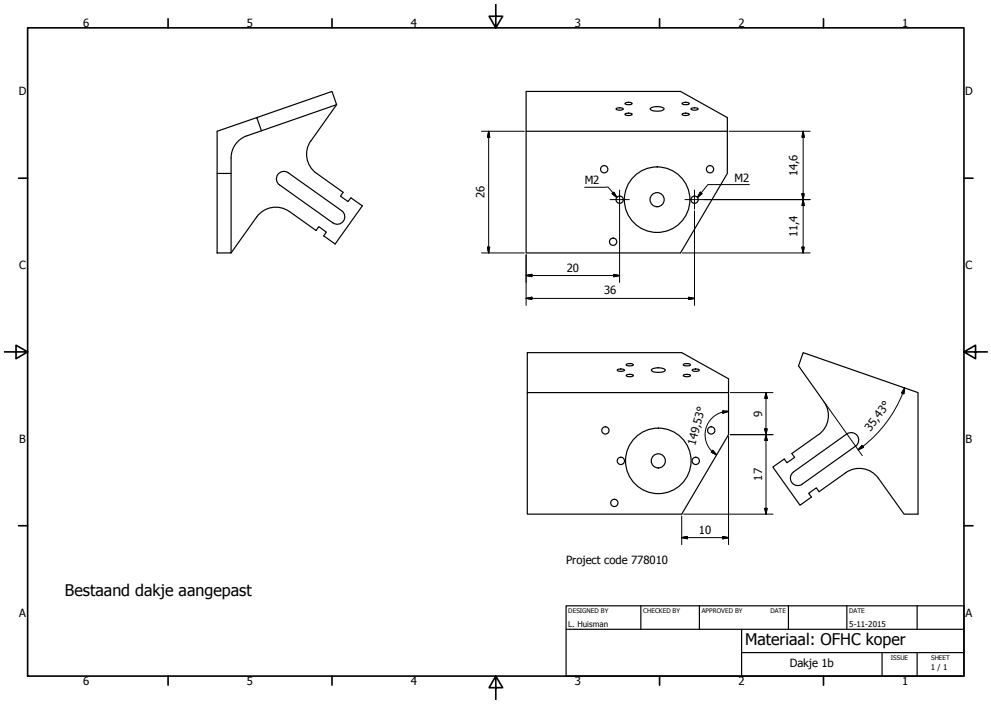

Figure A.4.: Oven holderl.

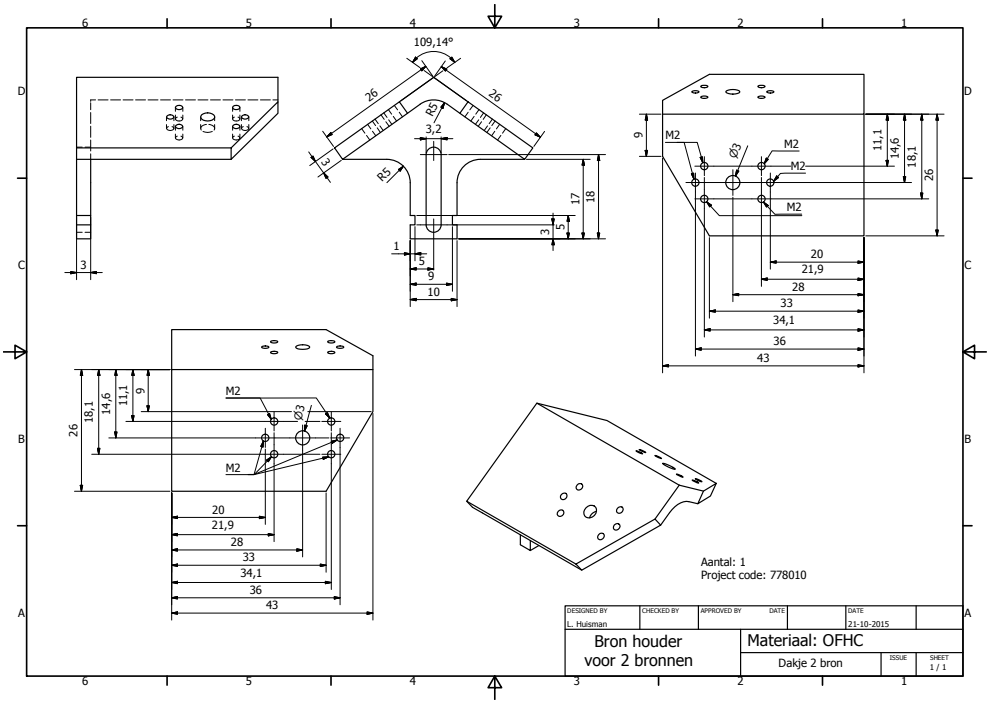

Figure A.5.: Oven holder.

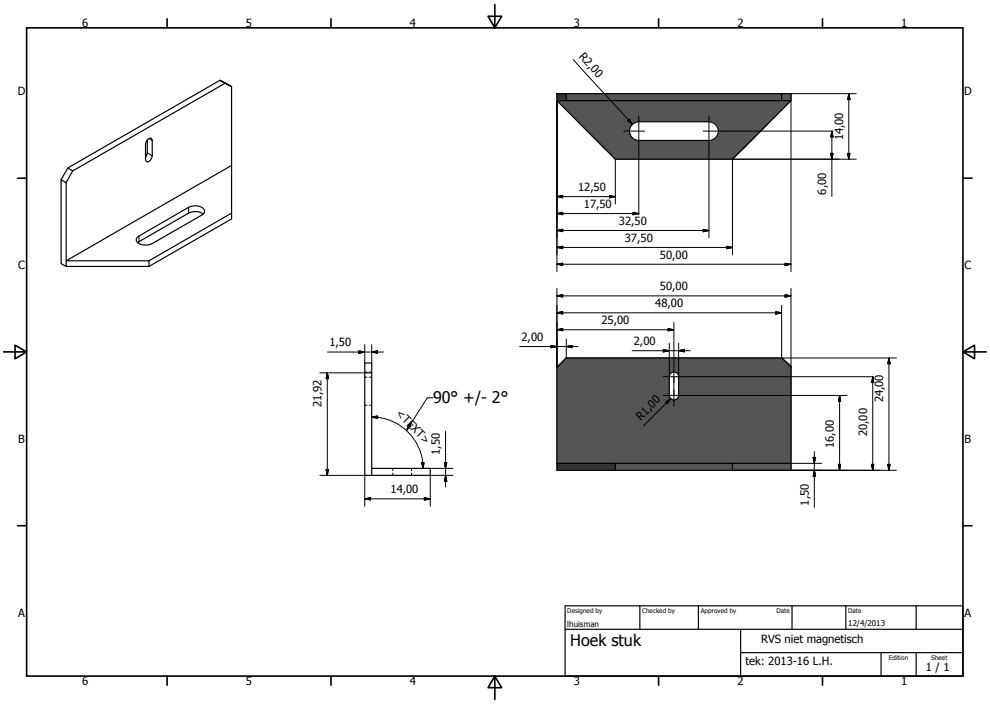

Figure A.6.: Slit aperture.

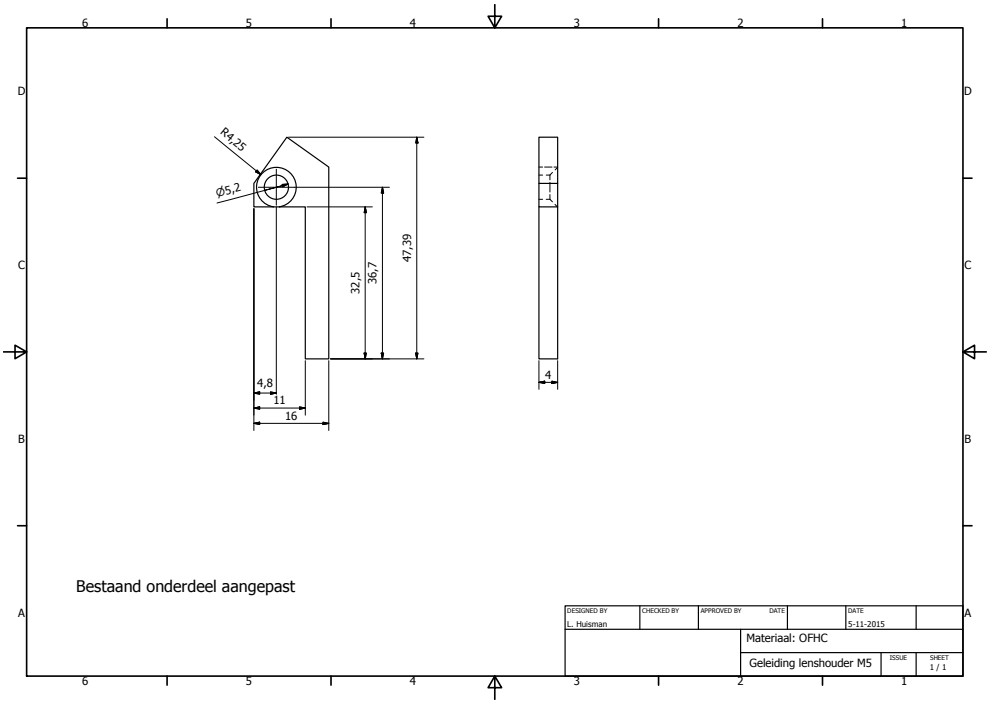

Figure A.7.: 'Hockey stick' holder for lens holder and aperuture.

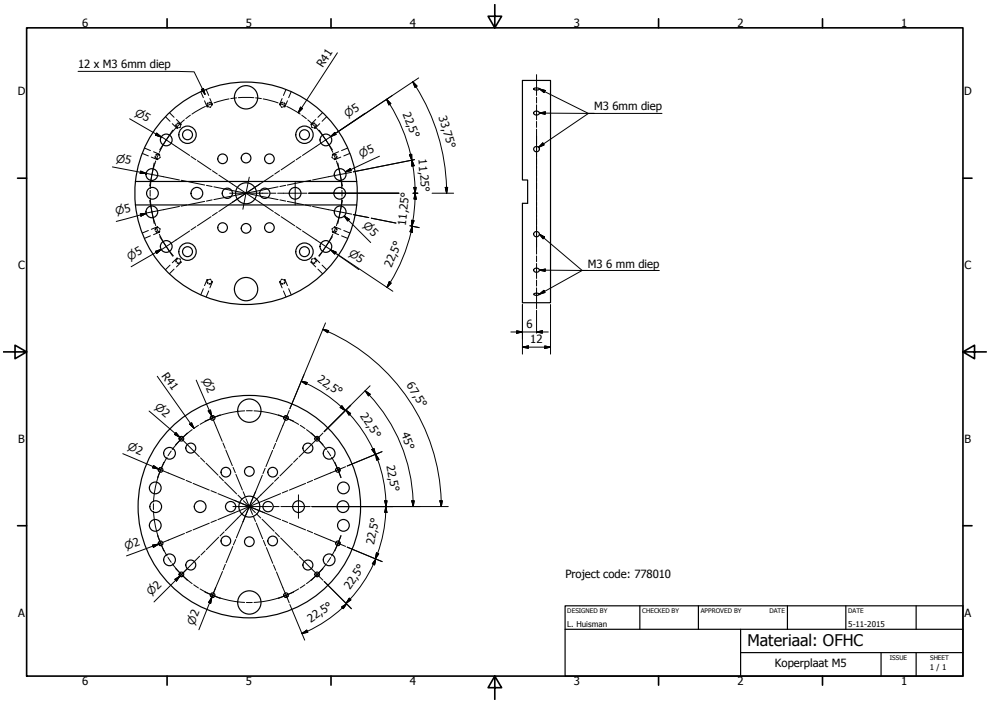

Figure A.8.: Cu base plate.

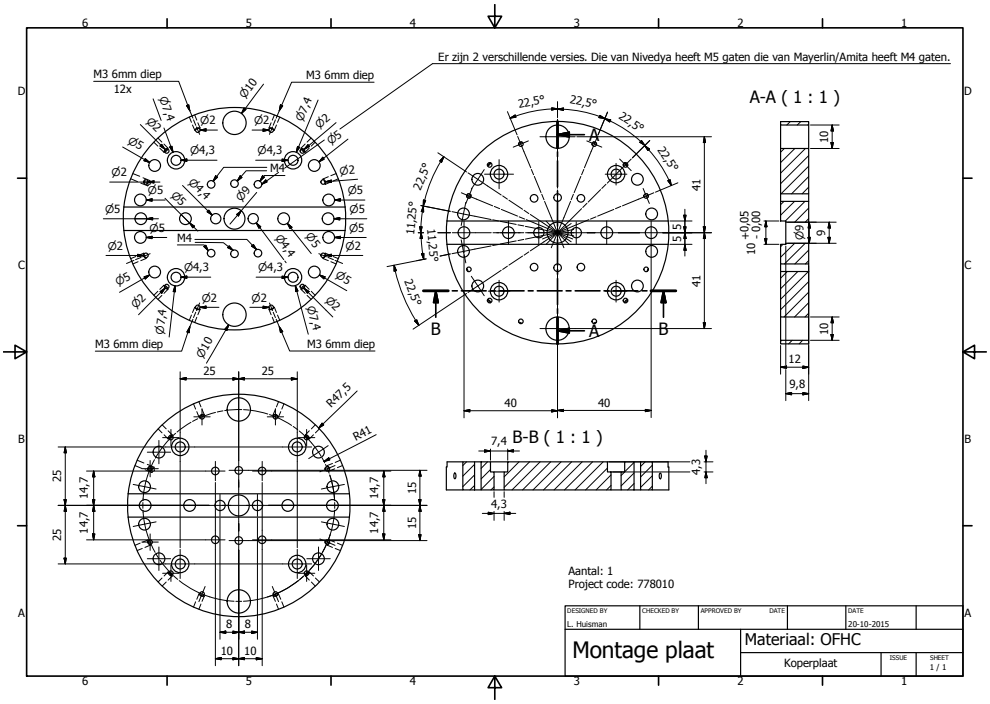

Figure A.9.: Cu base plate.

B. Schematics of dc-distribution box

Schematics of a high precision stable voltage distribution for biasing the correction electrodes (see Chapter 2).

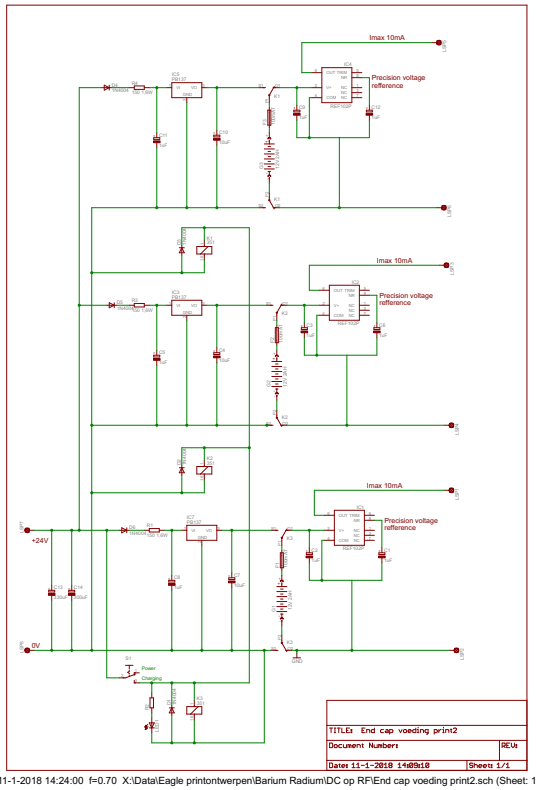

Figure B.1.: DC box for end caps.

C. Experimental parameters

Listing of the part of the experimental data which is discussed and analyzed in this thesis. The data files are organized by the sate of the data taking. A particular scan is referred by the time stamp in the data file. Additional parameters from the logbook are also given in the tables.

Table C.1.: Parameters to obtain the spectra of $5d\,^2D_{3/2}$ – $6p\,^2P_{1/2}$ transition for different switching frequencies. Data from 01 November 2017.

Start time (forward) [s]	Start time (backward) [s]	End time (backward) [s]	ν_s [kHz]	Blue Power [µW]	Red Power [µW]	$\nu_{comb,synth}$ -2e7 [Hz]	ν_{AOM,I_2} [MHz]	$\nu_{AOM,650}$ [MHz]	Number of Ions
30740	30856	30940	53.013	1.98	1.02	1325	72.47	352	20
31390	31490	31590	23.013	1.98	1.02	1325	72.47	352	20
31540	31642	31745	13.013	1.98	1.02	1325	72.47	352	20
31785	31888	31992	6.013	1.98	1.02	1325	72.47	352	20

Table C.2.: Parameters to determine saturation intensity. Data from 28 August 2017.

Start time [s]	End time [s]	Blue Power [µW]	Red Power [µW]	$\nu_{comb,synth}$ -2e7 [Hz]	ν_{AOM,I_2} [MHz]	ν_s [kHz]	$\nu_{AOM,650}$ [MHz]	Number of Ions
26730	26935	27.8	17	1325	72.47	53.013	352	6
27090	27295	16.1	17	1325	72.47	53.013	352	6
27370	27580	8.5	17	1325	72.47	53.013	352	6
29270	29500	5.4	17	1325	72.47	53.013	352	5
28225	28440	2.7	17	1325	72.47	53.013	352	5
28500	28720	1.3	17	1325	72.47	53.013	352	5
28740	28950	0.5	17	1325	72.47	53.013	352	5
28960	29190	0.26	17	1325	72.47	53.013	352	5

Table C.3.: Parameters for spectra recorded for different number of ions. Data from 28 August 2017.

Start time [s]	End time [s]	Blue Power [µW]	Red Power [µW]	$\nu_{comb,synth}$ -2e7 [Hz]	ν_{AOM,I_2} [MHz]	ν_s [kHz]	$\nu_{AOM,650}$ [MHz]	Number of Ions
27670	27878	5.4	17	1325	72.47	53.013	352	6
29270	29500	5.4	17	1325	72.47	53.013	352	5
33620	33730	5.4	17	1325	72.47	53.013	352	1

Table C.4.: Parameters for spectra recorded with $^{134}Ba^+$ for different detuning δ_{494}. Data from 07 September 2017.

Start time [s]	End time [s]	Blue Power [µW]	Red Power [µW]	$\nu_{comb,synth}$ -2e7 [Hz]	ν_{AOM,I_2} [MHz]	ν_s [kHz]	$\nu_{AOM,650}$ [MHz]	Number of Ions
28650	29150	8.6	19	1315	72.47	53.013	352	3
29420	29620	8.6	19	1320	72.47	53.013	352	3
29700	29920	8.6	19	1325	72.47	53.013	352	3
29930	30140	8.6	19	1330	72.47	53.013	352	3
30150	30350	8.6	19	1335	72.47	53.013	352	3

Table C.5.: Parameters for spectra recorded with $^{134}Ba^+$ for different powers P_{494} at $\nu_{AOM,650}$=362 MHz. Data from 02 November 2017.

Start time [s]	End time [s]	Blue Power [µW]	Red Power [µW]	$\nu_{comb,synth}$ -2e7 [Hz]	ν_{AOM,I_2} [MHz]	ν_s [kHz]	$\nu_{AOM,650}$ [MHz]	Number of Ions
19040	19250	12.60	6.5	1332	72.47	6.013	362	10
19300	19510	1.98	6.5	1332	72.47	6.013	362	10
19540	19740	0.79	6.5	1332	72.47	6.013	362	10
19760	19970	0.31	6.5	1332	7 2.47	6.013	362	10

Table C.6.: Parameters for spectra recorded with $^{134}Ba^{+}$ for different powers P_{494} at $\nu_{AOM,650}$=362 MHz. Data from 30 October 2017.

Start time [s]	End time [s]	Blue Power [µW]	Red Power [µW]	$\nu_{comb,synth}$ -2e7 [Hz]	ν_{AOM,I_2} [MHz]	ν_s [kHz]	$\nu_{AOM,650}$ [MHz]	Number of Ions
29570	29770	0.88	16.38	1345	72.49	53.013	362	5
29780	29990	0.55	16.38	1345	72.49	53.013	362	5
30030	30230	0.35	16.38	1345	72.49	53.013	362	5
30300	30500	3.50	16.38	1345	72.49	53.013	362	5
30640	30850	5.56	16.38	1345	72.49	53.013	362	5

Table C.7.: Parameters for spectra recorded with $^{134}Ba^{+}$ for different powers P_{494} at $\nu_{AOM,650}$=352 MHz. Data from 28 September 2017.

Start time [s]	End time [s]	Blue Power [µW]	Red Power [µW]	$\nu_{comb,synth}$ -2e7 [Hz]	ν_{AOM,I_2} [MHz]	ν_s [kHz]	$\nu_{AOM,650}$ [MHz]	Number of Ions
8450	8650	0.88	16.38	1345	72.49	53.013	352	5
8680	8880	0.55	16.38	1345	72.49	53.013	352	5
9470	94670	0.35	16.38	1345	72.49	53.013	352	5

Table C.8.: Parameters for spectra recorded with $^{134}Ba^{+}$ for different powers P_{650}. Data from 02 November 2017.

Start time [s]	End time [s]	Blue Power [µW]	Red Power [µW]	$\nu_{comb,synth}$ -2e7 [Hz]	ν_{AOM,I_2} [MHz]	ν_s [kHz]	$\nu_{AOM,650}$ [MHz]	Number of Ions
21200	21400	1.98	1.02	1332	72.47	6.013	362	10
21440	21645	1.98	2.58	1332	72.47	6.013	362	10
21900	22100	1.98	65.52	1332	72.47	6.013	362	10
21680	21890	1.98	6.50	1332	72.47	6.013	362	10

Table C.9.: Parameters for spectra recorded with $^{136}Ba^{+}$ for different powers P_{494}. Data from 27 September 2017.

Start time [s]	End time [s]	Blue Power [µW]	Red Power [µW]	$\nu_{comb,synth}$ -2e7 [Hz]	ν_{AOM,I_2} [MHz]	ν_s [kHz]	$\nu_{AOM,650}$ [MHz]	Number of Ions
26410	26630	8.6	19	1255	72.45	53.013	352	1
26640	26850	8.6	19	1255	72.45	53.013	352	1
26860	27060	8.6	19	1255	72.45	53.013	352	1

Bibliography

[1] Sheldon L. Glashow. Partial-symmetries of weak interactions. *Nuclear Physics*, 22(4):579–588, 1961.

[2] Steven Weinberg. A model of leptons. *Phys. Rev. Lett.*, 19:1264–1266, Nov 1967.

[3] Mary K. Gaillard, Paul D. Grannis, and Frank J. Sciulli. The standard model of particle physics. *Rev. Mod. Phys.*, 71(2):S96–S111, March 1999.

[4] S. Chatrchyan et al. Observation of a new boson at a mass of 125 GeV with the CMS experiment at the LHC. *Physics Letters B*, 716(1):30–61, September 2012.

[5] ATLAS Collaboration. Observation of a new particle in the search for the Standard Model Higgs boson with the ATLAS detector at the LHC. *Physics Letters B*, 716(1):1–29, 2012.

[6] Wikimedia Commons. File:standard model of elementary particles.svg — wikimedia commons, the free media repository, 2017.

[7] Jens Erler and Michael J. Ramsey-Musolf. Weak mixing angle at low energies. *Phys. Rev. D*, 72(7):073003, October 2005.

[8] T. D. Lee. Particle Physics and Introduction to Field Theory. *Contemp. Concepts Phys.*, 1:1–865, 1981.

[9] A. Sirlin. Radiative corrections in the $\mathrm{SU}(2)_L \times \mathrm{U}(1)$ theory: A simple renormalization framework. *Phys. Rev. D*, 22:971–981, Aug 1980.

[10] J G Ena, M Lintz, and M.-A Bouchiat. Atomic parity violation: Principles, recent results, present motivations. *Modern Physics Letters A*, 20(6):375–389, 2005.

[11] S.J Pollock and M.C Welliver. Effects of neutron spatial distributions on atomic parity nonconservation in cesium. *Physics Letters B*, 464(3):177 – 182, 1999.

[12] M.J. Musolf, T.W. Donnelly, J. Dubach, S.J. Pollock, S. Kowalski, and E.J. Beise. Intermediate-energy semileptonic probes of the hadronic neutral current. *Physics Reports*, 239(1):1 – 178, 1994.

[13] Jens Erler, Andriy Kurylov, and Michael J. Ramsey-Musolf. Weak charge of the proton and new physics. *Phys. Rev. D*, 68(1):016006, July 2003.

[14] S. G. Porsev, K. Beloy, and A. Derevianko. Precision determination of electroweak coupling from atomic parity violation and implications for particle physics. *Phys. Rev. Lett.*, 102(18):181601, May 2009.

[15] Precision electroweak measurements on the z resonance. *Physics Reports*, 427(5):257 – 454, 2006.

[16] S. L. A. C. E158 Collaboration, P. L. Anthony, et al. Precision measurement of the weak mixing angle in møller scattering. *Phys. Rev. Lett.*, 95(8):081601, August 2005.

[17] G. P. Zeller et al. Precise Determination of Electroweak Parameters in Neutrino-Nucleon Scattering. *Physical Review Letters*, 88(9):4, 2002.

[18] Hooman Davoudiasl and William J. Marciano. Running of the $u(1)$ coupling in the dark sector. *Phys. Rev. D*, 92:035008, Aug 2015.

[19] Hooman Davoudiasl. Nucleon decay into a dark sector. *Phys. Rev. Lett.*, 114(5):051802, February 2015.

[20] C. S. Wood, S. C. Bennett, D. Cho, B. P. Masterson, J. L. Roberts, C. E. Tanner, and C. E. Wieman. Measurement of parity nonconservation and an anapole moment in cesium. *Science*, 275(5307):1759–1763, 3 1997.

[21] S. C. Bennett and C. E. Wieman. Measurement of the 6S-7S transition polarizability in atomic cesium and an improved test of the standard model. *Physical Review Letters*, 82(12):2484–2487, 1999.

[22] S. G. Porsev, K. Beloy, and A. Derevianko. Precision determination of weak charge of ^{133}Cs from atomic parity violation. *Phys. Rev. D*, 82(3):036008, August 2010.

[23] V. A. Dzuba, J. C. Berengut, V. V. Flambaum, and B. Roberts. Revisiting parity nonconservation in cesium. *Phys. Rev. Lett.*, 109(20):203003, November 2012.

[24] V. M. Shabaev, K. Pachucki, I. I. Tupitsyn, and V. A. Yerokhin. Qed corrections to the parity-nonconserving $6s-7s$ amplitude in ^{133}Cs. *Phys. Rev. Lett.*, 94(21):213002, June 2005.

[25] M. A. Bouchiat, J. Guena, L. Pottier, and L. Hunter. New observation of a parity violation in cesium. *Physics Letters B*, 134(6):463–468, 1984.

[26] M. C. Noecker, B. P. Masterson, and C. E. Wieman. Precision Measurement of parity nonconservation in atomic cesium: A low-energy test of the electroweak theory. *Physical Review Letters*, 61(3):310–313, 1988.

[27] Paul Langacker, Mingxing Luo, and Alfred K. Mann. High-precision electroweak experiments: A global search for new physics beyond the standard model. *Rev. Mod. Phys.*, 64:87–192, Jan 1992.

[28] Gouri Shankar Giri. *Radium Ion Spectroscopy: Towards Atomic Parity Violation in a single trapped ion.* PhD thesis, University of Groningen, 10 2011. Relation: https://www.rug.nl/ Rights: University of Groningen.

[29] Heman Gharibnejad and Andrei Derevianko. Dark forces and atomic electric dipole moments. *Phys. Rev. D*, 91(3):035007, February 2015.

[30] Hooman Davoudiasl, Hye-Sung Lee, and William J. Marciano. Muon $g-2$, rare kaon decays, and parity violation from dark bosons. *Phys. Rev. D*, 89(9):095006, May 2014.

[31] C. S. Wu, E. Ambler, R. W. Hayward, D. D. Hoppes, and R. P. Hudson. Experimental test of parity conservation in beta decay. *Phys. Rev.*, 105:1413–1415, Feb 1957.

[32] M. A. Bouchiat and C. C. Bouchiat. Weak neutral currents in atomic physics. *Physics Letters B*, 48(2):111–114, 1974.

[33] G. Gwinner, E. Gomez, L. A. Orozco, A. Perez Galvan, D. Sheng, Y. Zhao, G. D. Sprouse, J. A. Behr, K. P. Jackson, M. R. Pearson, S. Aubin, and V. V. Flambaum. Fundamental symmetries studies with cold trapped francium atoms at isac. *Hyperfine Interactions*, 172(1):45–51, Sep 2006.

[34] G. Stancari, S. N. Atutov, R. Calabrese, L. Corradi, A. Dainelli, C. de Mauro, A. Khanbekyan, E. Mariotti, P. Minguzzi, L. Moi, S. Sanguinetti, L. Tomassetti, and S. Veronesi. Francium sources and traps for fundamental interaction studies. *The European Physical Journal Special Topics*, 150(1):389–392, Nov 2007.

[35] J. A. Sherman, A. Andalkar, W. Nagourney, and E. N. Fortson. Measurement of light shifts at two off-resonant wavelengths in a single trapped Ba^+ ion and the determination of atomic dipole matrix elements. *Phys. Rev. A*, 78:052514, Nov 2008.

[36] L. W. Wansbeek, B. K. Sahoo, R. G. E. Timmermans, K. Jungmann, B. P. Das, and D. Mukherjee. Atomic parity nonconservation in Ra^+. *Phys. Rev. A*, 78:050501, Nov 2008.

[37] B. K. Sahoo, L. W. Wansbeek, K. Jungmann, and R. G. E. Timmermans. Light shifts and electric dipole matrix elements in Ba^+ and Ra^+. *Phys. Rev. A*, 79:052512, May 2009.

[38] Klaus Peter Jungmann. Tests of fundamental symmetries and interactions - using nuclei and lasers. In *Hyperfine Interactions*, volume 171, pages 41–55, 2006.

[39] L. W. Wansbeek. *Atomic Parity Violation in a Single Radium Ion.* PhD thesis, University of Groningen, 2011.

[40] D. M. Meekhof, P. Vetter, P. K. Majumder, S. K. Lamoreaux, and E. N. Fortson. High-precision measurement of parity nonconserving optical rotation in atomic lead. *Physical Review Letters*, 71(21):3442–3445, 1993.

[41] P. A. Vetter, D. M. Meekhof, P. K. Majumder, S. K. Lamoreaux, and E. N. Fortson. Precise test of electroweak theory from a new measurement of parity nonconservation in atomic thallium. *Physical Review Letters*, 74(14):2658–2661, 1995.

[42] M. J D MacPherson, K. P. Zetie, R. B. Warrington, D. N. Stacey, and J. P. Hoare. Precise measurement of parity nonconserving optical rotation at 876 nm in atomic bismuth. *Physical Review Letters*, 67(20):2784–2787, 1991.

[43] P. K. Majumder and L. L. Tsai. Measurement of the electric quadrupole amplitude within the 1283-nm $6P_{1/2}$-$6P_{3/2}$ transition in atomic thallium. *Physical Review A*, 60(1):267, 1999.

[44] C. S. Wood, S. C. Bennett, D. Cho, B. P. Masterson, J. L. Roberts, C. E. Tanner, and C. E. Wieman. Measurement of parity nonconservation and an anapole moment in cesium. *Science*, 275(5307):1759–1763, 1997.

[45] K. Tsigutkin, D. Dounas-Frazer, A. Family, J. E. Stalnaker, V. V. Yashchuk, and D. Budker. Observation of a large atomic parity violation effect in ytterbium. *Phys. Rev. Lett.*, 103(7):071601, August 2009.

[46] Norval Fortson. Possibility of measuring parity nonconservation with a single trapped atomic ion. *Phys. Rev. Lett.*, 70(16):2383–2386, Apr 1993.

[47] T. W. Koerber, M. Schacht, W. Nagourney, and E. N. Fortson. Radio frequency spectroscopy with a trapped Ba^+ ion: Recent progress and prospects for measuring parity violation. *Journal of Physics B: Atomic, Molecular and Optical Physics*, 36(3):637–648, 2003.

[48] M. Nuñez Portela. *Single ion spectroscopy in preparation of an atomic parity violation measurement in* Ra^+. $PhDthesis, University of Groningen$, 2015.

[49] V. A. Dzuba, V. V. Flambaum, and J. S. M. Ginges. Calculations of parity-nonconserving s-d amplitudes in Cs, Fr, Ba^+ and Ra^+. *Phys. Rev. A*, 63:062101, May 2001.

[50] W. H. King. Comments on the article "peculiarities of the isotope shift in the samarium spectrum". *J. Opt. Soc. Am.*, 53(5):638–639, May 1963.

[51] W.H. King. *Isotope Shifts in Atomic Spectra*, volume 1. Springer US, 1984.

[52] K. M. Lynch et al. Laser-spectroscopy studies of the nuclear structure of neutron-rich radium. *Phys. Rev. C*, 97(2):024309, February 2018.

[53] M. S. Safronova and W. R. Johnson. All-Order Methods for Relativistic Atomic Structure Calculations, 2008.

[54] Julian C. Berengut, Dmitry Budker, Cic Delaunay, Victor V. Flambaum, Claudia Frugiuele, Elina Fuchs, Christophe Grojean, Roni Harnik, Roee Ozeri, Gilad Perez, and Yotam Soreq. Probing new long-range interactions by isotope shift spectroscopy. *Phys. Rev. Lett.*, 120(9):091801, February 2018.

[55] Masao Takamoto and Hidetoshi Katori. Spectroscopy of the $^1s_0 - ^3p_0$ clock transition of ^{87}Sr in an optical lattice. *Phys. Rev. Lett.*, 91:223001, Nov 2003.

[56] Hidetoshi Katori, Masao Takamoto, V. G. Pal'chikov, and V. D. Ovsiannikov. Ultrastable optical clock with neutral atoms in an engineered light shift trap. *Phys. Rev. Lett.*, 91:173005, Oct 2003.

[57] J. A. Sherman. *Single Barium Ion Spectroscopy: Light Shifts, Hyperfine Structure, and Progress on an Optical Frequency Standard and Atomic Parity Violation*. PhD thesis, University of Washington, 2007.

[58] N. L. Manakov, V. D. Ovsiannikov, and L. P. Rapoport. Atoms in a laser field. *Physics Reports*, 141(6):320–433, 1986.

[59] M. A. Bouchiat and C. C. Bouchiat. Parity violation induced by weak neutral currents in atomic physics. part II. *J. Phys. France*, 36(6):493–509, 1975.

[60] C. J. Bowers, D. Budker, S. J. Freedman, G. Gwinner, J. E. Stalnaker, and D. DeMille. Experimental investigation of the $6s^2 {}^1S_0 \rightarrow 5d6s^3 D_{1,2}$ forbidden transitions in atomic ytterbium. *Phys. Rev. A*, 59:3513–3526, May 1999.

[61] Amita Mohanty. *Lifetimes, level energies and light shifts in a single trapped Ba^+ Ion*. PhD thesis, University of Groningen, 2016.

[62] J. A. Sherman, T. W. Koerber, A. Markhotok, W. Nagourney, and E. N. Fortson. Precision measurement of light shifts in a single trapped ba^+ ion. *Phys. Rev. Lett.*, 94(24):243001, June 2005.

[63] Bijaya K. Sahoo, Rajat Chaudhuri, B. P. Das, and Debashis Mukherjee. Relativistic coupled-cluster theory of atomic parity nonconservation: Application to $^{137}Ba^+$. *Phys. Rev. Lett.*, 96(16):163003, April 2006.

[64] U. I. Safronova, M. S. Safronova, and W. R. Johnson. Forbidden $m1$ and $e2$ transitions in monovalent atoms and ions. *Phys. Rev. A*, 95:042507, Apr 2017.

[65] O. O. Versolato, L. W. Wansbeek, G. S. Giri, J. E. van den Berg, D. J. van der Hoek, K. Jungmann, W. L. Kruithof, C. J.G. Onder-

water, B. K. Sahoo, B. Santra, P. D. Shidling, R. G.E. Timmermans, L. Willmann, and H. W. Wilschut. Atomic parity violation in a single trapped radium ion. *Hyperfine Interactions*, 199(1):9–19, 2011.

[66] G.S. Giri, O.O. Versolato, L.W. Wansbeek, J.E. Van Den Berg, D.J. Van Der Hoek, K. Jungmann, W.L. Kruithof, C.J.G. Onderwater, B.K. Sahoo, B. Santra, P.D. Shidling, R.G.E. Timmermans, L. Willmann, and H.W. Wilschut. Precision spectroscopy of trapped radioactive radium ions. *Canadian Journal of Physics*, 89(1):69–72, 2011.

[67] Wolfgang Paul. Electromagnetic traps for charged and neutral particles. *Reviews of Modern Physics*, 62(3):531–540, 1990.

[68] C.J. Foot. *Atomic Physics*, volume First edition. Oxford University Press,New York, 2005.

[69] H. G. Dehmelt. Radiofrequency Spectroscopy of Stored Ions I: Storage. *Advances in Atomic, Molecular and Optical Physics*, 3(C):53–72, 1968.

[70] Günther Werth F. G. Major, Viorica N. Gheorghe. Charged Particle Traps. *Springer Series on Atomic, Optical, and Plasma Physics*, 37, 2005.

[71] Bradley Steven Clarke. Numerical and experimental investigation of the stability region for a cylindrical ion trap. Master's thesis, University of Nevada, Las Vegas, Jan 2012.

[72] R I Thompson, T J Harmon, and M G Ball. The rotating-saddle trap: a mechanical analogy to RF-electric-quadrupole ion trapping? *Canadian Journal of Physics*, 80(12):1433–1448, 2002.

[73] Raymond E March. An Introduction to Quadrupole Ion Trap Mass Spectrometry. *Journal of mass spectrometry J. Mass Spectrom*, 32(32):351–369, 1997.

[74] F. G. Major Günther Werth, Viorica N. Gheorghe. *Charged Particle Traps II: Applications*, volume 54. Springer Series on Atomic, Optical, and Plasma Physics, 2009.

[75] K. Jungmann, J. Hoffnagle, R. G. Devoe, and R. G. Brewer. Collective oscillations of stored ions. *Physical Review A*, 36(7):3451–3454, 1987.

[76] N. Kjærgaard, L. Hornekær, A. M. Thommesen, Z. Videsen, and M. Drewsen. Isotope selective loading of an ion trap using resonance-enhanced two-photon ionization. *Applied Physics B: Lasers and Optics*, 71(2):207–210, 2000.

[77] S. Gulde, D. Rotter, P. Barton, F. Schmidt-Kaler, R. Blatt, and W. Hogervorst. Simple and efficient photo-ionization loading of ions for precision ion-trapping experiments. *Applied Physics B: Lasers and Optics*, 73(8):861–863, 2001.

[78] Q. A. Turchette, Kielpinski, B. E. King, D. Leibfried, D. M. Meekhof, C. J. Myatt, M. A. Rowe, C. A. Sackett, C. S. Wood, W. M. Itano, C. Monroe, and D. J. Wineland. Heating of trapped ions from the quantum ground state. *Physical Review A - Atomic, Molecular, and Optical Physics*, 61(6):8, 2000.

[79] D. J. Berkeland and M. G. Boshier. Destabilization of dark states and optical spectroscopy in Zeeman-degenerate atomic systems. *Physical Review A*, 65(3):033413, 2002.

[80] S. L. Cornish, Yi-Wei Liu, I. C. Lane, P. E. G. Baird, G. P. Barwood, P. Taylor, and W. R. C. Rowley. Interferometric measurements of $^{127}I_2$ reference frequencies for 1s–2s spectroscopy in muonium, hydrogen, and deuterium. *J. Opt. Soc. Am. B*, 17(1):6–10, Jan 2000.

[81] E. A. Dijck, M. Nuñez Portela, A. T. Grier, K. Jungmann, A. Mohanty, N. Valappol, and L. Willmann. Determination of transition frequencies in a single $^{138}Ba^{+}$ ion. *Phys. Rev. A*, 91(6):060501, June 2015.

[82] U. Dammalapati, S. De, K. Jungmann, and L. Willmann. Isotope shifts of $6s5d\,^3D - 6s6p\,^1P_1$ transitions in neutral barium. *Eur. Phys. J. D*, 53(1):1–8, Mar 2009.

[83] E.J.Salumbides, K.S.E.Eikema, W.Ubachs, U.Hollenstein, H.Knöckel, and E.Tiemann. The hyperfine structure of 129 i 2 and 127 i 129 in the b band system. *Molecular Physics*, 104(16-17):2641–2652, 2006.

[84] Louis J. Gillespie and Lewis H. D. Fraser. The normal vapor pressure of crystalline iodine1. *Journal of the American Chemical Society*, 58(11):2260–2263, 1936.

[85] W. Demtrder and M. Roach. *Laser Spectroscopy: Basic Concepts and Instrumentation*. Advanced Texts in Physics. Springer Berlin Heidelberg, 2013.

[86] *FS725 Rubidium Frequency Standard Operation and Service Manual*. Stanford Research Systems 1290-D Reamwood Avenue Sunnyvale, California 94089, December 2015.

[87] M. Nuñez Portela, E. A. Dijck, A. Mohanty, H. Bekker, J. E. van den Berg, G. S. Giri, S. Hoekstra, C. J. G. Onderwater, S. Schlesser, R. G. E. Timmermans, O. O. Versolato, L. Willmann, H. W. Wilschut, and K. Jungmann. Ra^+ ion trapping: toward an atomic parity violation measurement and an optical clock. *Appl. Phys. B*, 114(1–2):173–182, Aug 2014.

[88] I. Siemers, M. Schubert, R. Blatt, W. Neuhauser, and P. E. Toschek. The "trapped state" of a trapped ion—line shifts and shape. *Europhys. Lett.*, 18(2):139, Feb 1992.

[89] Y. Stalgies, I. Siemers, B. Appasamy, and P. E. Toschek. Light shift and Fano resonances in a single cold ion. *J. Opt. Soc. Am. B*, 15(10):2505–2514, Oct 1998.

[90] Hilmar Oberst. Resonance fluorescence of single barium ions. Master's thesis, Universität Innsbruck, Innsbruck, Apr 1999.

[91] Thomas Zanon-Willette, Emeric de Clercq, and Ennio Arimondo. Ultrahigh-resolution spectroscopy with atomic or molecular dark resonances: Exact steady-state line shapes and asymptotic profiles in the adiabatic pulsed regime. *Phys. Rev. A*, 84(6):062502, Dec 2011.

[92] D. De Munshi, T. Dutta, R. Rebhi, and M. Mukherjee. Precision measurement of branching fractions of $^{138}Ba^{+}$: Testing many-body theories below the 1% level. *Phys. Rev. A*, 91(4):040501(R), Apr 2015.

[93] P. Kuske, N. Kirchner, W. Wittmann, H. J. Andrä, and D. Kaiser. Lifetime measurements by pulsed laser excitation of fast ion beams. *Phys. Lett. A*, 64(4):377–380, Jan 1978.

[94] Hans Karlsson and Ulf Litzén. Revised Ba I and Ba II wavelengths and energy levels derived by Fourier transform spectroscopy. *Phys. Scr.*, 60(4):321, 1999.

[95] J. J. Curry. Compilation of wavelengths, energy levels, and transition probabilities for Ba I and Ba II. *J. Phys. Chem. Ref. Data*, 33(3):725–746, Sep 2004.

[96] B. Lounis and C. Cohen-Tannoudji. Coherent population trapping and Fano profiles. *Journal de Physique II*, 2(4):579–592, 1992.

[97] A. R. P. Rau. Perspectives on the fano resonance formula. *Physica Scripta*, 69(1):C10–C13, January 2004.

[98] Michael I. Tribelsky, Sergej Flach, Andrey E. Miroshnichenko, Andrey V. Gorbach, and Yuri S. Kivshar. Light scattering by a finite obstacle and fano resonances. *Phys. Rev. Lett.*, 100(4):043903, January 2008.

[99] Andrey E. Miroshnichenko, Sergej Flach, and Yuri S. Kivshar. Fano resonances in nanoscale structures. *Reviews of Modern Physics*, 82(3):2257–2298, 2010.

[100] Andreas Bthaler, Stefan Rotter, Florian Libisch, Joachim Burgdrfer, Stefan Gehler, Ulrich Kuhl, and Hans-Jrgen Stckmann. Probing decoherence through fano resonances. *Phys. Rev. Lett.*, 105(5):056801, July 2010.

[101] Christian Ott, Andreas Kaldun, Philipp Raith, Kristina Meyer, Martin Laux, Jörg Evers, Christoph H. Keitel, Chris H. Greene, and Thomas Pfeifer. Lorentz meets fano in spectral line shapes: A universal phase and its laser control. *Science*, 340(6133):716–720, 2013.

[102] C. D. Lin and Wei-Chun Chu. Controlling atomic line shapes. *Science*, 340(6133):694, May 2013.

[103] Boris Luk'Yanchuk, Nikolay I. Zheludev, Stefan A. Maier, Naomi J. Halas, Peter Nordlander, Harald Giessen, and Chong Tow Chong. The Fano resonance in plasmonic nanostructures and metamaterials. *Nature Materials*, 9(9):707–715, 2010.

[104] Jun Zhao, Chunjie Zhang, Paul V. Braun, and Harald Giessen. Large-area low-cost plasmonic nanostructures in the NIR for fano resonant sensing. *Adv. Mater.*, 24(35):OP247–OP252, September 2012.

[105] Andrea Lovera, Benjamin Gallinet, Peter Nordlander, and Olivier J.F. Martin. Mechanisms of fano resonances in coupled plasmonic systems. *ACS Nano*, 7(5):4527–4536, 2013.

[106] Jérémy Butet and Olivier J. F. Martin. Fano resonances in the nonlinear optical response of coupled plasmonic nanostructures. *Optics Express*, 22(24):29693, 2014.

[107] U. Fano. Effects of configuration interaction on intensities and phase shifts. *Phys. Rev.*, 124:1866–1878, Dec 1961.

[108] David Hucul, Justin E. Christensen, Eric R. Hudson, and Wesley C. Campbell. Spectroscopy of a synthetic trapped ion qubit. *Phys. Rev. Lett.*, 119:100501, Sep 2017.

[109] K. Wendt, S. A. Ahmad, F. Buchinger, A. C. Mueller, R. Neugart, and E. W. Otten. Relativistic j-dependence of the isotope shift in the 6s-6p doublet of Ba II. *Zeitschrift fr Physik A Atoms and Nuclei*, 318(2):125–129, June 1984.

[110] Elwin A. Dijck, Amita Mohanty, Nivedya Valappol, M. Nuñez Portela, Lorenz Willmann, and Klaus Jungmann. Lifetime of the $5d\,^2D_{5/2}$ level of $^{138}Ba^+$ from quantum jumps with single and multiple Ba^+ ions. *Phys. Rev. A*, 97(3):032508, March 2018.

[111] The Qweak Collaboration. Precision measurement of the weak charge of the proton. *Nature*, 557(7704):207–211, 2018.